ABSTRACT

Title of dissertation: Multi-Valley Physics of Two-Dimensional Electron Systems on Hydrogen-Terminated Silicon (111) Surfaces

Robert Nicholas McFarland
Doctor of Philosophy, 2010

Dissertation directed by: Dr. Bruce E. Kane
Laboratory for Physical Sciences

Recent work on two dimensional electron systems (2DES) has focused increasingly on understanding the way the presence of additional degrees of freedom (e.g. spin, valleys, subbands, and multiple charge layers) affect transport as such effects may be critical to the development of nanoscale and quantum devices and may lead to the discovery of new physics . In particular, conduction band valley degeneracy opens up a rich parameter space for observing and controlling 2DES behavior[1]. Among such systems, electrons on the (111) surface of silicon are especially notable because effective mass theory predicts the conduction band to be sixfold degenerate, for a total degeneracy (spin $\times$ valley) of 12 in the absence of a magnetic field (B). Previous investigations of Si(111) transport using Metal-Oxide-Semiconductor Field Effect Transistors (MOSFETs) observed a valley degeneracy g_v of 2 except in certain specially prepared samples with low mobility [2, 3].

We have developed a novel device architecture for investigating transport on a H-Si(111)-vacuum interface free from the complications created by intrinsic disorder at Si-SiO_2 interfaces. The resulting devices display very high mobilities (up to 110,000 $cm^2/V\,s$ at 70 mK, more than twice as large as the best silicon MOSFETs), enabling us to probe valley-dependent transport to a much greater degree than previously possible. In particular, we observed detailed Integer Quantum Hall structure with hints of Fractional states as well. These devices display clear evidence of six occupied valleys, including strongly "metallic" temperature dependence expected for large g_v [4]. Some devices show strong sixfold degeneracy while others display a partial lifting of the degeneracy, resulting in un-

equal distribution of electrons among the six valleys. This symmetry breaking results in anisotropic transport at low B fields, but other observed anisotropies remain unexplained.

Finally, we apply this unusual valley structure to show how corrections to the low-B magnetoresistance and Hall effect can provide information about valley-valley interactions. We propose a model of valley drag, similar to Coulomb drag in bilayer systems, and find good agreement with our experimental data, though a small residual drag in the $T \to 0$ limit remains unexplained.

Multi-Valley Physics of Two-Dimensional Electron Systems on Hydrogen-Terminated Silicon (111) Surfaces

by

Robert Nicholas McFarland

Dissertation submitted to the Faculty of the Graduate School of the
University of Maryland, College Park in partial fulfillment
of the requirements for the degree of
Doctor of Philosophy
2010

Advisory Committee:
Dr. Bruce E. Kane, Advisor
Professor Howard Dennis Drew, Chair
Professor James R. Anderson
Professor Ian Appelbaum
Professor Martin Peckerar

Acknowledgments

Thanks ...

To Bruce Kane, for teaching the discipline of experiment

and John Boccio for teaching the beauty of theory.

To Kevin, for igniting the torch

and Tomek, for carrying it on.

To Rebecca for trudging alongside me through it all

and Lirael for forcing me to stop and play sometimes.

Finally, thanks to Bertrand Russell and everyone not thanked in this dissertation.

Table of Contents

List of Tables

List of Figures

Nomenclature

α	fraction of electrons in two-valley subband
δ	coefficient of B-dependent gap in SdH region
Δ_{4-2}	energy gap due to six valleys splitting into four-valley and two-valley states
η	multi-valley correction factor to ρ
Γ	Landau Level width
μ	electron transport mobility
ν	filling factor $= \frac{hn_s}{eB}$
ω_c	cyclotron frequency
Φ	dimensionless mass ratio $(\bar{m}/m^*)^2$
ψ	wafer miscut angle
τ_0	transport lifetime
τ_q	quantum lifetime $\hbar/(2\pi k_B T_D)$
τ_{vv}	intervalley momentum relaxation rate
g_v	valley degeneracy
I_g	gate current
M_j	mass tensor of j^{th} valley or valley pair
M_{jk}	reduced mass tensor of $j-k$ valley system
n_s	carrier density
q_{TF}	Thomas–Fermi screening wave vector
r_H	reduced Hall coefficient $rho_{x,y}/(B/n_s e)$
T_D	Dingle (scattering) temperature
V_g	gate voltage
(I/F)QHE	(Integer/Fractional) Quantum Hall Effect
2DES	Two–dimensional electron system
AFM	Atomic Force Microscopy
Ai(x)	Airy function of the first kind
AlAs	aluminum arsenide
BOX	Buried Oxide, middle layer of SOI
DI	deionized water
DoS	density of states
FET	Field Effect Transistor
HF	hydrofluoric acid
LLs	Landau Levels
MIT	metal–insulator transition
MOSFET	Metal-Oxide-Semiconductor Field Effect Transistor
NH_4F	ammonium fluoride
RIE	Reactive Ion Etch
RTA	Rapid Thermal Anneal
RuOx	ruthenium oxide
SdH	Shubnikov-de Haas
SOI	Silicon-On-Insulator
UHV	ultra high vacuum

Chapter 1

Introduction

1.1 2D systems with Discrete Degrees of Freedom

Over the many decades that two-dimensional electron systems (2DESs) have been studied two major components have driven research forward by opening up new domains to explore and new phenomena: increases in mobility have enabled finer resolution of the energy level structure of the quantized 2DES and revealed new phenomena from the integer quantum hall effect (QHE) to the fractional QHE. Likewise, the presence of additional discrete degrees of freedom has been long predicted to lead to rich new physics, but only recently has it been possible to create such systems and explore these effects. Electron spin now leads to the field of spintronics, making use of this additional property to expand the power of semiconductor technology. Double quantum wells have provided a platform for examining 2DES interactions and the physics of many-body excitations and collective modes. More recently the sublattice degeneracy of graphene has become an active research topic as well.

Conduction band valley degeneracy is especially interesting because it is an intrinsic property of the material, not directly dependent on fabrication or spatial parameters. Thus valley degeneracy can substantially increase the state space of an electron system without a significant scaling of engineering effort. From an applications perspective, it may provide an additional control parameter, or (as in the case of quantum information processing) it may be a source of decoherence. In either, case it must be understood well.

Bulk silicon is known to have a sixfold degenerate conduction band (one minimum along each [100] direction). In 2D Si systems the reduction in symmetry will lower this degeneracy, but the $\langle 111 \rangle$ orientations preserve the sixfold symmetry (Fig. 1.1). Together with spin, this yields a potentially 12-fold degenerate state space at zero magnetic field.

Early investigations of valley degeneracy on Si(111) were performed on Metal-Oxide-Semiconductor Field Effect Transistors (MOSFETs) with peak mobility $\mu \sim$2,500 cm^2/V s

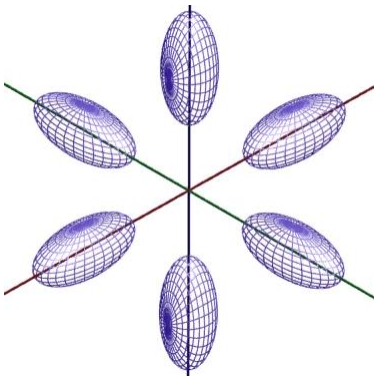

Figure 1.1: Six degenerate energy ellipsoids of bulk silicon projected on to the (111) surface.

(though recent work reports μ as high as 4,000 $\mathrm{cm}^2/\mathrm{V\,s}$[5])*. For many years, analysis of Shubnikov-de Haas (SdH) oscillations in these systems had always shown a valley degeneracy g_v=2; In 1979 Tsui and Kaminski observed sixfold degeneracy in certain low-mobility ($\sim$1,000 $\mathrm{cm}^2/\mathrm{V\,s}$) samples specially-prepared to reduce interface strain[3], though the precise reason for this difference was never fully settled.

From the ambiguities of the Si(111) MOSFET data it becomes clear that the properties of the oxide dielectric and its interface with the silicon greatly affect the resulting transport properties. How then can we separate these effects from the properties intrinsic to the silicon surface? The simplest approach would be to remove the oxide altogether. However, the bare surface is very reactive, with dangling bonds leading to reconstruction and adsorption of contaminant particles. This can alter the band structure of the silicon, either adding trap states that prevent conduction or filling the gap with conducting states.

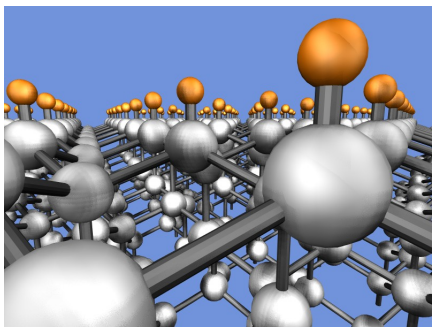

Figure 1.2: H-Si(111) surface. The silicon atoms are silver, hydrogen are gold. Image by B. E. Kane.

*Mobilities on these systems are lower in part due to a larger effective mass and higher density of surface atoms.

Hydrogen termination provides a feasible and elegant solution to this problem. It was found that chemical treatment with hydrofluoric acid (HF) or ammonium fluoride (NH_4F) *passivates* the silicon surface: the dangling bonds are each terminated with a hydrogen atom (Fig. 1.2), reducing surface reactivity without adding additional states to the Si bandgap[6, 7]. Furthermore, NH_4F etches silicon anisotropically, preferentially creating {111} surfaces, enabling us to create atomically flat inert Si(111) surfaces with simple chemical treatment. Surface flatness indicates low disorder and is also essential for the contact bonding method used to create our devices (see §3.2). Although Si-(100) can be H-terminated via the same chemical methods, this is known to roughen the silicon surface[8]. Atomically flat H-Si(100) surfaces have only been achieved in ultra high vacuum (UHV).

1.2 Our Device

While much work has been done studying the chemistry and structure of the H-Si(111) surface, this has not previously been connected to electronic transport on H-Si(111) as a device substrate. A major reason for this is that the H-passivation deteriorates (∼hrs) in ambient conditions. Further, one must construct a gate to create an inversion layer in the Si without covering the surface with material (and as a result introducing new disorder) and Ohmic contacts to probe the electron system without adding contamination or destroying the contacts in the preparation of the H-Si surface. We have developed a novel device design for preserving the H-Si(111) surface while enabling us to probe its transport properties.

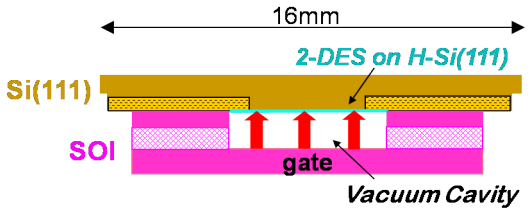

Figure 1.3: Basic device design. Two substrates are bonded together via Van der Waals forces to create the vacuum cavity that preserves the H-Si(111) surface.

The crux of the design is to employ contact bonding techniques developed for integrated circuit applications to encapsulate the H-Si(111) surface in a local vacuum cavity built into the device. The cavity is created by etching a recess into a second sample and

bonding it to the surface of our H-Si(111) sample in a vacuum chamber. (See Chapter 3 for a detailed discussion of the device construction and Appendix B for specifics of our fabrication process.) The bonded device can then be removed from vacuum and wired as a Field Effect Transistor (FET) with four source-drain contacts. The vacuum cavity both serves as the gate dielectric and protects the H-Si(111) surface from exposure to ambient conditions.

This device is in many ways a proof of concept for a broader-use technique for encapsulating any sort of environment-sensitive nano-structure in a sealed device that can be wired and probed *ex situ* using ordinary lab environments. A high-quality (low-disorder) bare surface also makes a promising substrate for nano-structures or quantum devices as it ensures that the substrate defects will not inhibit or obscure device properties.

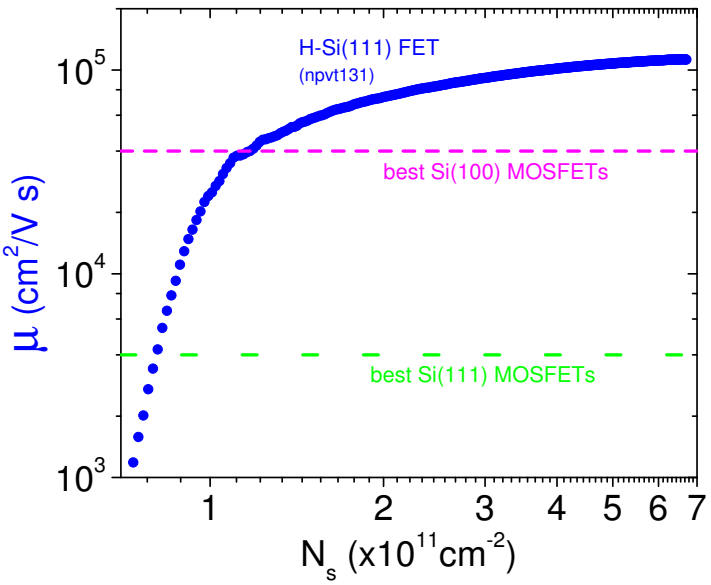

Figure 1.4: base T mobility for our best H-Si(111) vacuum FET

1.3 Results

The first thing we notice about our H-FET devices is that they display extremely high mobilities. The largest mobility reported for Si(111) MOSFETs is 4,000 $\mathrm{cm}^2/\mathrm{V\,s}$, an order of magnitude lower than the best Si(100) MOSFETs due in part to {111} having

nearly twice the effective electron mass and a higher density of surface atoms (and thus possible defect sites). In contrast, our fabrication process now regularly produces devices with $\mu \approx$20,000 and one device (npvt131, source of most of the data presented in this thesis) displayed μ=110,000 at T=70 mK. While we don't know the exact factors affecting device mobility, the fact that we have eliminated disorder due to the Si-SiO_2 interface, including trapped charge and inhomogeneous strain effects, would certainly be expected to boost mobility.

This improvement in mobility gives us an enormous increase in resolution for probing the energy structure of our 2DES, since low mobility leads to shorter scattering times and thus a broadening of the energy levels. We have been able to make the first detailed observations of the integer Quantum Hall Effect (IQHE) on Si(111) (in 1986 Gusev *et al* saw signs of quantized Hall conductance, but only $\nu = 2, 6, 10$ were discernible[9]). From our data we see a consistent picture of low-B valley degeneracy being lifted at high magnetic fields, with gaps eventually appearing at spacings of $\Delta\nu = 1$. In addition, our highest mobility device shows additional gaps at what we believe to be the $\frac{4}{3}$ and $\frac{8}{5}$ fractional Quantum Hall states.

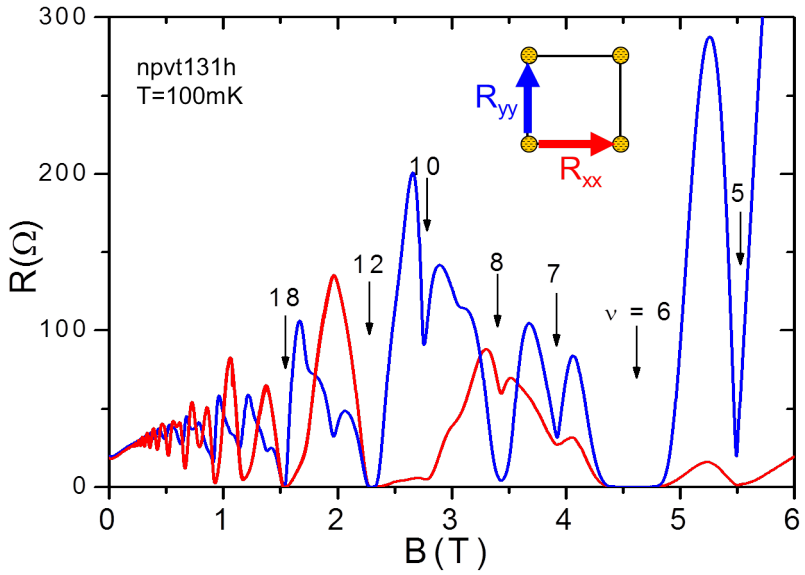

Figure 1.5: Magnetoresistance measured via orthogonal source current directions.

Interestingly, when we run the source-drain current in orthogonal directions, we ob-

serve an anisotropic response throughout the field range (Fig. 1.5). At low field this may manifest in slight differences in the SdH phase and amplitude. By moderate fields the prominent gaps may differ somewhat while at higher fields the QHE gaps generally occur at the same filling factor but with considerable variation in the magnitude of the minima and the peaks in between.

1.3.1 6–Valley Structure

From the data we have collected, we begin to assemble a model of the multi-valley 2DEG. We find all six valleys populated at $B = 0$ in every device although the valleys are not always degenerate. Our highest mobility device displays distinct signs of sixfold valley degeneracy with a valley splitting measured (in §6.1.1) to be at most ≈ 0.1 K.

In some devices (most notably `npvt75` discussed in this thesis) the sixfold degeneracy is clearly lifted even at $B = 0$, though never so strongly as to completely depopulate any of the valleys. This weak degeneracy lifting has several effects on the 2DES. The electron density becomes asymmetrically distributed among the valleys, potentially creating transport anisotropies. Different scattering rates among the valleys can also affect the observed SdH frequency. At higher B fields this splitting can affect the values we measure for cyclotron and spin gaps as well.

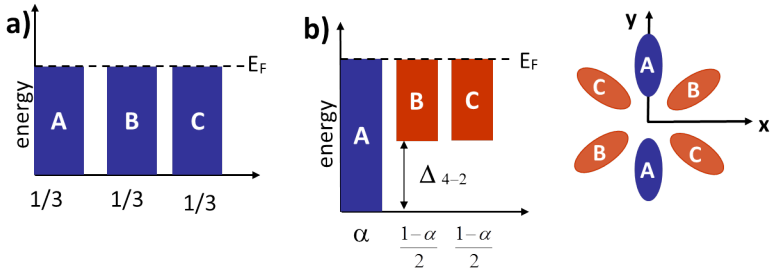

Figure 1.6: Distribution of electrons among valleys at B=0 for a) strong sixfold degeneracy and b) moderate valley splitting.

1.3.2 Valley drag

In addition to developing a model for the valley structure and splitting on Si(111), we have developed a new method for probing valley-valley interactions. As discussed in

§7.2 independent anisotropic valley channels result in additional B dependence of the 2DES magnetoresistance and Hall effect. Interactions between valleys (even those which conserve total 2DES momentum) will wash out this effect, causing the transport behavior to approach that of an isotropic single-valley system. We develop a model of valley-valley momentum exchange similar to Coulomb drag observed in double quantum wells in which electrons in each valley "tug" at electrons in other valleys. We measure changes to the reduced Hall coefficient $r_H \equiv \rho_{x,y}/(B/n_s e)$ in the $B \to 0$ limit as a function of temperature and find good agreement with our drag model. Further, the damping rate τ_{vv}^{-1} associated with this drag scales roughly as $(T/T_F)^2$, consistent with expected theoretical behavior for a single-valley interacting Fermi liquid[10]. However, the value of r_H at base temperature (70 mK) is lower than the lower bound predicted by our model (or indeed any similar model), a result which is both experimentally robust and as yet unexplained.

1.4 Outline of the Thesis

The remainder of this thesis will be organized as follows. Chapter 2 will cover some of the basic physics of valley degeneracy and two-dimensional electron systems, properties of Hydrogen-terminated Si(111), and review various effective masses that will come up throughout this work. Chapter 3 describes the assembly and operation of our H-Si(111) FET, with further detail provided in Appendices B and C. We also present a quick reference guide to the main devices discussed in this text.

In Chapter 4 we summarize the experimental measurements and instruments used to characterize our devices. We then turn our attention to experimental results, with Chapter 5 covering temperature and density dependence at zero magnetic field, including a brief consideration of the density-dependent transition from "metallic" ($d\rho/dT > 0$) to "insulating" ($d\rho/dT < 0$) behavior; Chapter 6 discusses the effects of magnetic field, including Shubnikov-de Haas oscillations and the Quantum Hall Effect; and Chapter 7 focuses on recent work using the zero-field Hall coefficient as a probe of "valley drag", total momentum-conserving valley-valley interactions that can wash out many of the effects of valleys on 2D transport. In Chapter 8 we briefly consider additional interesting observations

we have made in these devices that have not been given more thorough discussion due to time limitations, incomplete analysis, or simply because we have no compelling explanation for them yet. Finally, in Chapter 9 we summarize this work and consider future directions for the research, both in the near term and distant possibilities.

Chapter 2

Background

In this chapter we establish the basic theoretical framework and vocabulary for discussing our experimental work on two-dimensional multi-valley systems. While we present this information in a block at the outset of this thesis in order to lay out important ideas, the material is not central to understanding the experimental basics covered in Chapters 3 and 4 or the characterization measurements presented in Chapter 5. The reader may, if so inclined, detour around this chapter and refer back to it as needed.

We work almost entirely in the effective mass approximation, even though some of the data presented later suggests that more exotic physics is in play. Since we are just beginning to explore the properties of a new physical system, there remains much that we do not yet understand and rushing to invoke fancy many-body explanations would be premature. A great deal of our data can be explained within the effective mass approximation, which in some respects already allows us too much "wiggle room" in interpreting our results until additional data constrains us to a meaningful answer.

2.1 Valley Basics

For indirect bandgap semiconductors, the conduction band minimum is not at the same point in k-space as the valence band maximum. For silicon, the minimum appears at a point k_0 approximately 85% of the way to the edge of the Brillouin zone along the (100) direction[11]. Due to the symmetry of the silicon lattice, this minimum appears along each of the $\langle 100 \rangle$ directions for a total of six equivalent energy minima.

Another multi-valley semiconducting system is aluminum arsenide (AlAs), in which the band minimum appears on the edge of the Brillouin zone at the X point[11]. This results in six half-valleys or three full valleys. In real AlAs quantum well devices the choice of well width breaks this symmetry to g_v=1 (for narrow wells) or $g_v = 2$ (for thick wells)[1]. This splitting can be further controlled via applied strain. The properties of these valleys and

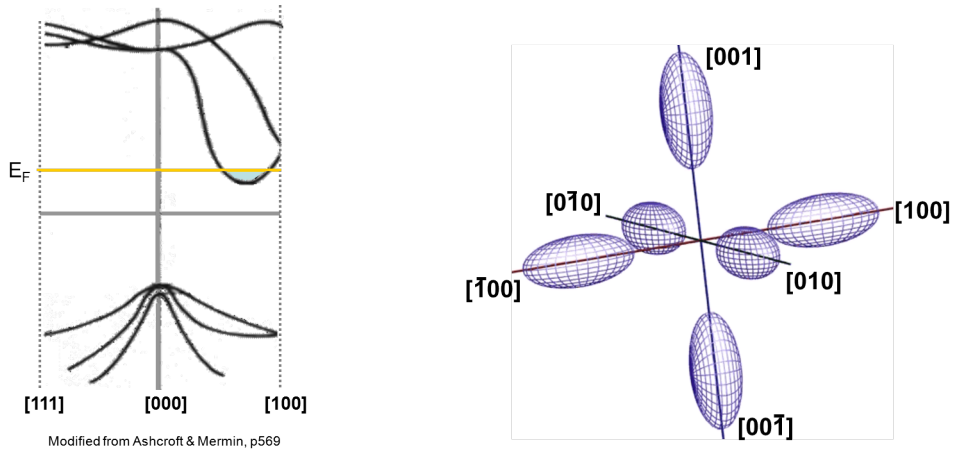

Figure 2.1: Left: Si bulk band structure (modified from [11, p. 586]). Right: constant energy ellipsoids (solutions to Eq. (2.1)) in k-space for bulk silicon.

their effect on 2D transport have been well studied and thus will at times provide a useful reference point for our work.

2.1.1 Valleys and anisotropic mass

Near each conduction band minimum $E(k)$ is very nearly parabolic and can be written as

$$E(k) = \frac{\hbar^2}{2}\left(\frac{k_x^2}{m_x} + \frac{k_y^2}{m_y} + \frac{k_z^2}{m_z}\right) = \frac{\hbar^2}{2}\vec{k}\cdot\mathbf{W}\cdot\vec{k} \tag{2.1}$$

where the inverse effective mass tensor $\mathbf{W}$ has eigenvalues $1/m_x, 1/m_y, 1/m_z$ and eigenvectors along the principle axes of the constant energy ellipsoid.

For bulk silicon, the masses are m_l, m_t, m_t where $m_l = 0.916m_e$ is the mass along the ellipsoid major axis and $m_t = 0.190m_e$ is the mass for motion transverse to this axis. In general we will take the free electron mass m_e to be the understood unit for all effective mass values and will thus omit it for brevity.

3D to 2D (surface dependence)

For 2D systems, either at the surface, in a thin film, or in a narrow quantum well, this degeneracy will in general be affected by the orientation of the 2D plane relative to the bulk crystal directions and the axes of the degenerate ellipsoids. For example, in (100)

MOSFETs the two valleys with long axes pointed out of the plane will have lower energy than the remaining 4 so a 2DES created in such a system will have g_v=2. In Si(111) the valleys project symmetrically on to the 111 plane so the sixfold degeneracy remains.

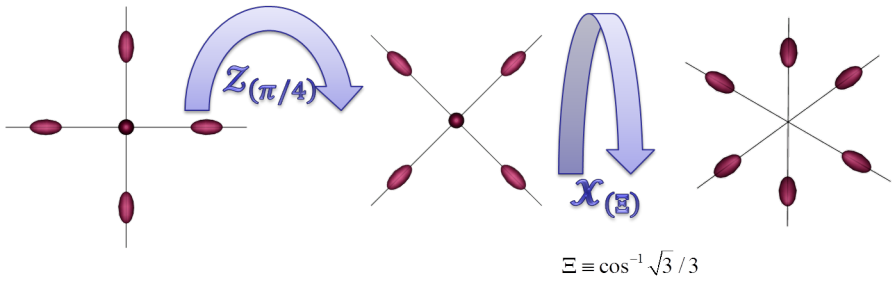

Figure 2.2: Illustration of the k-space rotations that transform a $\langle 100 \rangle$–oriented system to $\langle 111 \rangle$ as shown mathematically in Eq. (2.2).

We will see in §2.2 that electrons on a gated surface become quantized in the z direction (normal to the surface) with an energy spectrum determined by m_z. Motion in the plane of the surface is affected by the masses m_x and m_y in the surface coordinate frame. It is evident, therefore, that the orientation of the surface can significantly affect the energy and transport properties of the 2DES. To see this effect, we transform the bulk mass tensor (aligned with the principle masses) into the coordinates of the [111]–oriented system, defining z to be normal to the surface and choosing a convenient assignment of x and y within the plane.

$$\begin{aligned} \mathbf{M}_{111} &= \mathcal{X}(-\Xi)\mathcal{Z}(-\pi/4)\mathbf{M}\mathcal{Z}(\pi/4)\mathcal{X}(\Xi) \\ &= \begin{pmatrix} \frac{1}{2}(m_x+m_y) & \frac{m_x-m_y}{2\sqrt{3}} & \frac{m_x-m_y}{\sqrt{6}} \\ \frac{m_x-m_y}{2\sqrt{3}} & \frac{1}{6}(m_x+m_y+4m_z) & \frac{m_x+m_y-2m_z}{3\sqrt{2}} \\ \frac{m_x-m_y}{\sqrt{6}} & \frac{m_x+m_y-2m_z}{3\sqrt{2}} & \frac{1}{3}(m_x+m_y+m_z) \end{pmatrix} \end{aligned} \tag{2.2}$$

where $\Xi = \arccos 1/\sqrt{3}$.

symbol	expression	value
m_e		1
m_z	$1/\mathbf{W}_{zz}$	0.258
m_x	$\mathbf{M}_{xx}$	0.190
m_y	$\mathbf{M}_{yy}$	0.674
m_{op}	$\frac{2m_x m_y}{m_x+m_y}$	0.296
m^*	$\sqrt{m_x m_y}$	0.358
$\bar{m}$	$(m_x + m_y)/2$	0.432
m_-	$(m_y - m_x)/2$	0.242

Table 2.1: common effective mass parameters for Si(111)

2.1.2 Important masses

Because there are so many mass parameters that will appear throughout this work, we will take a moment to clarify and distinguish the notation used.

- The **normal mass** $m_z \equiv 1/\mathbf{W}_{zz}$ determines vertical bound state energy, appearing in the E_j^z in Eq. (2.5). Although $m_z = \mathbf{M}_{zz}$ when $\mathbf{W}$ is diagonal, this is not the case in general.

- The **density of states effective mass** $m^* = \sqrt{m_x m_y}$ is the geometric mean of the in–plane masses and appears in the density of states $D(E)$, the Fermi energy, and the cyclotron energy.

- The **free electron mass** m_e determines Zeeman (spin) splitting via the electron spin magnetic moment $\mu_B = \frac{\hbar e}{2m_e}$.

- The **optical** or **conductivity mass** $m_{op} = 2m_x m_y/(m_x + m_y) = (\frac{m_x^{-1}+m_y^{-1}}{2})^{-1}$ (the harmonic mean of the in–plane masses) appears in transport properties such as resistivity ρ.

We also introduce two symbols $\bar{m}$ and m_- as a useful shorthand. $\bar{m} \equiv (m_x + m_y)/2$ is the arithmetic mean of the in-plane masses and is the same for all valleys (equal to $\frac{1}{2}$ the trace of the 2D mass tensor and thus invariant to rotation). Its anti-symmetric twin $m_- \equiv (m_y - m_x)/2$ turns up in a number of calculations and vanishes in the case of isotropic valleys ($m_x = m_y$). We can use this to express the conductivity mass as $m_{op} = m^{*2}/\bar{m}$.

2.2 2D confinement potential

Consider a charged system confined to a surface by an effective electric field F perpendicular to the surface; the Hamiltonian is given by:

$$\mathcal{H} = \frac{\hbar^2}{2}\left(\frac{k_x^2}{m_x} + \frac{k_y^2}{m_y} + \frac{k_z^2}{m_z}\right) + V(z) \tag{2.3}$$

where we approximate the interface potential $V(z)$ as

$$V(x) = \begin{cases} \infty & z > 0 \\ -zeF & z \leq 0 \end{cases}, \tag{2.4}$$

i.e. we approximate the barrier at the interface as infinite (in practice it will be on the order of the Si work function $\sim$5 eV$\sim$58,000 K) and ignore corrections due to exchange interaction and image charge. This is called the triangular well approximation[12]. The parameter F gives the effective field, including both the field applied by the gate and the (much smaller) contribution due to depletion charge*.

Since $V(z)$ depends only on z we can separate the x and y dependence of Eq. (2.3) (free particle solutions) and the Bloch wavefunction $\mathbf{u}(\mathbf{R})$to focus on the z-dependent part of the resulting wavefunction.

$$\Psi = \zeta_z e^{ik_z z}\mathbf{u}(\mathbf{R}) \times e^{ik_x x/\hbar}e^{ik_y y/\hbar} \tag{2.5}$$

$$\zeta_z \approx \mathrm{Ai}\left(\frac{2m_z}{\hbar^2}^{1/3}(eFz - E_i)\right) \tag{2.6}$$

$$E = E_j^z + \frac{\hbar^2}{2}\left(\frac{k_x^2}{m_x} + \frac{k_y^2}{m_y}\right) \tag{2.7}$$

$$E_j^z \approx \left(\frac{\hbar^2}{2m_z}\right)^{1/3}\left(\frac{3\pi e^2 N_s}{2\epsilon_0\kappa}\left(j + \frac{3}{4}\right)\right)^{2/3} \tag{2.8}$$

where the envelope functions ζ_z are Airy functions. Thus we obtain a ladder of discrete bound states for the z component while retaining the continuum of free particle states in

*Ref. [12] includes an adjustable parameter $0 \leq f \leq 1$ in the definition of F. We find that setting $f \approx 0.8$ gives the best agreement with the more general self-consistent variational calculation.

x and y. The gap between the two lowest-energy z-states (j=0 to j=1) is ∼470 K (for n_s ∼7×10^{11} cm^{-2},F ∼10^6 V/cm) while Fermi temperatures for our system are generally of order ∼10 K, so we can safely ignore higher subbands and treat our electron system as two-dimensional.

We note that E_j^z depends upon m_z, the effective mass component normal to the surface, and is therefore dependent on the crystallographic orientation of the surface. Because E_0^z is so large, even a very small mismatch in m_z between two sets of valleys can create a measurable difference in ground state energy.

2.2.1 2D Density of States

The density of states (DoS) for a 2D system is constant and given by

$$D(E) = \frac{g_s g_v m^*}{2\pi\hbar^2}. \tag{2.9}$$

Thus the additional degeneracies from spin g_s and valley g_v directly increase the density of states.

For $B > 0$ the continuous energy spectrum lifts, becoming instead a ladder of discrete states called Landau Levels (LLs) with energy spectrum determined by the cyclotron frequency ω_c:

$$E_c = \hbar\omega_c(N + \frac{1}{2}) = \frac{\hbar eB}{m^*}(N + \frac{1}{2}). \tag{2.10}$$

Each level has a degeneracy (states per unit area) of $\beta_{LL} = eB/h$ in addition to g_s and g_v. If the carrier density is n_s we can determine the number of filled levels:

$$\nu = \frac{hn_s}{eB}. \tag{2.11}$$

The parameter ν is called the *filling factor*; it will prove to be the leading descriptive parameter for our 2DES. Note that the definition of ν does not account for spin and valley degeneracy, so (for example) for a twofold spin-degenerate system filling an additional LL would increase ν by 2.

2.2.2 Shubnikov–de Haas oscillations

For small B this regular modulation of the density of states leads to oscillations in the 2DES resistivity called *Shubnikov–de Haas oscillations* (SdH)[13, 12, 14]. The diagonal components of both the conductivity σ_{xx} and resistivity $\rho_{xx} = \sigma_{xx}/(\sigma_{xx}^2+\sigma_{xy}^2)$ are maximum when a Landau level is half-filled and minimum when all occupied LLs are filled[†]. In the limit of zero temperature and neglecting level broadening, the amplitude of these oscillations is given by

$$\Delta\rho \sim 1 - \cos(2\pi\nu/g_s g_v). \tag{2.12}$$

The oscillation is periodic in n_s and $1/B$ with period given by the total degeneracy $g_s g_v$. The signal is further modified by intrinsic as well as temperature–dependent broadening which we will discuss in §6.1.1.

2.3 Silicon $\langle 111 \rangle$

In this work we have studied the (111) surface of silicon. This choice of surface is beneficial for chemical fabrication and rich in valley physics. Here we describe the basic properties of the Si(111) surface and the benefits it offers.

Crystal Structure

The ideal (111) surface of silicon has a triangular structure with atoms spaced by ≈ 3.8 Å. Each atom has a single dangling bond oriented normal to the surface (Fig. 2.3). In our final device, each of these bonds will be terminated with a hydrogen atom. We consider only the unreconstructed 1×1 surface, which the H-termination should help preserve. At high temperatures in UHV, dangling bonds of surface atoms can connect to neighboring atoms, reshaping the symmetry of the surface, most commonly in a periodic array of a 7 atom by 7 atom pattern dubbed the 7×7 reconstruction[8].

[†]Since the DoS goes to zero between LLs, $\sigma_{xx} \to 0$; $\sigma_{xy} \neq 0$ for $B > 0$ so ρ_{xx} must go to zero as well

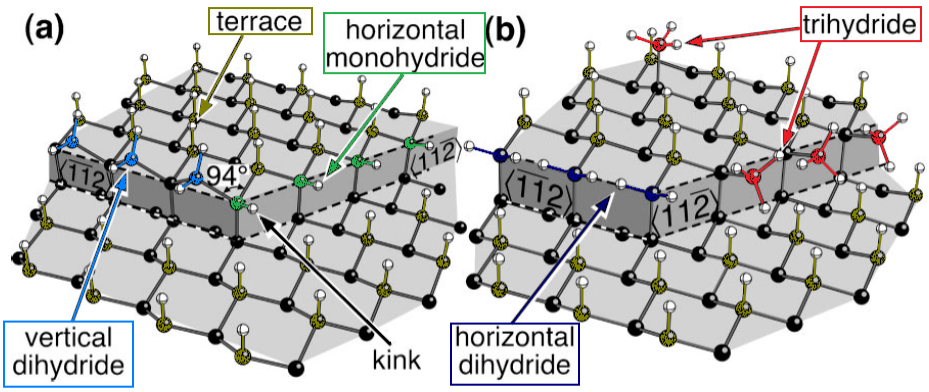

Figure 4 The atomic structure of H-terminated Si(111) surfaces. The dark balls represent Si atoms, while the light balls represent H atoms. (*a*) Sites that have been identified by vibrational spectroscopy; (*b*) transient species.

Source: Hines, M., *Annu. Rev. Phys. Chem.*, 54, 29 (2003) (Color Added)

Figure 2.3: Bonds on H-Si(111) surface. The vertical H–Si bonds on the terrace are relatively stable and electronically inert. NH_4F attacks the other bond species found at step edges, creating large flat terraces.

Wafer miscut and atomic steps

In practice, silicon wafers are never perfectly oriented according to the specified direction, so we cannot expect a single, uninterrupted atomic plane across an entire 4" or 2" wafer or even a $\approx$1 cm^2 sample. The deviation of the actual surface normal from the nominal direction is given by the *miscut angle* ψ, typically much less than one degree. As shown in Fig. 2.4, this creates a series of atomic steps with a spacing determined by the miscut angle. By imaging the silicon surface with Atomic Force Microscopy (AFM) we can measure the width of the steps and thus compute the wafer miscut angle. This in turn enables us to estimate the valley splitting due to misorientation (§2.4.1) . It should be emphasized that such cartoons and even AFM images exaggerate the height of the steps, creating the illusion of a bumpy surface. In fact, the step height is much smaller than the step width, roughly similar to the thickness of a sheet of paper of rise over the length of the page. Nonetheless, these steps may play an important role in the properties of Si(111)–based nanosystems. [15] presents a model in which step effects account for an observed B dependent *suppression* of valley splitting, while [16] use the steps to guide the growth of $GdSi_x$ nanowires.

As shown earlier (§2.1.1) the crystallographic orientation of a surface affects how the

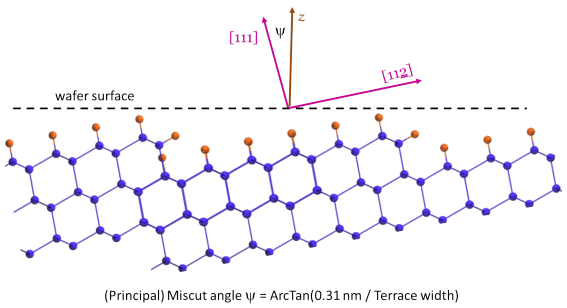

Figure 2.4: Cartoon of Si(111) surface in profile showing how misorientation results in terraces or steps along the surface. A second angle φ characterizes the orientation of the steps in the plane of the wafer.

six degenerate valleys of the bulk project into 2D. For the {111} planes of Si, we can see that the valleys project equally, preserving the sixfold symmetry in 2D (Fig. 2.5).

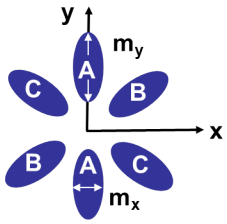

Figure 2.5: Projection of the six constant energy ellipsoids from the bulk onto the (111) surface.

As we shall see in §2.4.1 this symmetry breaks if the surface normal deviates from the ideal [111] orientation.

2.4 Mechanisms of Valley Splitting

Although the *ideal* Si(111) surface possesses sixfold valley degeneracy, there are many mechanisms that can break the sixfold symmetry and lift the valley degeneracy. We will now consider several common sources of valley splitting. Note that within effective mass theory, oppositely–aligned valleys are completely equivalent since they have identical mass tensors. Thus the valley splitting mechanisms discussed here can at most separate the six valley levels into three doubly–degenerate levels; any means of lifting this remaining twofold valley degeneracy would necessarily move us outside of effective mass theory.

2.4.1 Wafer Miscut

As shown in §2.2 the bound state energies E_j^z depend on the crystal orientation via the normal mass m_z. However, we also found in §2.3 that real silicon wafers are never perfectly oriented and will generally differ by a miscut angle ψ from [111]. If we account for this deviation in our calculation of the inverse mass tensor $\mathbf{W}$ we find that the energy levels associated with the three valley pairs shift to non-degenerate values. From this simple effective mass model we estimate the splitting for small miscut to be

$$\Delta m_z \approx \frac{\sqrt{2}(m_l - m_t)\psi}{m_l + m_t} + O[\psi]^2 \Longrightarrow \Delta_\psi \approx 5.5\text{K/deg} \tag{2.13}$$

while more sophisticated calculations based on tight-binding methods indicate that the effect will generally be larger than this[17]. See §A.4 for further details.

2.4.2 Strain

Strain on the crystal lattice can change the shape of the conduction band, breaking the symmetry of the unstrained crystal and lifting the valley degeneracy. Strain can arise at the interface between different materials due to lattice mismatch or different rates of thermal contraction, though for Si(111) strain normal to the surface does not break the rotational valley symmetry. One can also induce strain in a controlled fashion by attaching the device to a piezo[1]. In Si(111) MOSFETs, inhomogeneous strain at the Si-SiO_2 interface has been considered the likely source of valley splitting leading to observations of two-fold valley degeneracy except in samples specially prepared to minimize this strain[3]. We expect strain effects to be minimal in our H-Si(111) FETs since they have no barrier material above the channel, our bonded pieces should be well thermally matched (and hypothetical strains due to bonding should be symmetric in any case), and we mount our devices in a plastic jig specifically designed to prevent shifting without straining the sample (see photo in Fig. 3.6 p. 25).

2.4.3 Magnetic Field

There are numerous observations of valley splitting induced by strong magnetic fields[12, 1]. Most often this splitting appears to grow linearly with $B_\perp$, though a mechanism for *suppression* of valley splitting via an applied $B_\perp$ has also been proposed[15].

Within the effective mass approximation, Stern and Howard [18] show that an in-plane component of B can cause a lifting of the valley degeneracy. Specifically, for an arbitrary B field they show a correction to the 2DES energy of

$$\Delta E = \frac{e^2}{2}(\langle z^2\rangle - \langle z\rangle^2)\left(\frac{(B_y - \frac{\mathbf{W}_{23}}{\mathbf{W}_{33}}B_z)^2}{m_1} + \frac{B_x^2}{m_2}\right) \tag{2.14}$$

where the coordinates are aligned with the principle axes of the valley ellipsoid and the $\mathbf{W}_{jk}$ are components of the inverse mass tensor (see Eq. 2.1). Note that there will be a term proportional to B_yB_z – i.e. linear in B_y – unless the off-diagonal term $\mathbf{W}_{23} = 0$. While this is the case for other multi-valley systems, including Si(100) and AlAs, for Si(111), which has (3D) ellipsoids tilted out of the x-y plane, this term is non-vanishing. This produces an energy component *linear* in the in-plane field and thus *asymmetric* with respect to the tilt angle θ. For each valley pair the in-plane field components B_y and B_x will be different, leading to three different energy bands.

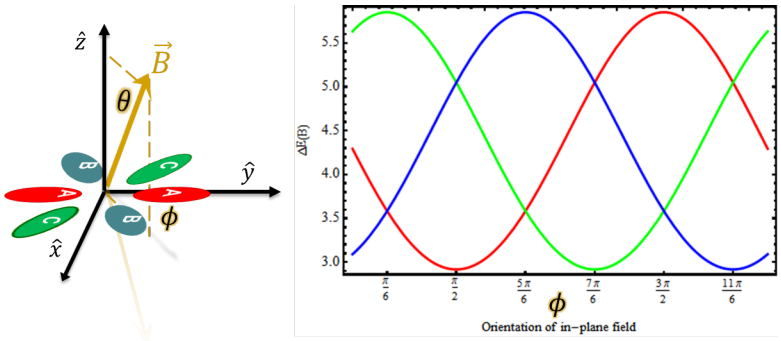

Figure 2.6: Energy correction from Eq. (2.14) for a field B=12 T tilted $\theta = \pi/9$ (20 degrees) from $\hat{z}$ vs the orientation ϕ of the in-plane field. The three valley pairs are shown in red, green, and blue.

2.4.4 Interface Potential

For 2DESs on Si(100) the interface potential is known to couple the $\pm k_z$ valleys, resulting in the lifting of the twofold valley degeneracy[12]. This should not occur on Si(111) because inversion of the z component of the wave vector does not map any valley onto another valley.

Chapter 3

H–Si(111) Vacuum Field Effect Transistors

In order to measure transport on H-Si(111) surfaces, we require a device platform that meets several criteria: 1) we must preserve the H-terminated free surface, with no material over the passivation layer 2) we must have a means to apply a field perpendicular to the surface to create the 2DES and modify the carrier density without creating leakage paths outside the intended channel 3) we must be able to make electric contact to the 2DES without exposing the H-Si surface to contamination.

To do this we use two silicon substrates bonded together to preserve the H-Si(111) surface within a small vacuum cavity inside the device. This chapter will describe the design of this device, the process of fabrication, and means of characterization. Additionally, we present discussion of some of the design changes that have been implemented over the course of this work.

3.1 Device Design

The H-FET is built from two separate silicon substrates. The first is the H-Si(111) sample whose surface serves as the channel for our 2DES. The second substrate is a piece of Silicon-on-Insulator (SOI) with a $\sim$0.7 μm recess etched into its surface. These pieces are brought together in a vacuum chamber, where their surfaces bond together via Van der Walls forces. This leaves an encapsulated vacuum cavity that will serve as a gate dielectric and preserve the H-Si(111) surface from degradation when the device is removed from vacuum.

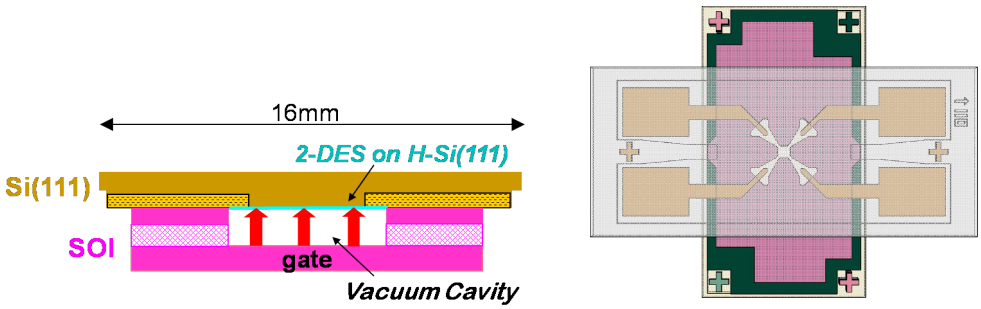

Figure 3.1: **a)** Cross-section and **b)** overhead view of bonded device

3.2 Wafer direct bonding

When two smooth, flat, clean surfaces are brought in contact, they will adhere to one another due to van der Waals forces without the need for applied force, thermal treatment, or adhesives[19]; this is known as *direct bonding* or *contact bonding* and is widely used in applications from the fabrication of integrated circuits to transfer printing of micro-electromechanical systems. References [19, 20] provide a detailed overview of both the principles and applications of this technique. There it is emphasized that successful bonding requires that the surfaces to be joined are:

- **clean** — Particles on the surface can produce bubbles in the bonded interface several orders of magnitude larger than the particle size.
- **flat** — Variations in wafer thickness across the sample can create vacancies/gaps at the bonding interface.
- **smooth** — Rough surfaces cannot come close together and have less overlapping surface area. The rms roughness should be less than $0.5 - 5$ Ådepending on the surface chemistry.

Although we have not studied the hermeticity of the cavity bond, contact bonding has been shown to preserve H-Si(111) even when the bonded samples have been exposed to ambient conditions for weeks[21]. Our only probes of bond quality (apart from the initial infrared (IR) image taken at the time of bonding (Fig. 3.2)) are device mobility over time and, for retired devices, AFM of the Si(111) surface after breaking the bond open. While

some samples, particularly early ones, do show some degradation in mobility when exposed to room temperature conditions for many weeks or months, the best devices have proved to be very robust, enduring numerous thermal cycles and transfers between fridges with negligible mobility loss. When opened and imaged a year or more after fabrication such devices still show clean surfaces and clear atomic steps.

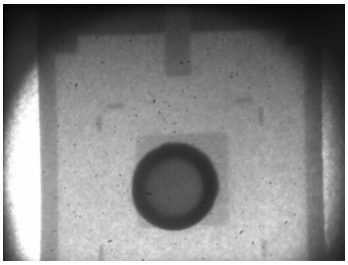

Figure 3.2: Infrared image of an early bonded device (npvt26). The very dark circle in the center is the sapphire hemisphere above the sample used to initiate bonding.

3.3 Device Fabrication

This is a general overview of our fabrication process. See Appendix B for details.

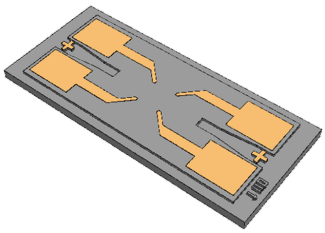

Figure 3.3: Processed Si(111) sample (ver 3.75). Orange regions indicate P-implanted Ohmic contacts. Size is 16 mm × 7 mm.

We begin fabrication with the (111) oriented silicon wafer, whose surface will be H-terminated and serve as the channel for our 2DES. After growing a thermal oxide on the surface, we create a mesa via Reactive Ion Etch (RIE) to protect the surface from damage and particulate near the sample edge. Then we use selective ion implantation to create four Ohmic contacts which we will use to contact the 2DES. The implanted contacts provide metallic behavior without the vulnerability that metals would have to the cleaning solutions we employ. After activating the implants, we clean the sample using a series of

solvents*, Piranha etc.(§C.2.1), and megasonic† deionized water (DI). Finally, the sacrificial oxide is removed with HF and the exposed silicon surface is passivated and flattened with NH_4F. Since the quality of the silicon surface is very sensitive to dissolved oxygen in our solutions[8], we now perform this final step in a nitrogen glovebox with ambient O_2 levels $\lesssim$1 ppm‡.

Figure 3.4: Schematic of a Silicon-On-Insulator (SOI) wafer used to create the FET gate.

The second substrate is a piece of commercially purchased Silicon-on-Insulator (SOI), which consists of 340 nm layer of p-type silicon atop 400 nm of SiO_2 (the buried oxide or 'BOX' layer), which in turn sits on a 450 um thick 'handle' wafer of p-type silicon. See Fig. 3.4. We use this piece to build the gate as well as the cavity that will preserve the H-Si(111) surface. First we implant the top silicon layer (the *shield*) and the lower handle wafer (the *gate*, just below the BOX) with Boron to create two conducting layers. We then grow a thin thermal oxide on the top surface and activate the implants (§B.2.3).

The next phase of fabrication involves a series of plasma etches through the layers of the SOI. As with the (111) sample we etch material from the sample perimeter through the top layers and past the gate implants, leaving a mesa isolated from the sample edge. We next etch a smaller mesa in the top Si layer further recessed from the edge to prevent gate-shield leakage. Finally, we etch a cavity in the center of the SOI through the silicon and BOX layers to the implanted handle layer (see Fig. 3.5). Again we clean this sample with solvents, Piranha, and DI.

We then place the two samples in a vacuum chamber and pump down to 10^{-6} torr. The samples are brought in contact by slowly raising a sapphire cylinder supporting the SOI until it meets the Si(111). If both samples are extremely clean and atomically flat (rms roughness < 5 Å) the surfaces will bond together due to Van der Waals forces. Because silicon is transparent at infrared wavelengths ($\gtrsim 1\mu$m), we can verify this bond using an IR

*acetone, methanol, isopropyl alcohol (IPA)

†high–frequency (∼MHz) ultrasonics

‡Prior to the introduction of the glovebox (circa 2008) we sparged our NH_4F with N_2 gas ∼1 hr prior to use, with moderate success.

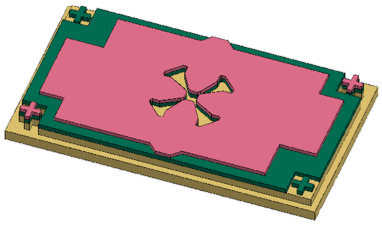

Figure 3.5: Processed SOI sample (ver 8). Top silicon layer is pink, buried oxide layer is green, and the handle wafer is tan. Size is 6.5 mm × 12.5 mm.

camera (Fig. 3.2).

Once the device is bonded, we can remove it from the vacuum and mounted for measurement. Gold wires are attached to the four Ohmic contacts on the Si(111) and the gate and shield layers of the SOI via indium solder. We place the device in a plastic jig which in turn is screwed in to a 20 pin header; the jig helps protect and immobilize the device without adding strain at low temperature. We typically mount a Hall sensor to the header as well to provide confirmation measurements of our magnetic field.

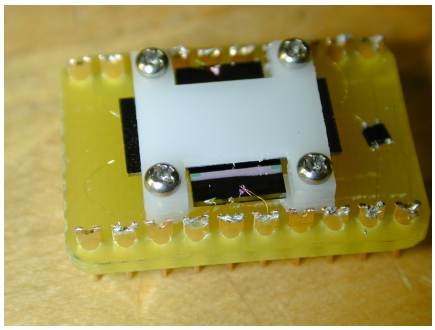

Figure 3.6: Bonded device (npvt75) wired and mounted for measuring

3.4 Surface Characterization

It is often useful to characterize our (111) surface without making a full device to check process and wafer quality/parameters. For this we use Atomic Force Microscopy (AFM) to image the Si surface. This allows us to see atomic steps (and thus measure the miscut angle of the wafer), measure surface roughness, inspect for contamination, verify smooth topography at the contact edges, etc. Unfortunately, this cannot be performed on the exact Si(111) samples used for devices as those surfaces must be bonded immediately

following H-termination. AFM involves too much exposure to ambient air and too much time following passivation and risks contamination or handling error. We therefore must rely on imaging similar silicon samples from the same wafer or debonding a device to image the inside (usually reserved to autopsy a no-longer-working device).

3.4.1 Topography — an Aside

We have observed that the doped contacts on the Si(111) are often highly disordered, very rough, and sometimes at a different elevation from the undoped Si. This was first seen with proximity doped samples, wherein a doping wafer was coated with spin-on dopant and placed a few hundred microns above the target sample (which had a suitable mask). The wafers were heated in the tube furnace or Rapid Thermal Annealer (RTA), allowing dopants to diffuse out of the source wafer and into the target sample. This was found to create extremely dirty contacts. We also found that high temperature exposure to H_2, the ambient gas used in the RTA, created an insoluble translucent brown film on the device that we could not remove with any of our known cleaning methods.

We then moved to ion-implantation of the contacts, experimenting with arsenic (As) and antimony (Sb) as well as phosporus (P). The implantation services required outsourcing (see C.5), as we do not have such capabilities at LPS. While there was an improvement in cleanliness and bondability, AFM inspection revealed serious problem at the contact edge (Fig. 3.7).

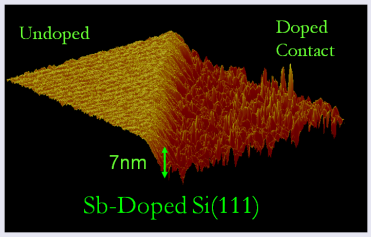

Figure 3.7: AFM of Sb-implanted contact edge under old processing methods.

As shown, the undoped region is very flat and well-ordered, but the doped area is both very rough and offset ∼7 nm below the rest of the sample surface. Such a dislocation

could allow contamination to leak into the cavity or may impair Ohmic contact to the 2DES. After continued investigation we found that this topography effect could be mitigated by sticking with phosphorous implants, reducing the implant density (from $\sim 10^{15}$ cm^{-2} to $\sim 4.5 \times 10^{14}$ cm^{-2}), and ensuring a long (40+ min) high-temperature (950° C or higher) anneal during post–implantation activation.

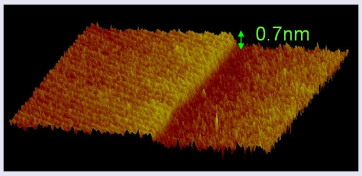

Figure 3.8: AFM of P-implanted contact edge after modifications to anneal and etch parameters.

Later we found that the RCA clean (SC1, see §C.2.2) was another major culprit: it seems that the RCA solution etches through the implanted silicon dioxide much faster than through the unimplanted oxide. If the solution etches through the SiO_2 layer completely it then etches the underlying doped silicon in addition to leaving the silicon vulnerable to later processing. It has been sown previously that SC1 etches both silicon and SiO_2[8], but the strong differential etch rate does not appear to have been reported. A summary of our (rough) measurements appears below (Table 3.1). It is worth noting that the implant parameters are such that the SiO_2 itself should not contain a very high dose of dopant.

material	**etch rate (Å/ min)**
unimplanted SiO_2	4
'implanted' SiO_2	13
unimplanted Si(111)	7–8
implanted Si(111)	9

Table 3.1: Estimated etch rates of implanted and unimplanted sample regions exposed to RCA clean SC1. The 'unimplanted' values are consistent with those reported in[8]

3.5 Dramatis Personae

Quick guide to the principal devices presented in this thesis:

npvt56

Fabricated: March 2005

Studied: Spring 2005-Fall 2005

Highest mobility: $10,000$

Notes: This is the first device to demonstrate Quantum Hall features. Data appears in [22, 23].

npvt75

Fabricated: Apr 2006

Studied: Apr 2006 to Nov 2006

Highest mobility: $24,000$

Notes: In this device we observed IQHE, transport anisotropy, and measured a base valley splitting of ≈ 7 K. Data appears in [24]

npvt124

Fabricated: Spring 2008

Studied: Spring 2008

Highest mobility: $24,000$ (4 K)

Notes: Sample only studied at 4 K due to fridge problems. Density increased until gate breakdown ($\sim 10^{12}$ cm^{-2}).

npvt131

Fabricated: Spring 2008

Studied: Spring 2008 to Summer 2009

Highest mobility: $110,000$ (70 mK)

Notes: Strong sixfold degeneracy and valley-valley drag. Published data presented in [25].

Chapter 4

Methods of Experimental Measurement

We now review the core measurements that form the building blocks of the experiments discussed in this text. In contrast to the unique device architecture and rich valley structure on Si(111) the instrumentation and measurement methods we employ in our data collection are quite standard and straightforward. Generally speaking, we vary one or more of temperature T, carrier density n_s, and magnetic field B (total intensity B and possibly orientation θ) and measure device resistance between various contacts.

4.1 Temperature

Four cryogenic systems are used for low temperature measurements:

- A simple dip stick for making quick 4 K measurements. A silicon diode thermometer provides rough temperature confirmation.
- An Oxford Heliox™helium-3 system for quick-turnaround characterization down to 0.3 K (sample $T \approx$0.3 K) and smooth temperature control. This can be placed in a liquid helium storage dewar or in the 12 T or 15 T magnet systems.
- An old (circa 1991) Oxford Kelvinox™dilution refrigerator ('OldFridge') with a base temperature of $\approx$ 0.3 K and a single-axis mechanical rotation stage. This system is run in the 12 T cryostat.
- A larger, newer (circa 2001) Oxford Kelvinox™dilution refrigerator ('BigFridge') with a base temperature of $\approx$ 20 mK (sample $T \approx$65 mK) . This system operates inside a copper shielded room and has a 6 T magnet.

Most temperature monitoring and control uses ruthenium oxide (RuOx) thermometers thermally anchored to the mixing chamber or helium-3 pot (either directly or at the bottom of the cold finger). In some cases an additional LakeShore RX-202A RuOx thermometer is wired to the sample header to give a better indication of the sample temperature.

4.2 Carrier Density

Control and testing of the FET gate

The gate is controlled using a Keithley 2400 Sourcemeter™. The shield is generally kept grounded, as is the I_- contact on the Si(111). We filter the output through a $\sim$ 16 Hz low pass filter to remove high frequency noise (especially 38.5 and 60 kHz). In most experiments we apply up to 90 V on the gate, largely set by historical observation in early devices that the gate oxide could break at substantially higher voltages, though unbonded SOI substrates can handle a shield-gate voltage of 210 V+ (the limit of the sourcemeter). In practice we have not been able to probe carrier densities substantially higher than 1×10^{12} cm^{-2} without device breakdown.

Figure 4.1, shows the carrier density n_s measured by low T SdH and QHE minima as a function of the applied gate voltage V_g. The charge density scales linearly with V_g as expected for a parallel plate capacitor. Ideally, we expect this data to follow the capacitor equation:

$$n_s = \frac{\epsilon_0 \epsilon}{ed}(V_g - V_{th}) \tag{4.1}$$

where ϵ_0 is the permittivity of free space, ϵ is the dielectric constant of our vacuum cavity (ideally $\epsilon = 1$), d is the cavity depth, and V_{th} is the threshold voltage required to activate the channel. If we set $\epsilon = 1$ and use d and V_{th} as our fitting parameters, we obtain $d = 734$ nm, in excellent agreement with the 735 nm cavity depth measured by profiler for this particular batch of SOI, and $V_{th} \approx 1$ V, corresponding to a density of defect states $< 10^{10}\mathrm{cm}^{-2}$. This high degree of agreement with ideal values is atypical (but then the device mobility was exceptionally high as well); other "good" devices may have V_{th} as high as 10-20 V and effective ϵ as high as 1.1-1.2.

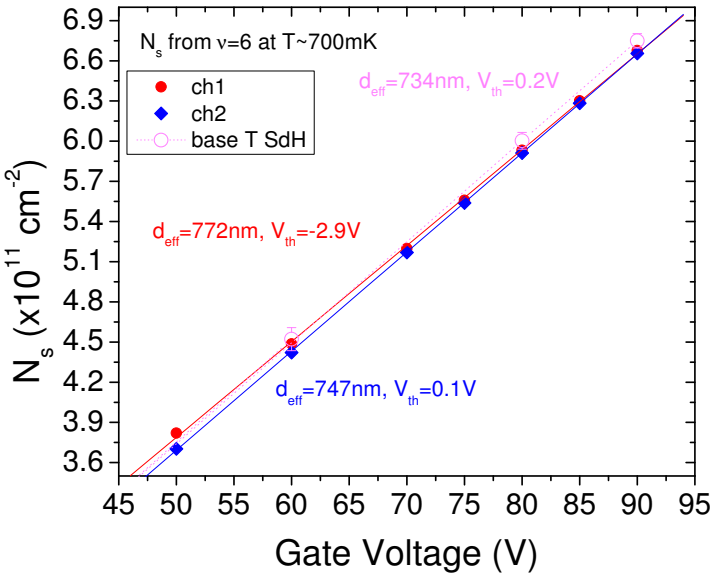

Figure 4.1: n_s vs V_g for npvt131 at 70 mK.

4.2.1 Gate Leakage — An Aside

One of the chief pitfalls in the fabrication procedure has been anomalous leakage between the gate and shield layers of the SOI , often before the Si(111) piece is bonded to the top. We have found several factors contributing to this:

1. Early samples with lower-quality SOI were sometimes prone to pinhole leaks in the BOX layer. This effect seemed to be exacerbated by excessive ultrasonication of the SOI and possible charge buildup during ion implantation

2. Chemical residue from the wet processing (especially piranha clean) can create leakage paths along the sides of the sample. If the residue is small enough, Rapid Thermal Anneal (RTA) at 450° C can mitigate this, but otherwise it can make the leakage much worse. Thorough rinsing with DI water after each chemical clean seems to be the best solution.

3. atmospheric humidity can cause leakage, making it harder to identify other sources.

This was improved by performing leakage tests in a N_2 drybox.

4. small particulate can adhere to the surface or between the SOI and Si(111) in such a way as to short out the BOX. This risk is greatest when the device has left the clean room. Sometimes a blast N_2 can dislodge the contaminant and remove the leakage.

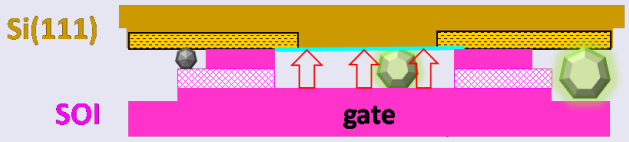

Figure 4.2: Device cross-section showing new SOI design and hypothetical dust particles. The large 'glowing' particles represent contamination that could short out the gate, while the small black particle (left) cannot do so.

Under optimal conditions we should see a (steady–state) gate current $I_g < 1$ pA for 90 V applied between gate and shield. In air at room temperature this may be several nA, but it should vanish in vacuum and at low temperature. In practice, a measured I_g of a few nA at low T is acceptable, as it is usually caused by leakage in the room-temperature connections.

4.3 Resistivity

The primary measurement for all experiments is the resistivity of the 2DES. Fig. 4.3 shows the configuration of contacts to the gated 2DES region, forming a van Der Pauw geometry[26]. This enables us to probe the longitudinal and transverse resistivity and probe the anisotropy of the former.

The current source is the oscillator output of a SRS830 lock-in amplifier across a current-limiting resistor (50–200 MΩ) in series with the sample. The voltage contacts are connected to a low-noise differential amplifier with gain 100, the output of which is input to the SRS830 for phase-sensitive measurement.

In order to measure the different components of ρ in a smooth and automated manner, we add a SRS SIM925 multiplexer between the sample lines and the measurement

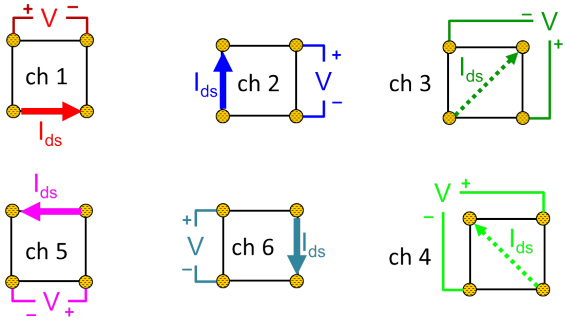

Figure 4.3: Schematic of the sourced-current/measured-voltage 4-wire configurations associated with each of the multiplexer channels. The B field is directed into the page.

instrumentation to allow programmatic switching of the contact assignments.

One caveat about these Hall measurements: note that we are never measuring the transverse resistivity in the same basis as the longitudinal ρ. Our Hall current runs not along x or y but along one of the diagonals shown in Fig. 4.3. If $\rho_{xx} \neq \rho_{yy}$ this change of basis will introduce an error in our measurement of channels 3 and 4:

$$\mathcal{Z}(\frac{\pi}{4}) \begin{pmatrix} \rho_{xx} & \rho_{xy} \\ -\rho_{xy} & \rho_{yy} \end{pmatrix} \mathcal{Z}(-\frac{\pi}{4}) = \begin{pmatrix} \frac{\rho_{xx}+\rho_{yy}}{2} & \rho_{xy} + \frac{\rho_{xx}-\rho_{yy}}{2} \\ -\rho_{xy} + \frac{\rho_{xx}-\rho_{yy}}{2} & \frac{\rho_{xx}+\rho_{yy}}{2} \end{pmatrix}. \tag{4.2}$$

In this rotated basis, the transverse resistance we measure is offset by $(\rho_{xx} - \rho_{yy})/2$. For isotropic systems ($\rho_{xx} = \rho_{yy}$) this error vanishes, but this is not generally the case for our experiments. Fortunately, the orthogonal measurement $\mathcal{Z}(-\pi/4)\rho\mathcal{Z}(\pi/4)$ produces the opposite error. Thus we can average the results of our measurements on channels 3 and 4 to obtain the correct Hall value. Alternatively we can compute the error given ρ_{xx} and ρ_{yy} and re-align the measurement directly.

4.4 Magnetic Field

The magneto-transport data presented here was taken in superconducting electromagnets installed in their respective cryostats. These included a 12 T Oxford magnet, a "15 T" (9 T in practice) Cryomagnetics, Inc. magnet, a 12 T Scientific Magnetics system, and a 6T magnet from Oxford. In all cases the magnets were controlled with an Oxford

IPS-120™Magnet Power Supply. Often a Lakeshore HGT-2100 Hall resistor was mounted next to the sample to verify the field at the device* and, for the 'OldFridge' system, to check the orientation of the tilt stage.

The older Kelvinox dilution fridge ('OldFridge') contains a pulley-controlled rotation stage (single axis) which allows for rotation of the device orientation with respect to the magnetic field (which is always vertical along the dewar axis). A linear motion feed-through at the top of the cryostat moves the pulley through ∼1.25" or ∼115 degrees. This method is subject to some backlash, making it necessary to carefully monitor the Hall voltage of the device and Hall sensor to determine actual orientation. Heating due to this motion can also affect the device signal, so the rotation must be done slowly and while monitoring the temperature; the Hall sensor is fairly insensitive to thermal changes, so it gives a more reliable signal during this process. For the tilted field data presented here, rotation was controlled by hand. We have since added a stepper motor control for automated rotation, but this has not yet been used substantially.

"Four knobs"

The four parameters T, n_s, B and θ together with the contact configuration constitute our primary toolbox for controlling our 2DES. There is nothing particularly exotic about this set of "knobs", and there are not many to choose from, but it is more than enough to span a wide territory of previously–unexplored physics. Even without the tilt stage the parameter space is large enough that it is not typically feasible to map it completely for each device†. Thus the real trick is to choose the right slices through the parameter space to find the most interesting. informative, and novel data, adapting one's strategy in response to the unfolding data set while remaining focused on the overall picture.

*This verification is not normally necessary but was quite important when using the high–inductance (121 H) Cryomagnetics magnet as the field measured at the sample could lag the applied field by 15—30 min.

†The major constraints on the rate of data acquisition are the time constant of the low-frequency lock-in, the magnet sweep rate, and the thermal response time of the fridge.

Chapter 5

Resistivity of Electrons on H-Si(111) at Zero Magnetic Field

Although most of our work has focused on magneto-transport effects, there are still many useful properties to measure at zero field. Our primary control parameters in this case are temperature and carrier density.

5.1 Characterization at 4 Kelvin

Measurements at 4 K serve as a useful benchmark of low temperature behavior, revealing many of the basic features of low T transport without the complexity of structure that arises at sub-Kelvin temperatures. Furthermore, with so much variability in base temperatures reached by different fridges and discrepancies between fridge and sample temperature, 4 K is a consistently attainable temperature for comparison across systems.

First we must verify that the device functions as a FET, i.e. that the channel resistance decreases with increasing gate voltage V_g and the electron density increases linearly with V_g as discussed in §4.2. Figure 5.1 shows the carrier density n_s measured by the 4K Hall slope vs. V_g. At this temperature the nonlinear corrections to the Hall slope due to multi-valley effects described in §7.1 are quite small and the n_s values we measure agree well with those obtained from base temperature SdH data.

It is also useful to characterize the device mobility at 4 K. Figure 5.2 plots 4 K mobility vs. density for the devices listed in §3.5.

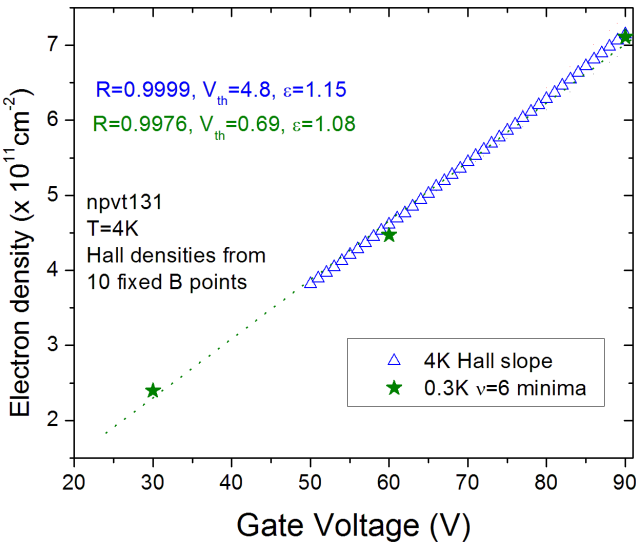

Figure 5.1: n_s vs. V_g plot.

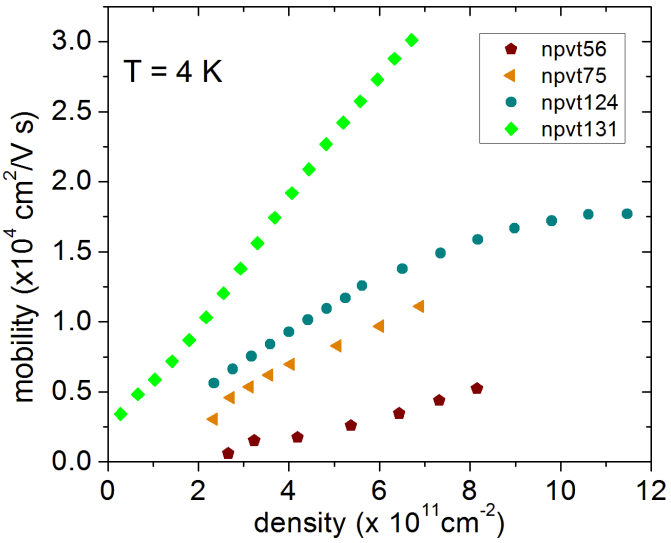

Figure 5.2: Mobility vs density for several devices at T=4 K

5.2 Temperature Dependence of ρ

At a base temperature of 70 mK the mobility μ has increased dramatically compared with its 4 K value (Fig. 5.3). We also find that ρ continues to decrease with decreasing T, a behavior typically labeled "metallic" (Fig. 5.4). At low densities $n_s \lesssim 0.9\times10^{11}$ cm^{-2}, this

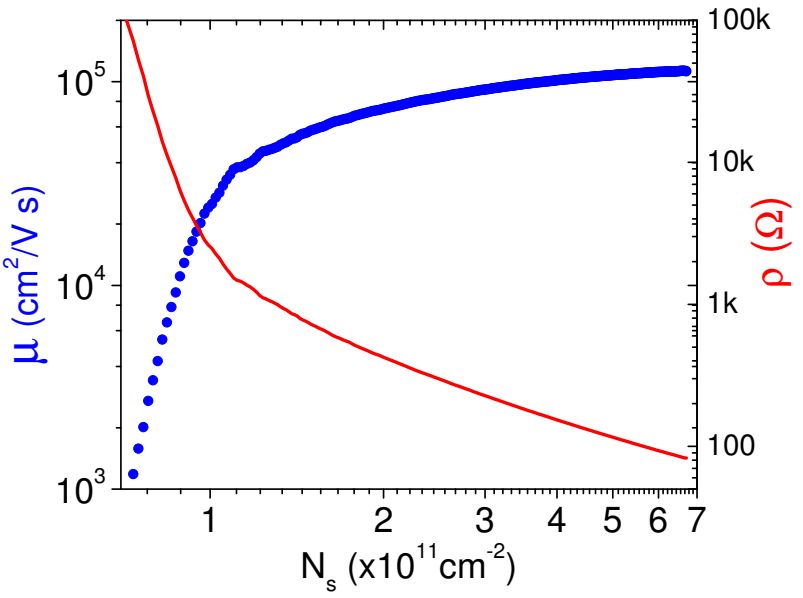

Figure 5.3: μ and ρ vs. n_s at base T

trend reverses and the 2DES becomes *less* conductive as $T \to 0$. This behavior, termed the 2D "Metal-Insulator Transition" or MIT has been observed in many 2D systems [27, 28, 29] but the exact nature and origin on the phenomenon remains the subject of considerable debate [30, 31, 27, 32]. While we have not studied this effect in enough detail to weigh in on the various theoretical models, we do wish to show robust data we have taken and mention some notable features.

The strong "metallic" behavior has been consistently observed in all of our working H-Si(111) devices over several years. The "insulating" behavior has only been reliably observed in the very high mobility device `npvt131`, largely because the low threshold voltage V_{th} and reduced capacitance and lead resistance compared with previous device designs enabled us to probe much lower densities than has been possible in other devices. At intermediate densities ρ is not monotonic in T. Similar behavior is discussed in Ref. [32], which argues that such "crossover" effects appear as T moves through competing energy scales.

To better visualize the MIT, Fig. 5.5 shows the derivative dR/dT as a function of n_s and T. Where $dR/dT > 0$ (red regions) the 2DES is "metallic", while the "insulating" behavior occurs where $dR/dT < 0$ (blue). The reentrant "metallic" behavior for R_{xx} at

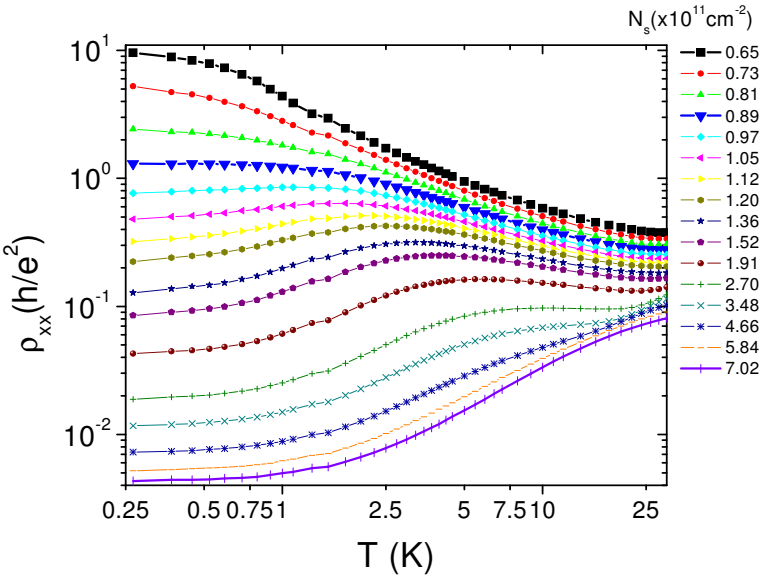

Figure 5.4: Resistivity vs. T at several densities.

high T is associated with a curious non-monotonic n_s dependence observed on that channel at high T. We do not understand this and will touch on it again only briefly in §8.3.

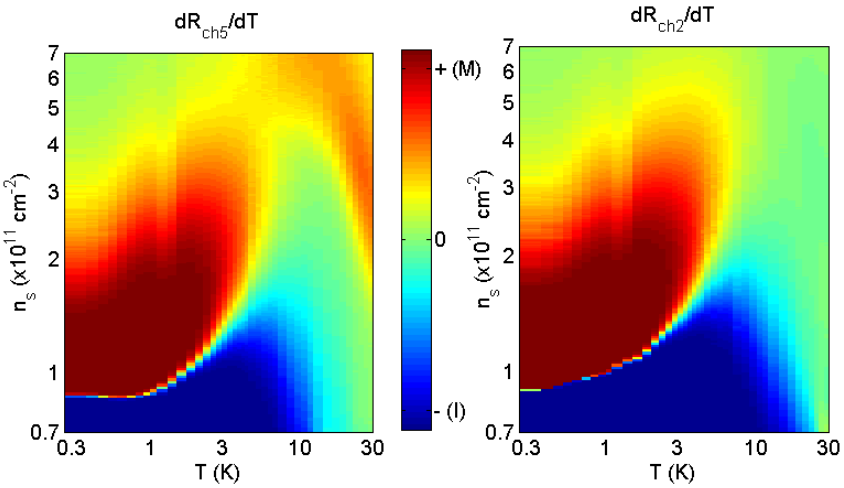

Figure 5.5: d/dT of R_{xx} ('ch5') and R_{yy} ('ch2') vs n_s and T. Red regions indicate "metallic" behavior while the "insulating" region is blue.

Because the valley degeneracy g_v directly enhances the density of states (Eq. 2.9), a large g_v should lead to stronger screening[4]. The larger effective mass of Si(111) compared with Si(100) and the reduced dielectric constant κ of our vacuum cavity compared with SiO_2 further contribute to the enhancement of charge screening (here parameterized in terms of

the Thomas–Fermi screening wave vector q_{TF}[31]):

$$\frac{q_{TF}}{2k_F} = \frac{e^2}{\hbar^2} \frac{(g_s g_v)^{3/2} m^*}{\sqrt{4\pi n_s}\kappa} \tag{5.1}$$

For sixfold–degenerate Si(111) this value is $\approx 12\times$ larger than for Si(100) and $\approx 136\times$ larger than n-GaAs at the same density. This enhanced screening in turn is predicted to result in strong "metallic" T dependence at low temperatures, and our results in Fig. 5.4 appear qualitatively consistent with the predictions of Ref. [4].

Another component of the observed T dependence may be due to the T–dependent suppression of multi-valley effects, which we will discuss further in Chapter 7.

Chapter 6

Magneto-Transport of Electrons on H-Si(111)

Having examined the zero-field behavior of these devices, in this chapter we will now investigate the response of our 2DES to an applied B field. These magnetoresistance measurements comprise the foundation for our experimental work, providing the most information about the electronic structure of electrons on H-Si(111). The B field quantizes the 2D energy spectrum and gives us a means to control the inter-level spacing (§2.2.1). In weak fields we can separate the levels just enough to observe their primary structure and learn about the zero-field properties (§6.1). At higher fields we can fully separate the energy levels to trace the evolution of particular gaps, piece together an understanding of the valley splitting, and seek out novel system states in the strongest fields (§6.2).

6.1 Shubnikov–de Haas oscillations and g_v

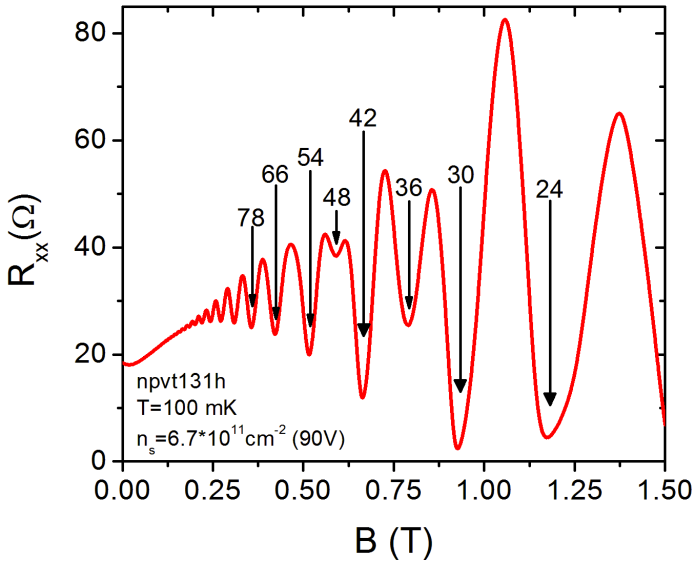

Figure 6.1: Ch1 (R_{xx}) SdH signal showing sixfold valley degeneracy.

Figure 6.1 shows a trace of R_{xx} vs B for npvt131 at a base temperature of $\sim 100\,\mathrm{mK}$.

Beginning at ≈0.1 T one sees clear oscillatory behavior. Finding the value of B at each minimum and computing $\nu = \frac{hn_s}{eB}$ we find these oscillations have a period $\Delta\nu$ of 11.94±0.04, in good agreement with the 12-fold degeneracy expected for non-spin-split Si(111). Above ≈0.5 T the period becomes 5.91±0.1 as spin degeneracy lifts.

Using standard values for m^* and g^*, the cyclotron spacing is[12]

$$\Delta_c = \frac{\hbar e B_\perp}{m^*} = 3.752 \text{ K/T}. \tag{6.1}$$

and the spin splitting is

$$\Delta_Z = \frac{g\hbar e B_{tot}}{2m_e} = 1.343 \text{ K/T}. \tag{6.2}$$

Since we are presently considering only fields applied perpendicular to the sample, we will drop the subscripts on B for convenience. Note that the spin splitting will reduce the energy gap between Landau levels

$$\Delta_c\prime = \Delta_c - \Delta_Z = 2.409 \text{ K/T}. \tag{6.3}$$

Oscillations become visible when the energy gap becomes larger than the level width Γ. In §6.1.1 we will use temperature dependence measurements to calculate Γ, but for now we can estimate it from the onset of the SdH signal:

$$\Gamma \approx (\Delta_c\prime \text{ or } \Delta_Z \text{ at first oscillation}) = 0.1{-}0.2 \text{ K}. \tag{6.4}$$

From the preceding calculations we would expect the cyclotron gaps to dominate, with minima appearing at ν=36, 48, 60, 72 etc. Instead we observe gaps at odd multiples of 6: ν=30,42,54,66.... This likely indicates an enhancement of Δ_Z relative to Δ_c, possibly including effects of B-dependent valley splitting. This phenomenon has been previously observed in Si(111) MOSFETs[2] as well as Si(100) MOSFETs[33]. In both cases, however, this was a low-density phenomenon, occurring near the metal-insulator crossover; at higher densities the even gaps again dominated.

The situation becomes even more curious when we examine the SdH data for R_{yy}. As

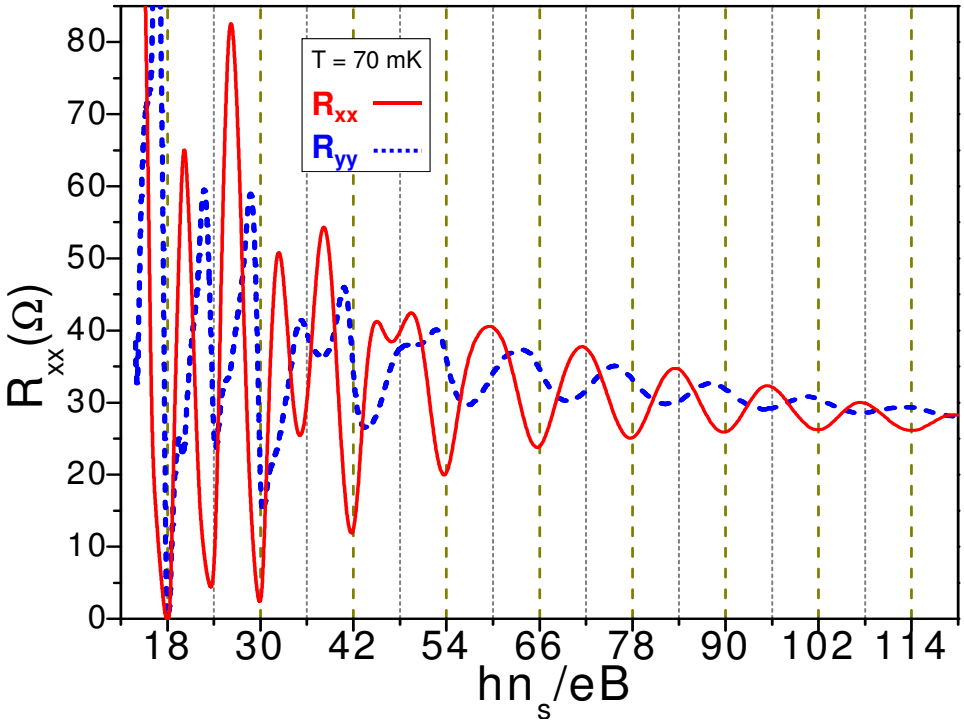

Figure 6.2: Low temperature SdH signals for orthogonal source current configurations. The baseline and period are very similar, but the phases do not match until $\nu \lesssim 30$. This is likely an indication of trace valley splitting enhanced by the applied B field.

is evident from Fig. 6.2 the general trend of both R_{xx} and R_{yy} is similar, but the phases of the two traces are clearly different. Nevertheless, the oscillation period $\Delta\nu$ remains essentially 12 (12.5±0.1; 6.4±0.2 at higher B). This may indicate a very small valley splitting which may be increasing with B.

Such a lifting of the valley degeneracy would entail a slight difference in carrier density between different valleys which should result in beating between distinct frequencies in the SdH data. The fact that we do not observe such beating indicates that either the splitting is much smaller than the level broadening Γ* or that one valley band dominates the SdH signal. In the latter case, if we assume that the anisotropy is maximally sensitive to the valley splitting (i.e. R_{xx} depends only on, say, the upper valleys and R_{yy} only on the lower valleys) this could potentially give rise to a slight frequency difference that would be most

*Another means of estimating an upper bound on the density difference is to note that we could not detect a beating pattern with a period larger than the observed SdH data range. Since we observe single-frequency oscillations over a range $\Delta\nu \sim 150$, $\Delta n_s/n_s \lesssim 0.01$.

prominent at low fields. It is, however, difficult to reproduce the magnitude of the observed phase shift under such a model using a constant splitting consistent with the strongly twelvefold oscillation period. We would therefore like to know just how tightly the SdH data constrains the degree of low-B valley splitting in this device.

6.1.1 Temperature-dependent SdH

The preceding discussion highlights the important role of the level broadening in making sense of our data. Fortunately, SdH oscillations carry information about the level structure as well as g_v. Ignoring spin splitting for the moment, we consider the effects of temperature on the SdH signal [12].

$$\Delta\rho = e^{-2\pi^2 m^* k_B T_D/\hbar eB} \frac{\xi}{\sinh \xi} \cos\left(2\pi \frac{hn_s}{g_s g_v eB}\right) \tag{6.5}$$

where $\xi = 2\pi^2 k_B T/\Delta_c = 2\pi^2 k_B T m^*/eB$ and the *Dingle temperature* $T_D \sim \Gamma$ characterizes the intrinsic scattering that contributes to the level broadening. For fixed T, the B dependence of the SdH amplitudes thus can reveal this intrinsic broadening. This requires that all other parameters are known, including the effective mass m^*. In practice, m^* frequently differs from the value predicted by band structure. If we hold B fixed and examine the T dependence of the SdH envelope function, we can determine m^*. We can then use this value in our calculation of T_D.

More generally, if we have a set of energy levels with spacing Δ the SdH oscillations behave as[12, 34]

$$\Delta\rho = e^{-2\pi^2 k_B T_D/\Delta} \frac{2\pi^2 k_B T/\Delta}{\sinh(2\pi^2 k_B T/\Delta)} \cos\left(2\pi \frac{E_F}{\Delta}\right) \tag{6.6}$$

and we can determine Δ and T_D, the level spacing and the level broadening. If Δ describes not a cyclotron gap but, say, a spin gap, then $\Delta = g^*\mu_B B$ and $\delta \equiv \Delta/B$ gives information about the effective g-factor rather than m^*. For intermediate spacing, δ may depend on both g^* and m^*.

Following standard techniques nicely demonstrated in Ref. [35] we first take R_{xx} and

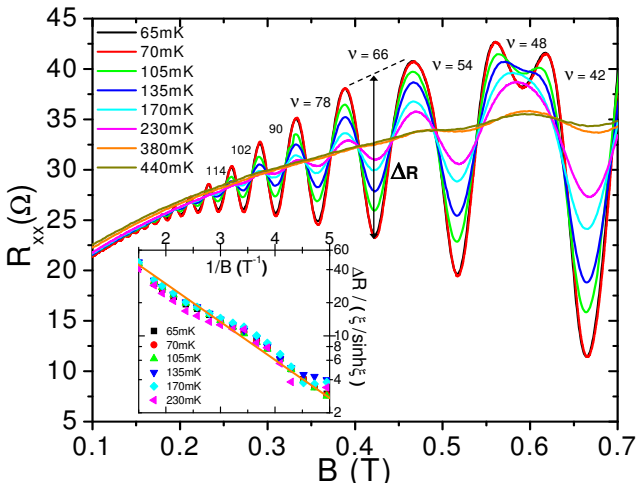

Figure 6.3: Low-B SdH oscillations at several temperatures. To measure the T dependence of the SdH amplitudes we compute the size ΔR of the oscillations via linear interpolation of the minima and maxima across a wide range of ν[35]. We then plot $\Delta R/T$ vs T to extract the gap size $\delta = E_{gap}/B = 2.69$ K/T. **Inset:** Using the calculated δ, we plot $\Delta R/(\xi/\sinh(\xi))$ vs. $1/B$ to compute the quantum lifetime $\tau_q = 12\,\text{ps}$ (equivalently, the Dingle temperature $T_D = 0.1$ K). Note how the data collapse onto a single line.

R_{yy} traces at several temperatures (Fig. 6.3). Then we identify the peaks and valleys of the SdH signal and approximate the envelope function via linear interpolation. We measure the amplitude ΔR from each minimum and maximum to its corresponding point on the interpolated envelope. This gives us

$$\Delta R = R_0 e^{-2\pi^2 m^* k_B T_D/\Delta} \frac{2\pi^2 k_B T/\Delta}{\sinh(2\pi^2 k_B T/\Delta)}. \tag{6.7}$$

Dividing by $k_B T$ gives an expression that depends on T only via the sinh term. For each minimum or maximum, the field B is constant so we can fit the $\Delta R(T)/k_B T$ using Eq. (6.7) to extract the SdH gap Δ. The results are shown in Fig. 6.4 scaled by B.

From the ρ_{xx} oscillations we obtain a value of $\delta \equiv \Delta/B = (2.69 \pm 0.11)$ K/T while the ρ_{yy} SdH gives a value of $\delta = (2.98 \pm 0.40) K/T$. Due to the large experimental uncertainty in the latter measurement, we interpret these results (to first approximation) as indicating an isotropic $\delta \approx 2.7 K/T$ (while allowing for the possibility that the ρ_{yy} data reveals a genuine anisotropic correction at the edge of resolution for this experiment).

Because our gaps occur at odd multiples of six, the simplest analysis would treat them as spin gaps, which would correspond to an enhanced $g^* = 4.0 \pm 0.2$. However, the

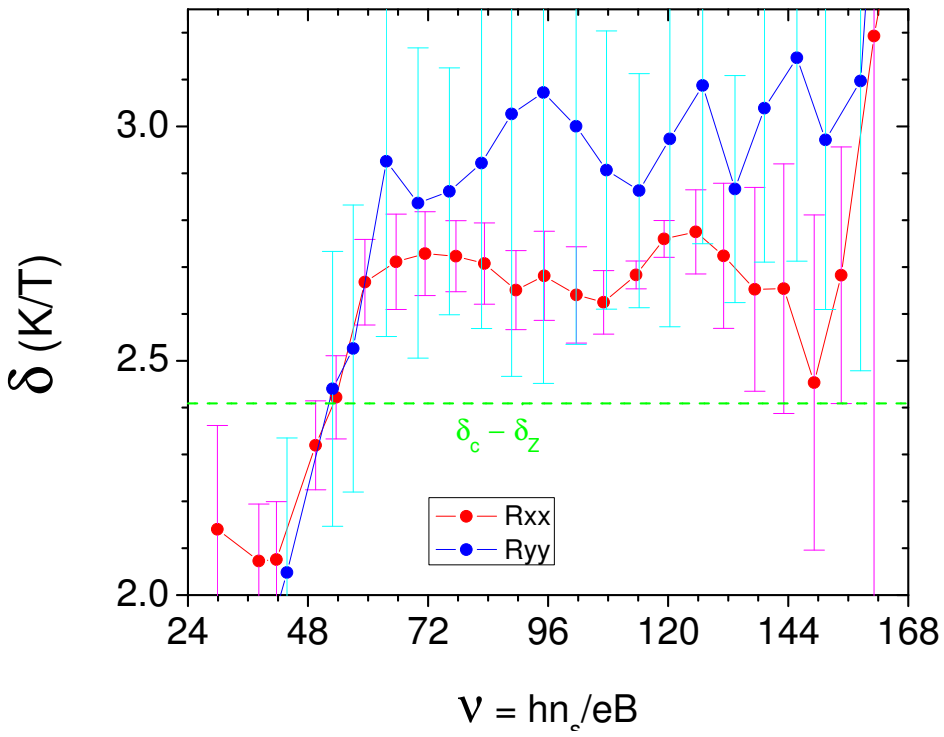

Figure 6.4: SdH gap parameter $\delta \equiv \Delta/B$ measured at several values of ν and for two channel configurations. Error bars indicate the 95% confidence intervals from the numeric fit to Eq. (6.7).Green line shows cyclotron gap reduced by the Zeeman gap for band structure values of m^* and g^*

anisotropy that emerges when $B > 0$ suggests B-dependent valley splitting is also present, confounding a simple interpretation of δ. Regardless of the gaps' origin, we can insert this value into Eq. (6.6) and solve for T_D (and thus an upper bound on the valley splitting). We obtain a value T_D of 0.1 K, which agrees well with our crude estimate in Eq. (6.4). Furthermore, we can compute the *quantum lifetime* $\tau_q = \hbar/(2\pi k_B T_D) \approx 12$ ps, which is $\approx \frac{2}{3}$ the transport lifetime $\tau_0 \approx 18$ ps obtained from zero field transport [†] .

6.2 Higher Field: Quantum Hall Effect

At higher B fields the LLs become well separated and Eq. (6.5) no longer holds. The Hall conductance becomes quantized at integer filling factor and the longitudinal conduc-

[†]We can approximate τ_0 using the mobility data discussed in §5.2, but a more accurate value requires that we account for multi-valley correction effects (§7.2). Thus we ultimately determine τ_0 by solving Eqs. (7.6) and (7.6)

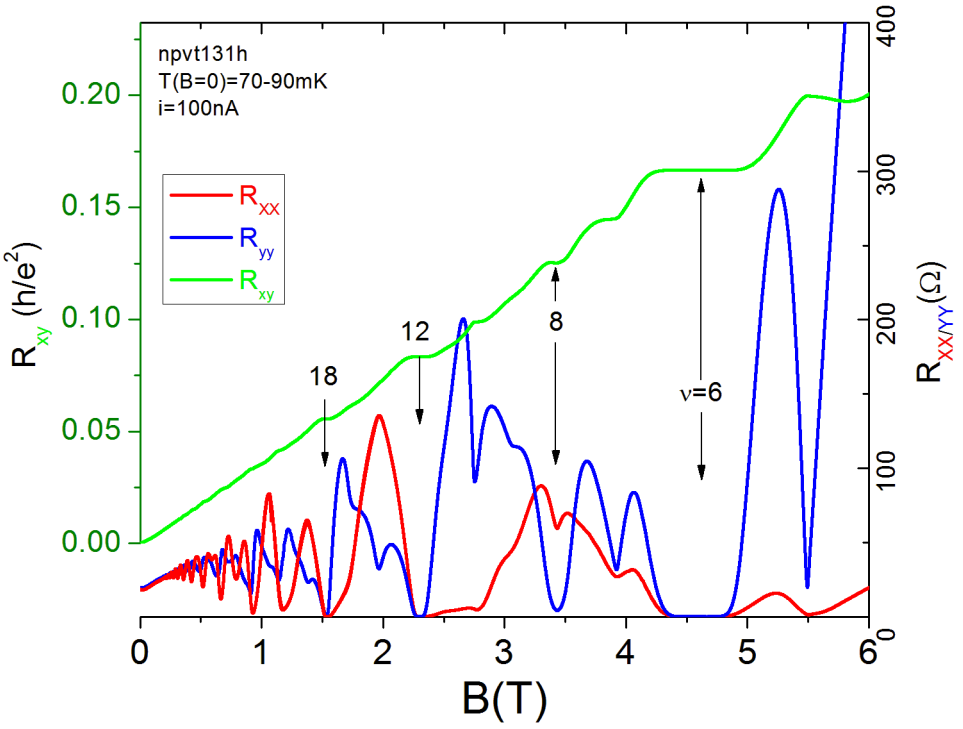

Figure 6.5: Base temperature (∼100 mK) resistivity in the Quantum Hall regime. The transverse resistivity ρ_{xy} displays Hall plateaus at specific fractions $\frac{h}{\nu e^2}$of the resistance quantum while the longitudinal resistivities ρ_{xx} and ρ_{yy} go to zero at the same points.

tivity drops to zero due to the lack of extended states between LLs. Though the physics has changed, the central heuristic for analyzing the data remains the same: when LLs are half-filled $\rho_{xx/yy}$ is maximum, while ρ minima (now going to zero) occur when the highest occupied LL is completely filled.

We see that beyond $\nu = 12$ the sixfold degeneracy lifts to a twofold and eventually single step spacing. Note that the $\nu = 6$ minimum is still quite strong, indicating that the sixfold degeneracy still dictates the leading behavior, with the further splitting a smaller correction. At high field, $\nu = 2$ is especially strong, indicating that the "4-2" gap is the strongest splitting followed by the additional splittings. for npvt131 we can lower the density enough to see a strong $\nu = 1$ as well (Fig. 6.7).

As we see in Fig. 6.8 although there is is quite a bit of variation in the level structure between devices (especially at mid to low fields) the high field structure ($\nu \geq 6$) is quite

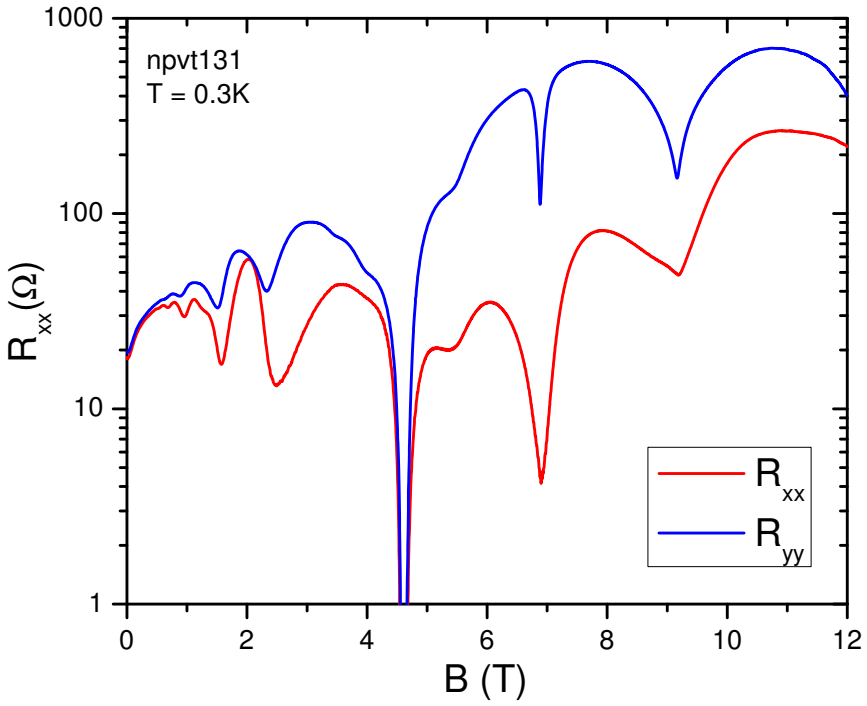

Figure 6.6: npvt131 R_{xx} and R_{yy} up to $B = 12$ T at $T \approx 0.3$ K.

similar across devices, suggesting that at least certain features of the valley splitting (or at least in high fields) may be general and less dependent on device specifics (like miscut or mobility). Thus far we have not probed these gaps extensively, focusing instead on the ample physics that is evident in the low-field region.

We observe gaps at intervals smaller than 6, indicating a lifting of the valley degeneracy. We can separate this into two groups: the even gaps and odd gaps. Even-numbered gaps can arise from a variety of mechanisms that break the sixfold rotational symmetry of the Si(111) system including strain, miscut, and in-plane fields as discussed in §2.4. Depending on the nature of the symmetry breaking this can result in a "4-2" split (i.e. a fourfold degenerate higher energy state and a twofold degenerate ground state), a "2-4" split, or a "2-2-2" split.

Within the effective mass approximation, however, all valley bands will remain at least doubly degenerate due to k-space inversion symmetry. It is therefore interesting that we observe gaps at odd filling factors as well, beginning as early as $\nu = 9$. At present,

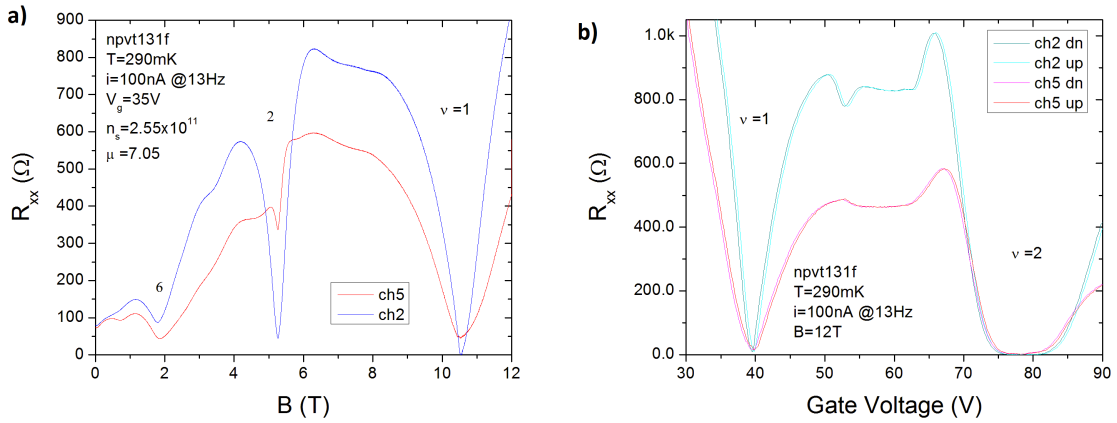

Figure 6.7: Low filling factor gaps seen by a) sweeping B at low density (n_s =2.55×10^{11} cm^{-2}) and b) sweeping the gate voltage at high B.

we do not know what mechanism is responsible for these gaps. As discussed in §2.4.4, the interface–induced splitting observed in Si(100) systems should not apply to Si(111). It is possible that these gaps arise not as a separation between two distinct valley states but as a result of many-body interactions including skyrmions[36] for which valley index is no longer a good quantum number[37].

In §8.1 we present preliminary measurements of fractional quantum Hall states.

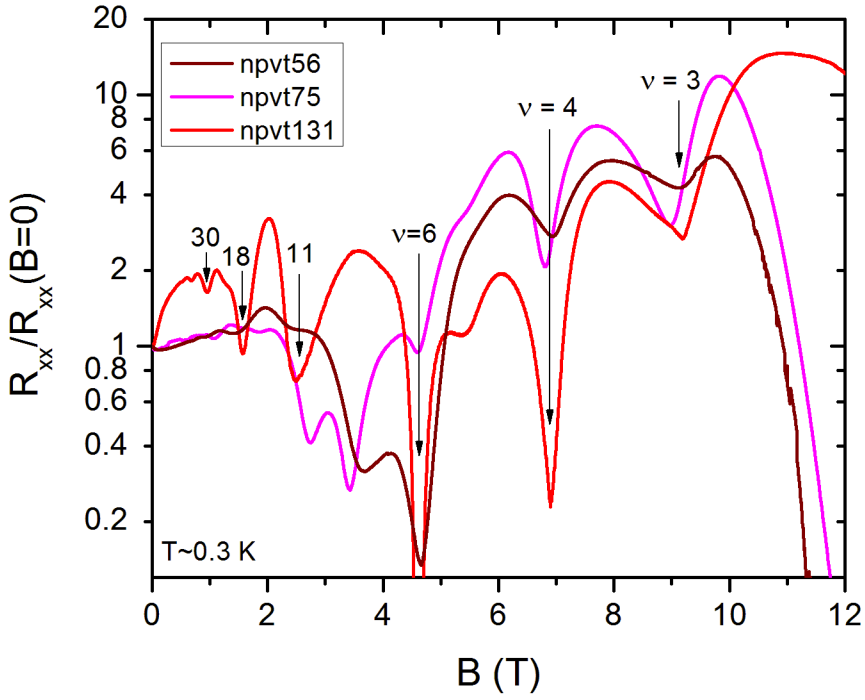

Figure 6.8: R_{xx} vs B for several devices at V_g=90 V. Traces are normalized by their $B = 0$ values.

6.3 Measures of Valley Splitting

In §2.4 we surveyed some of the common sources of valley splitting. We now consider some of the signatures of valley splitting from an experimental standpoint.

6.3.1 Activation energy

The most direct way to measure energy gaps is via activation measurements. At integer ν between energy levels, resistance is thermally activated. The resistance at the minimum is given by

$$R \approx R_0 e^{\frac{\Delta}{2k_b T}} \tag{6.8}$$

where Δ is the gap size, which will generally depend on B and possibly n_s. Thus by following the temperature dependence of the minima we can determine the size of the gap (adjusting

for level broadening). While this provides the clearest measurement of the level spacing, it can be a time-consuming measurement and it requires large fields and well-defined minima. The results are dependent on the value of B, so one must track a given gap at several B points in order to separate the B dependence from any constant gap. Furthermore, because B and n_s scale together we cannot directly separate possible B and n_s dependence without adding tilted field measurements.

6.3.2 Dingle Temperature

As we discuss in §6.1.1 the T dependence of the SdH oscillations can provide information about the level broadening which, while not directly tied to valley splitting, does affect the resolution we can expect for detecting valley splitting via SdH. Simply put, a valley splitting smaller than the level width would not show up in the SdH oscillations. Hence T_D serves as an upper bound on the valley splitting if the SdH frequency indicates full sixfold degeneracy.

6.3.3 ρ_{xx}/ρ_{yy} anisotropy

We show in §A.2 that unequal valley occupation due to valley splitting can produce anisotropy between ρ_{xx} and ρ_{yy}. To a limited extent, we may therefore crudely estimate the valley splitting from this zero field anisotropy[‡]. For the case of two valleys lower in energy than the other four by a gap Δ_{42}, the occupancy of the low-energy pair would be

$$\alpha = 1/(3 - 2\Delta_{42}/E_F). \tag{6.9}$$

If we measure the anisotropy $r \equiv \frac{R_{xx}}{R_{yy}}$, we can estimate the fraction α of electrons in the lowest valley pair as

[‡]This assumes our contacts are oriented such that the measured anisotropy is greatest. If $\hat{x}$ and $\hat{y}$ as defined by our probe orientation lie in some unlucky basis even a significant anisotropic signal could be averaged away in the coordinate frame of our measurement. We expect that by fabricating our samples along a specified crystal direction we can increase the chances that our contacts will lie along an auspicious direction.

$$\alpha = \frac{1}{3} + \frac{\bar{m}}{m_-}\frac{2}{3}\frac{1-r}{1+r} \tag{6.10}$$

and use Eq. (6.9) to get

$$\Delta_{42}/E_F = \frac{3}{2 + \frac{m_-}{\bar{m}}\frac{1+r}{1-r}} \tag{6.11}$$

which would in principle give the gap size relative to the Fermi energy given only the values of R_{xx} and R_{yy} at B=0. In practice Eq. (6.11) overestimates the gap Δ_{42} because it neglects other contributions to resistance anisotropy such as sample asymmetries or contact irregularities. Therefore this calculation is at best an order–of–magnitude consistency check and a quick way to estimate the zero-field valley splitting using only two resistance values prior to making a more thorough measurement.

6.3.4 SdH frequency shift

Since the frequency of the SdH oscillations depends on the valley degeneracy, a lifting of the degeneracy will appear in the oscillations. In the simplest case of a constant (B–independent) gap, we would expect a beating pattern composed from the frequencies associated with each valley sub-band. However, if one sub-band has a significantly higher mobility (smaller T_D) then its SdH oscillations may dominate over the other (in comparison the density of states of low-mobility band blurs to a constant background signal). In such a case, the observed SdH frequency is determined by the spin and valley degeneracies of the high–mobility band *as well as its occupancy fraction* α. Using the "4-2" case above, we find

$$\omega_{\mathrm{SdH}} = \frac{h\alpha n_s}{Beg_s g_v} \Rightarrow \Delta\nu = \frac{g_s g_v}{\alpha} = \frac{4}{\alpha} \tag{6.12}$$

while if the four-valley band (with density $(1-\alpha)n_s$) dominates

$$\omega_{\mathrm{SdH}} = \frac{h\alpha n_s}{Beg_s g_v} \Rightarrow \Delta\nu = \frac{g_s g_v}{1-\alpha} = \frac{8}{1-\alpha}. \tag{6.13}$$

Note that for the equally occupied case ($\alpha = 3$) both equations give the expected result $\Delta\nu$=12. We can thus use Eq. (6.12) or Eq. (6.13) together with Eq. (6.11) to estimate the

(presumed B-independent) valley splitting from the observed SdH signal.

The most important lesson here is not the measurement of Δ (which will be only a rough estimate) but to understand how the SdH period can differ from 6 or 12 *even when all six valleys are occupied*. This point was made clear in analyzing data from npvt75 which featured SdH minima spaced by $\Delta\nu = 8$ (Fig. 6.9)), suggesting g_v=4 under a naive reading of the oscillations. We eventually determined (from activation measurements and numerical modeling of the density of states[24]) that the device possessed a very large ($\sim$ 7 K) "4-2" valley splitting at B=0, which at the high densities where we took most of our data resulted in $\sim$ 50% of the electrons being in the 2 lowest-energy valleys. From Eq. (6.12) $\Delta\nu = \frac{2\times2}{\alpha} \approx 2 \times 2 \times 2 = 8$ in agreement with our observation. The fact that the period was an integer was coincidental. Similar data in npvt56, which featured a much smaller gap Δ_{4-2} ≈2.5 K, reveals a slope of 10.5 (Fig. 6.10).

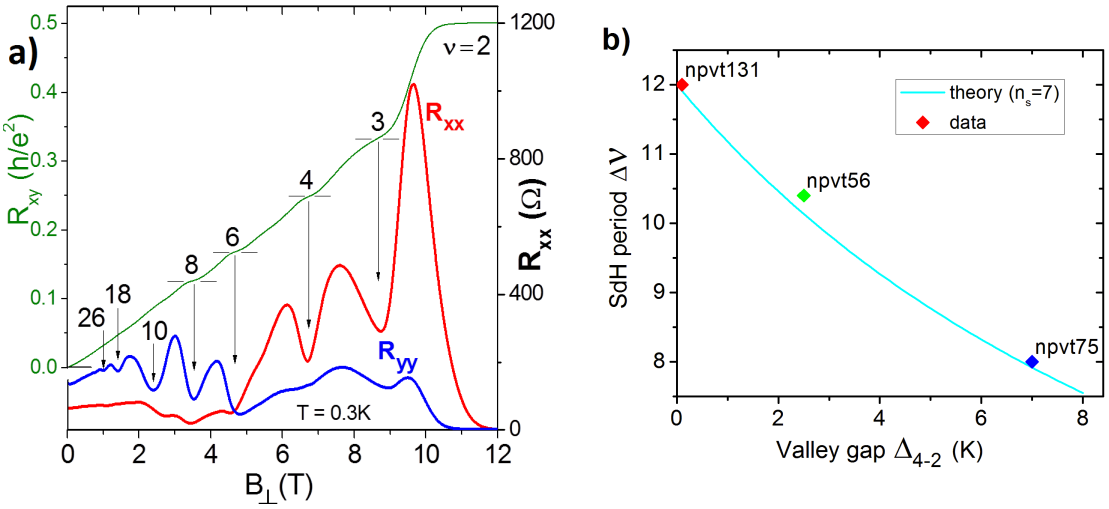

Figure 6.9: a) Magnetoresistance and quantized Hall resistance for npvt75. Note the apparent eightfold SdH period at low B and the strong anisotropy that persists to $B = 0$. b) Observed SdH period vs. measured valley gap for three devices. The orange line shows the prediction of Eq. (6.12) for n_s=7×10^{11} cm^{-2}.

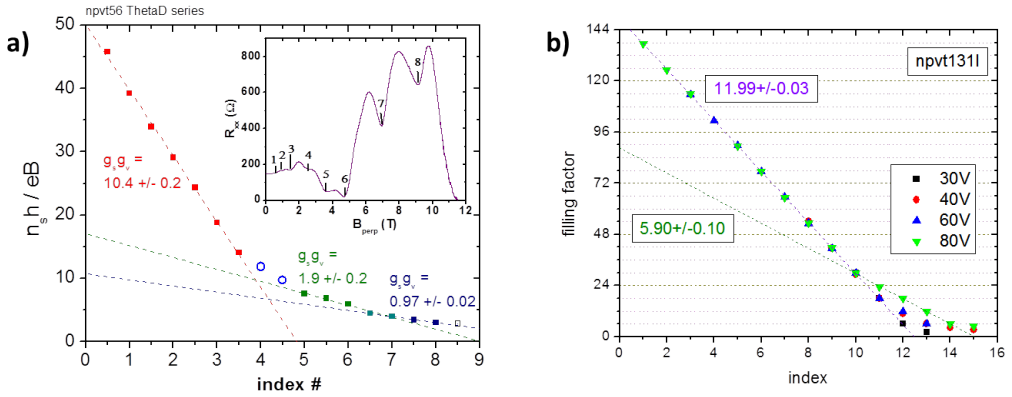

Figure 6.10: Observed minima and maxima for a) npvt56 and b) npvt131. The slopes indicate the total degeneracy ($g_s g_v$) near the indicated filling factors.

6.4 Summary

Magnetoresistance measurements provide a wealth of information about the properties of a 2D charge system. In addition to the techniques discussed here for discerning degeneracy, level broadening, and valley splitting, there are other methods we either have been unable to pursue or have not had time to discuss here. Chief among these are parallel field measurements which can be very informative but for which we have yet to collect unambiguous data. We cover this matter briefly in §8.2.

At very low fields weak localization effects can be used to measure inter–valley transition scattering[38] and may also serve as a sensitive probe of magnetic moments of molecules or devices placed on the Si surface. Commensurability oscillations [39] might enable independent measurement of m_x and m_y by tracking oscillations on the magnetoresistance as the cyclotron orbits shift in and out of resonance with a 1D periodic potential patterned on the surface. Likewise, microwave–, Hall– and phonon–induced resistance oscillations (MIRO, HIRO, and PIRO) indicate resonance of cyclotron energies with applied electric field (AC and DC) and thermal energy scales, respectively[40].

Chapter 7

Valley Drag

The measurements we have discussed so far reveal a lot of information about a previously–unstudied 2DES. However, the techniques and ideas are all quite standard and have been applied to numerous 2D systems for many decades. In this chapter we focus on new effects due to the properties of anisotropic multi-valley systems. The theoretical foundation we invoke is neither new nor particularly exotic; it simply arises from semi-classical transport when assumptions about isotropic single–valley band structure are relaxed. Thus if much of this physics appears novel it is because for most other 2D systems of interest one can safely make such simplifying assumptions while for Si(111) the effects of multiple anisotropic valleys are unavoidable and indeed central to understanding the electronic structure.

7.1 Transport in Independent Valleys

Semiclassical transport in multiple anisotropic valleys can result in additional (non-oscillatory) B dependence in both ρ_{xx} and ρ_{xy} at low fields (this manifests, for example, in the overall positive slope of the data in Fig. 7.1a). This low B behavior results from the presence of multiple anisotropic transport channels. To see this, we first consider the case of equally-occupied, non-interacting valleys that are identical up to rotations $Z(\theta)$ in the x-y plane for some $\theta < \pi$ that defines the rotational symmetry of the whole set* . The basic Drude resistivity for a single valley (with proportional density n_s/g_v) for a coordinate system aligned to the symmetry axes of the valley is given by

$$\rho_0 = \frac{g_v}{n_s e} \begin{pmatrix} \frac{m_x}{e\tau_0} & -B \\ B & \frac{m_y}{e\tau_0} \end{pmatrix}, \tag{7.1}$$

*In the case of Si(111) we have three valley pairs, so $\theta = \frac{2\pi}{3}$ and valley indices range from 1 to 3. The result however does not depend on the number of valleys.

where τ_0 is the transport lifetime associated with momentum transfers from the 2DES to the lattice (and may include intervalley transitions[38]). The resistivity of the j^{th} valley is $\rho_j = Z(j\cdot\theta)\rho_0 Z(-j\cdot\theta)$ and the total resistivity will be

$$\rho = \left(\sum_j \rho_j^{-1}\right)^{-1} = \frac{1}{n_s e}\begin{pmatrix} \frac{\bar{m}}{e\tau_0}\eta & -B\eta \\ B\eta & \frac{\bar{m}}{e\tau_0}\eta \end{pmatrix}, \tag{7.2}$$

where $\bar{m} \equiv (m_x + m_y)/2$ and

$$\eta \equiv \frac{1+(\omega_c\tau_0)^2}{\Phi+(\omega_c\tau_0)^2} \tag{7.3}$$

is the multivalley correction factor. Here $\omega_c = eB/m^*$ is the cyclotron frequency, $m^* = \sqrt{m_x m_y}$, and we define $\Phi \equiv (\bar{m}/m^*)^2$. For $\omega_c\tau_0 \gg 1$, η approaches unity and both ρ_{xx} and ρ_{xy} are given by their respective classical values $\rho_{xx} = \bar{m}/e^2 n_s\tau_0$ and $\rho_{xy} = B/en_s$. At $B = 0$ however, both are suppressed by the factor $(m^*/\bar{m})^2 \leq 1$ (since the geometric mean cannot exceed the arithmetic mean), with equality only in the case of isotropic valleys ($m_x = m_y$).

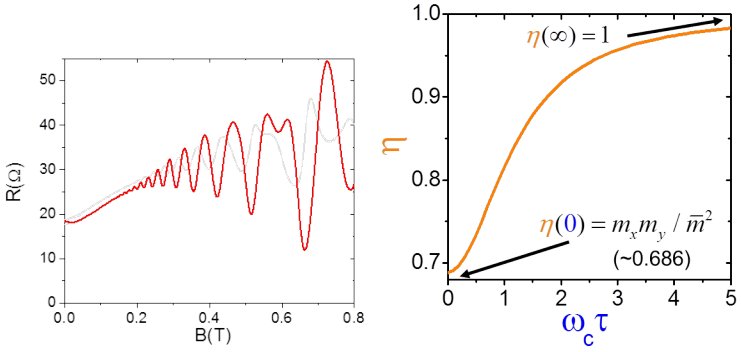

Figure 7.1: a) Low–B magnetoresistance for npvt131. The B dependence of the baseline is due to the effects of Eq. (7.2). b) Multivalley correction factor η vs. the dimensionless parameter $\omega_c\tau$.

In the case of Si(111) we find $\eta|_{B=0} = 0.686$. Because η depends on mass only in *ratio* it remains insensitive to any *isotropic* mass enhancement (i.e. one that scales m_x and m_y equally). Our measurements of "m^*" (via δ) in§6.1.1 are consistent with isotropic enhancement to first approximation, and we will assume this for the rest of the present discussion while noting that there may be corrections due to slight ($\lesssim 10\%$) anisotropy.

Because of mass anisotropy, the current $\vec{j}_i$ in the i^{th} valley induced by an applied field

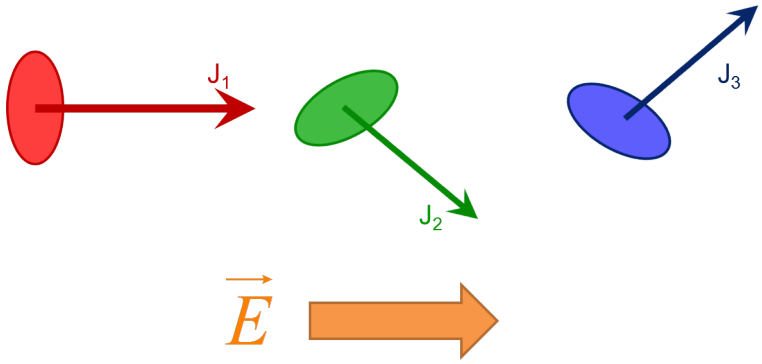

Figure 7.2: Direction of induced current by an applied $\vec{E}$ field. Because of mass anisotropy $\vec{j}$ for a given valley will not be parallel to $\vec{E}$, but symmetry of the valleys ensures that the total $\vec{J}$ does align with $\vec{E}$ for $B = 0$.

$\vec{E}$ will not necessarily flow in the direction of $\vec{E}$ (in fact it will only do so when $\vec{E}$ points along one the the principle axes of M_i). However, the *total* current $\vec{J}$ will follow $\vec{E}$ due to the averaging effect just discussed.

7.2 Valley Drag Model

We have seen how the existence of multiple valleys can produce significant corrections in the low-B resistivity and Hall coefficient. Now we take the reverse and examine how measuring this correction can provide important information about valley-valley interaction effects. The preceding discussion treats the valleys as independent (i.e. non-interacting) channels. Strong valley-valley coupling, as might arise from Coulomb interactions between electrons, will tend to suppress this correction as all electrons move in concert as though in a single isotropic valley. To make this idea more rigorous, we model intervalley effects as a drag interaction between valleys that conserves total 2DES momentum while damping the relative momenta between valleys.

This drag effect is not to be confused with *intervalley scattering*, a lattice-mediated interaction in which electrons scatter from one valley to another. Such scattering involves a momentum change $\Delta k \sim \sqrt{2}k_0$[†], where $k_0 \approx 0.85 \times \frac{2\pi}{a_0} \approx 14\ \mathrm{nm}^{-1} \gg k_F$ corresponds to the conduction band minimum. This requires a short-range interaction potential $\sim 1/\Delta k \sim$

[†]assuming scattering to one of the four 'adjacent' valleys; for 'backscattering' to the opposite valley $\Delta k \sim 2k_0$

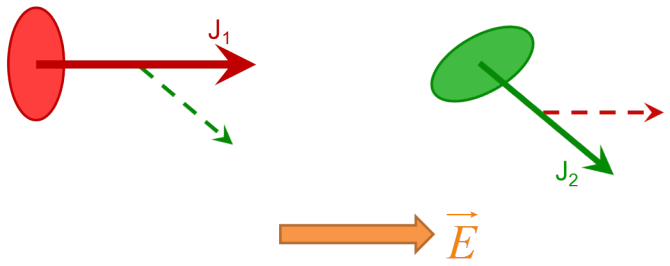

Figure 7.3: Conceptual picture of the valley–valley drag interaction. In addition to the usual anisotropic current response to an applied E field (solid arrows) electrons in each valley feel a frictional tug (dashed arrows) from the current flowing in other valleys.

0.7 Åthat does not conserve 2DES momentum[‡]. By contrast, valley drag is a potentially long–range *exchange of momentum* between valleys with no net momentum transfer to the lattice (Fig. 7.3). Following the kinetic approach used in [41, 42, 43] for multi-band systems we obtain a set of coupled equations:

$$\frac{M_j \mathbf{v_j}}{\tau_0} = e(\mathbf{E} + \mathbf{v_j} \times \mathbf{B}) + \frac{1}{\tau_{vv}} \sum_{k \neq j} \left(M_{jk} (\mathbf{v_k} - \mathbf{v_j}) \right). \tag{7.4}$$

Here M_j is the mass tensor of the j^{th} valley, $M_{jk}^{-1} \equiv M_j^{-1} + M_k^{-1}$ is the reduced mass tensor of the j-k system, and τ_{vv} is the drag relaxation time, which we assume to be isotropic and constant for all valleys. Combining opposite valleys (which have the same M_j), we have three valley pairs. Substituting $\mathbf{j}_k = n_k e \mathbf{v_k} = n_s e \mathbf{v_k}/3$ we then solve the equation $\mathbf{E} = \rho \mathbf{J} = \rho(\mathbf{j_1} + \mathbf{j_2} + \mathbf{j_3})$ for ρ as detailed in Appendix A.3. This gives

$$\rho_{yx} = -\rho_{xy} = \frac{B}{n_s e} \frac{(\Lambda \frac{\bar{m}}{m_1}\gamma + 1)(\Lambda \frac{\bar{m}}{m_2}\gamma + 1) + (\omega_c \tau_0)^2}{\Phi(\Lambda\gamma + 1)^2 + (\omega_c \tau_0)^2} \tag{7.5}$$

and

$$\rho_{xx} = \rho_{yy} = \frac{\bar{m}}{n_s e^2 \tau_0} \frac{(\Phi\Lambda\gamma + 1)(\Lambda\gamma + 1) + (\omega_c \tau_0)^2}{\Phi(\Lambda\gamma + 1)^2 + (\omega_c \tau_0)^2}, \tag{7.6}$$

where $\Lambda \equiv 6 \det(M_{jk}) / \det(M_j) = 6/(3\Phi+1)$ and $\gamma \equiv \frac{\tau_0}{\tau_{vv}}$ characterizes the relative strength of the drag interaction. In the absence of intervalley interaction, $\gamma \to 0$ and we recover Eq. ((7.2)). Conversely, when $\tau_{vv} \ll \tau_0$, $\gamma \to \infty$ and we effectively wash out the multi-valley correction, as shown in Fig. 7.4.

[‡]For an interesting approach to the measurement of intervalley scattering on Si(111) via weak localization see Ref. [38]

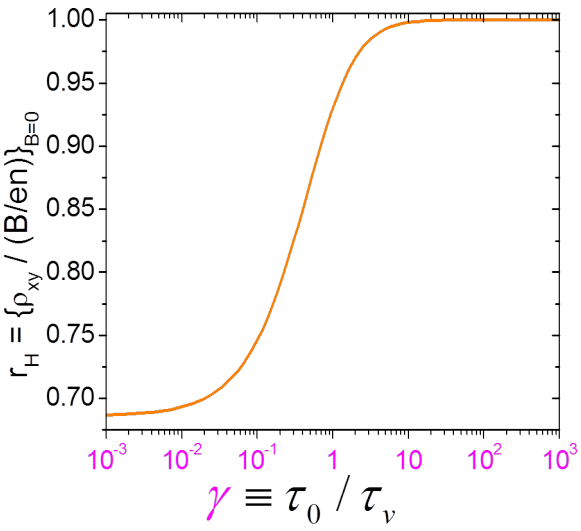

Figure 7.4: Calculated effect on the reduced Hall coefficient r_H as a function of the drag interaction strength γ.

7.3 Measurements of Valley Drag

We have experimentally observed the multi-valley effects of Eq. (7.2) in numerous samples at base temperature. In order to probe the valley-valley interactions, we wish to examine the evolution of this behavior as a function of temperature. We assume that whatever interactions there may be among electrons in different valleys will scale with temperature, allowing us to adjust these interactions via thermal controls.

The correction in Eq. (7.2) is strongest at $B = 0$. By measuring R_{xx} and R_{xy} at $B = 0$, we can use the two equations (7.5) and (7.6) to solve for the two unknown scattering times τ_0 and τ_{vv}. Measuring R_{xx} at zero field is simple enough, but $R_{xy} \to 0$ in this limit regardless of the level of valley-valley drag. What we really want is to measure the Hall slope R_{xy}/B in this limit and compare it to the classical value $-1/n_s e$ that we expect in the strongly interacting limit. We therefore define the *reduced Hall coefficient*:

$$r_H = \lim_{B \to 0} \frac{R_{xy}}{B/n_s e} \tag{7.7}$$

to characterize the interaction. One benefit of this form is that it allows us to compare results at various densities.

Figure 7.5 shows such a measurement of $r_H \equiv \rho_{xy}/(B/en_s)$ vs. T, averaging results

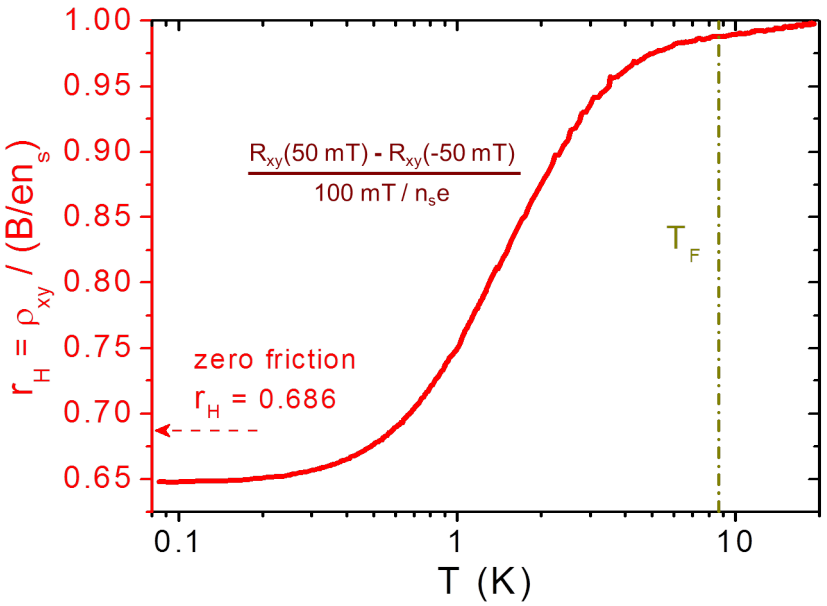

Figure 7.5: Measured value of the reduced Hall coefficient r_H near $B = 0$, which in the absence of intervalley drag deviates from unity due to multi-valley transport effects (Eq. 7.2) . As T increases, intervalley drag erases the distinction among valleys, causing transport to approach single-valley behavior. We use this change in r_H to compute the valley-valley relaxation rate τ_{vv}^{-1}. The dashed arrow gives the predicted value of $r_H = 0.686$ (for $T = 0$, $\tau_{vv} = \infty$), which our model predicts to be a lower bound.

from orthogonal directions (Fig. 4.3) to remove mixing from ρ_{xx} and ρ_{yy} as discussed in §4.3. We determine the density $n_s = 6.7 \times 10^{11}$ cm^{-2} from R_{xx} minima at $\nu = 18$ and $\nu = 6$ and find it to be insensitive to T. B was held fixed at ± 50 mT while T was swept both up and down to ensure consistency. Taking a slope from these points gives a measure of r_H near B=0 while avoiding heating problems observed when sweeping B through 0 T in the "BigFridge".

Above 5 K, r_H is very close to its classical value, while below 5 K r_H drops rapidly with T before settling to a value of 0.65 at $T = 90$ mK. Interestingly, 0.65 is less than the ideal theoretical value of $(m^*/\bar{m})^2$=0.686, though our model suggests the latter value to be a lower bound set by the effective masses of the 2DES.

Because the measurement is based on data taken at $B \neq 0$, we expect this to be an overestimate of r_H, especially at low T where the $\omega_c\tau_0$ terms in Eqs. (7.5) and (7.6) are largest. Indeed when a later cooldown of this device showed $\sim 30\%$ mobility reduction and corresponding broadening of the $B \approx 0$ region, we found $r_H = 0.6$ which is consistent with

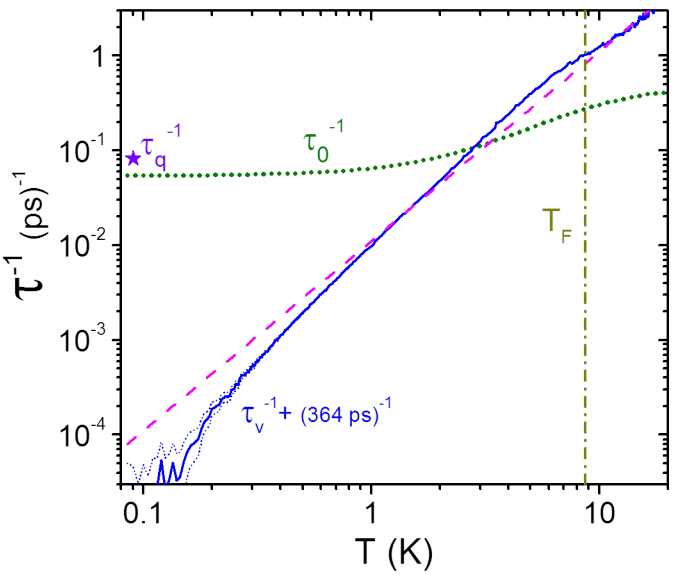

Figure 7.6: Lattice scattering rate τ_0^{-1} (thick green dots) and valley-valley relaxation rate τ_{vv}^{-1} (solid blue) as a function of T. The ★ indicates the inverse quantum lifetime τ_q^{-1} calculated from low-T SdH oscillations. The dashed magenta line shows the damping rate expected for a Fermi liquid (see text). The vertical line gives the Fermi temperature T_F for $g_s g_v = 12$.

the error expected for finite field at the higher mobility.

The simplest adjustment we can make to our model to incorporate this discrepancy in the zero–drag limit of r_H is to allow τ_{vv}^{-1} to approach a constant *negative* value at low T. Negative drag has been discussed as a possible consequence of electron correlation in bilayer systems[44, 45, 46]. Anisotropic mass enhancement could also account for this lower value as an increase in the mass difference $m_y - m_x$ would cause the ratio $m_x m_y/\bar{m}^2$ to decrease. An alternate possibility is that the transport scattering time τ_0 is anisotropic, leading to different scattering rates along the high–mass and low–mass directions. In particular, in the isotropic mean free path limit[47] $\tau_x/\tau_y = m_x/m_y$ and the effects in §7.1 are completely nullified ($r_H = 1$ for all B). Instead, we would have to move in the other direction, resulting in even stronger anisotropic transport than we have in the independent channel case. Preliminary calculations suggest that this would have roughly the same effect as anisotropic mass enhancement.

In Fig. 7.6 we plot the T dependence of the extracted $\tau_{vv}^{-1}+(364\text{ ps})^{-1}$ (offsetting τ_{vv}^{-1} by the base temperature value to remove the divergence) as well as the lattice scattering

rate τ_0^{-1}. The dashed magenta line plots the T-dependent electron–electron (e-e) scattering rate theoretically expected for a single-valley Fermi liquid $\tau_{e\text{-}e}^{-1} \sim (E_F/\hbar)(T/T_F)^2$[10][§], with a prefactor of 1.9 determined by fitting[¶]. Although earlier work has identified the sensitivity of r_H to e-e interactions[49, 50, 51] such corrections are quite small (∼1-4%) at high densities ($n_s \gg n_{MIT}$). Furthermore, these models predict $r_H \to 1$ in the $T \to 0$ limit, whereas our model treats the multi-valley effects of Eq. (7.2) as intrinsic at $T = 0$.

7.4 Summary

We have seen that the existence of multiple anisotropic valleys has a dramatic effect on the low-B transport. This correction is easiest to measure in the Hall coefficient since the "uncorrected" single-valley limit is well-defined and can be independently determined from SdH or QHE features. We have demonstrated how measurement of the reduced Hall coefficient r_H can serve as a sensitive probe of valley–valley interactions and introduced a new "Valley Drag" model for such interactions that agrees well with our data and with the general T-dependent scaling behavior of e-e interactions in a Fermi liquid. Future work will continue to explore this model and possible modifications, including the n_s–dependence of the drag interaction, that might explain our observations of r_H suppression below the lower bound set by the valley effective masses.

[§]We have neglected the additional $\ln(T/T_F)$ correction required for 2D systems[48] because the resulting expression diverges without also including additional constant (in T) terms that increase the number of free parameters used in an already very approximate fit.

[¶]Note however that vertically shifting the $1/\tau_{vv}$ data on a log-log plot can affect the details of the T-dependence, including this numeric fitting coefficient. However, it would not affect the slope (and thus the power-law exponent) which is our primary interest in making this comparison.

Chapter 8

Remnants: Other Measurements

Over the many years we have been studying H-Si(111) devices we have made a number of intriguing observations that we have not yet been able to explore further or, in some cases, to make sense of. The purpose of this chapter is simply to chronicle some of of these unusual and/or under–explored findings. We hope that such a record will serve as:

- a starting point for further investigation
- a comparison for future data
- an acknowledgement of peculiar observations for the benefit of future grad students' sanities
- documentation of interesting but uninterpreted data in the hopes that future theory may shed new light
- a glimpse into the wide range of measurements made on these devices that has not made it in to our published work or this thesis.

8.1 FQHE

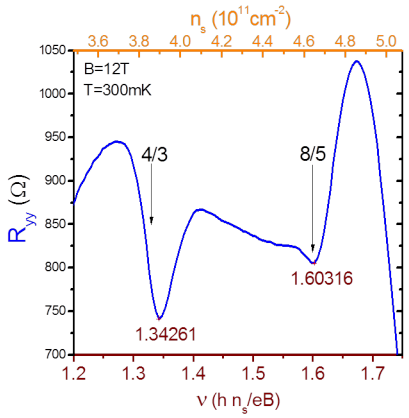

Figure 8.1: Likely fractional quantum Hall states observed in npvt131.

In npvt131 at 300 mK we observed clear ρ_{xx} minima between filling factors $\nu = 1$ and $\nu = 2$ that we believe to be precursors to the $\nu = 4/3$ and $\nu = 8/5$ Fractional Quantum Hall states. These states also appear to be the strongest fractional features between $\nu = 1$ and 2 for strained Si quantum wells as well[52]. While we would fully expect to see more fractional structure in very high mobility H-Si(111) FETs at lower temperature and higher fields, our coldest fridge, "BigFridge", is limited to 6 T. Moderate mobility devices ($\mu \sim 20,000$ $\mathrm{cm}^2/\mathrm{V\,s}$) are too noisy at low densities to reliably discern fractional states. In hindsight, an odd dip observed in npvt75 just past $\nu = 2$ is consistent with ν=8/5 but that data is not sufficiently reliable on its own to justify such an identification.

8.2 Parallel B field

With the sample oriented so that the applied B field runs entirely along the sample plane the cyclotron splitting and Quantum Hall effects are removed. The in-plane field thus serves primarily to spin-polarize the 2DES, though depending on the nature of the valley splitting it may lift the valley degeneracy as well*. This polarization has been shown in other systems [5, 53, 54] to lead to a strong increase in ρ_{xx} and eventual saturation at full polarization. Spin polarization also reduces screening [55] and may play a role in the 2D metal–insulator transition [27, 29]. It would also be interesting to see how spin– (and possibly valley–) polarization affects the drag effects presented in §7.

*The parallel field effect discussed in §2.4.3 would not appear since that term is proportional to B_z.

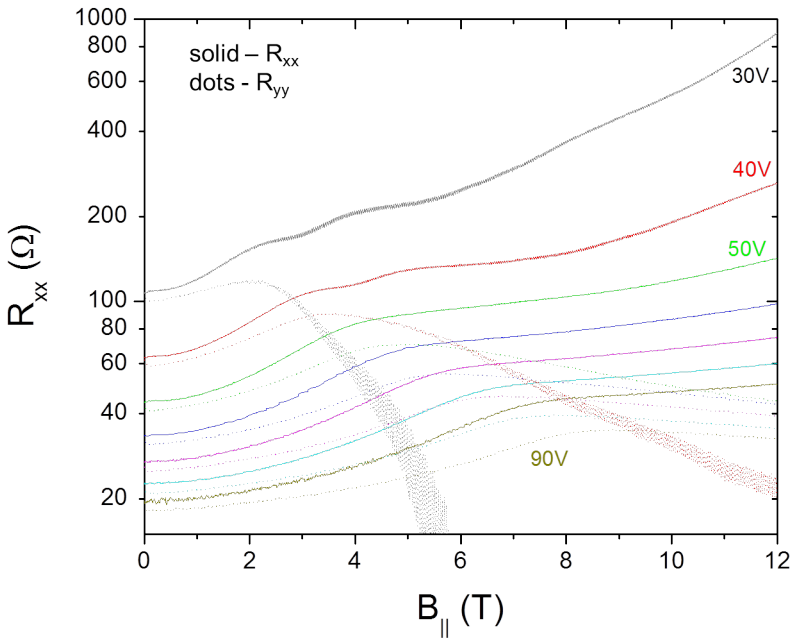

Figure 8.2: Magnetoresistance of npvt131 as a function of in–plane B field. The 'knees' in the R_{xx} (ch5) traces may indicate points of spin and valley polarization. The R_{yy} (ch2) behavior is clearly different, but we cannot rule out contact problems as a contributing factor to this. The complementary channels could not be compared due to one contact having a low resistance to ground; only channels using that pin as (grounded) I_- provided sensible measurements.

8.3 High-T anisotropy

For npvt131 the resistance is very isotropic at low temperatures, but when the system is warmed to much higher temperatures $T \gg 10$ K a new anisotropy appears as shown in Fig. 8.3.

We do not know the source of this behavior as higher temperatures introduce a variety of complicating factors (significant phonon effects, possible parallel conduction channels in the device) that we could ignore at low T. It is worth noting that the observed behavior is linked to a non-monotonic density dependence in the R_{xx} transport (Fig. 8.4).

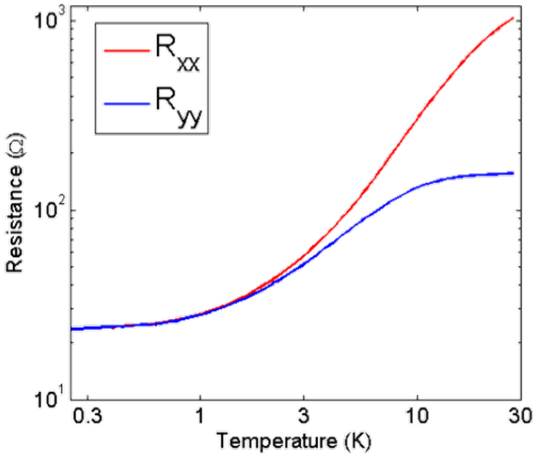

Figure 8.3: Sample resistance vs. temperature for npvt131 at n_s=7×10^{11} cm^{-2}.

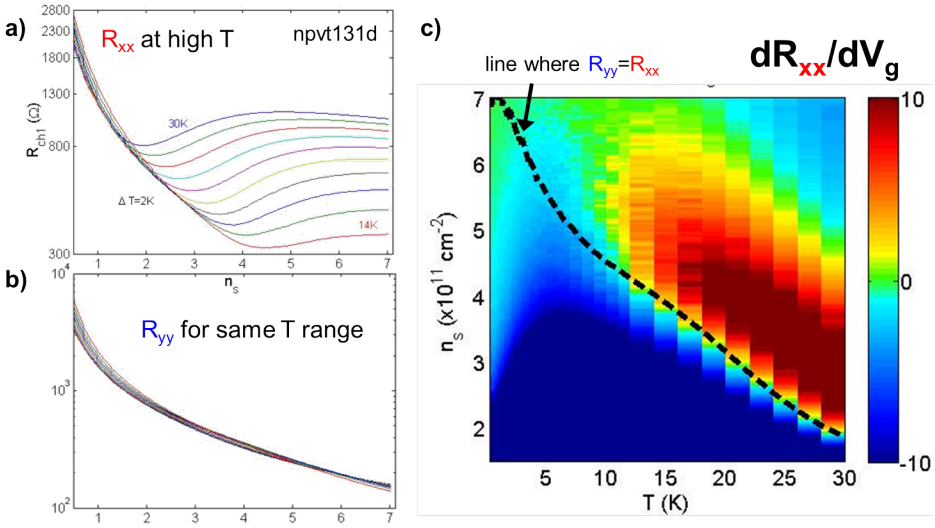

Figure 8.4: High temperature a) R_{xx} and b) R_{yy} vs. carrier density (gate voltage). R_{xx} becomes increasingly non–monotonic at higher T while R_{yy} remains momotonic as expected. Curiously, the R_{yy} curve intersects the R_{xx} curve at the R_{xx} minimum. This is illustrated in c) which shows the derivative of R_{xx} with respect to V_g. The green regions (between cyan and yellow) indicate zero slope (i.e. a local minimum or maximum). The dashed line plots the intersection of R_{xx} and R_{yy}.

8.4 Resistance spikes

At low density and $T \approx 0.3$ K we observe a curious feature at filling factors 1 and 2. As shown in Fig. 8.5 R_{yy} displays a minimum as expected while R_{xx} displays a sharp *peak*. The size of the peak depends on B sweep rate and excitation current, and I-V measurements indicate non-metallic behavior for R_{xx} at this point. Looking at the density dependence of this structure, we find that it appears in a narrow range between 1.4 and 2.2×10^{11} cm^{-2} and is sharpest at $\approx 1.8\times10^{11}$ cm^{-2}. When we revisited the $\nu = 2$ peak months later (when the device mobility had fallen to $\sim 70,000$ cm^2/V s) it did not appear at base temperature ($\approx$ 70mK) but did appear when the sample was heated to $\approx$0.3 K (ν=1 was not visible with the 6 T magnet). This may be due to a level crossing near the Fermi level[56, esp. Fig. 1b][57], an excited state brought about by many body effects, or some mundane fluke of measurement. We will need data from other high-mobility devices in order to form any useful theories here.

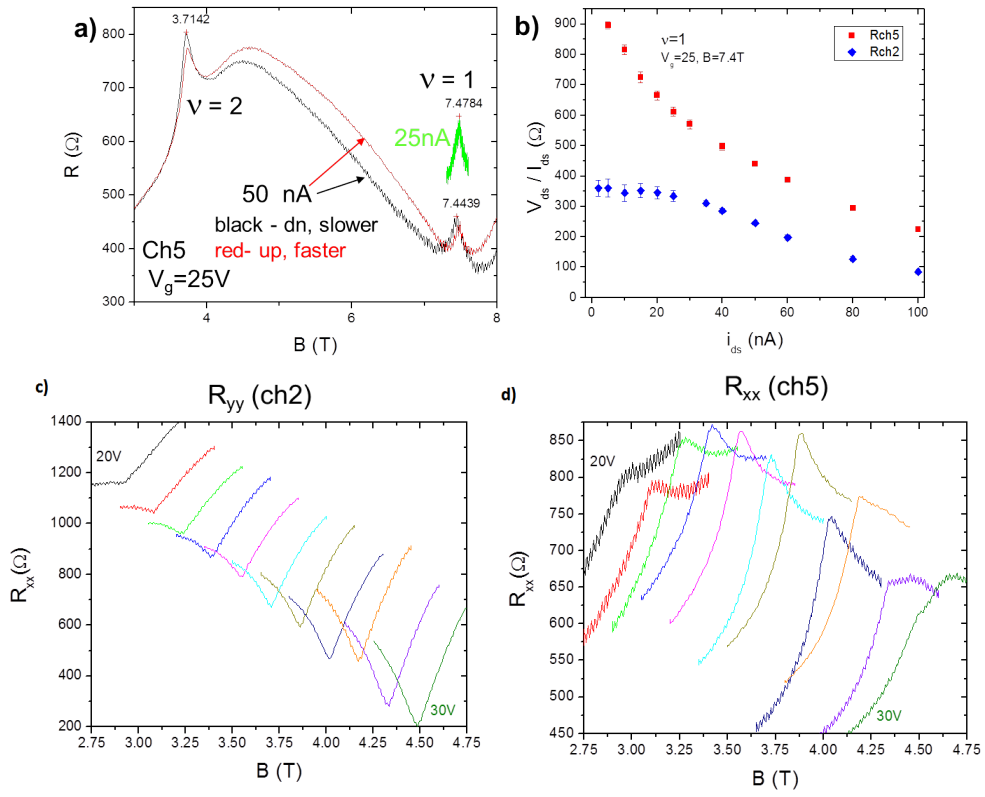

Figure 8.5: a) Anomalous resistance spikes observed at filling factors ν=1 and 2 for low carrier density. b) $I-V$ response at ν=1. R_{yy} (ch2) shows fairly Ohmic behavior at low i_{ds} while R_{xx} (ch5) displays non-Ohmic insulating behavior. c) B sweeps for R_{yy} and d) R_{xx} at ν=2 for a range of gate voltages. R_{yy} displays the expected minimum, which grows deeper as the device mobility increases. However R_{xx} instead exhibits a peak at ν=1 which is strongest in the middle of the plotted density range and eventually becomes a proper minimum at higher n_s.

8.5 Resistance Fluctuations

In npvt56[†] and npvt75 we found reproducible erratic structure in the resistance as a function of gate voltage (Fig. 8.6). Although we typically label these features "fluctuations" they are actually relatively stable with time (∼days to months) and two orders of magnitude larger than the time-dependent fluctuations due to noise. Most interestingly, we note a strong anti-correlation between the fluctuations observed for orthogonal current directions: peaks in R_{xx} frequently match dips in R_{yy} at the same V_g and vice versa. Measurements of the lead resistance revealed noisy behavior that did not correlate to the 4-probe

[†]Data taken in npvt56 was initially ignored as noise. After similar signals in npvt75 proved quite robust we re-examined the older data and noticed the same striking features.

measurements of the 2DEG channel.

As the channel width in these older devices (1—2 mm contact separation and moderate mobility) is four orders of magnitude larger than the mean free path length, an explanation in terms of universal conductance fluctuations[58] seems implausible as the length scales do not justify ballistic transport models. Furthermore, we did not observe such structures in our B–dependent sweeps (though it is possible that the effects of the magnet sweep rate and lock–in timescale simply averaged away fine-scale structure).

Lacking a model for interpreting these observations, we undertook a systematic experimental characterization of this phenomenon, including temperature dependence (features disappeared above 1—2 K and if we cycled to ∼14 K or higher the structure would be different upon return to base T, with only the strongest features persisting), current dependence (features were sharper at lower current), and the response to perpendicular and parallel magnetic fields up to 12 T (regardless of orientation, fields had little to no effect below ∼2 T; at higher B the peaks and dips shifted but remained strong and anti-correlated to 12 T).

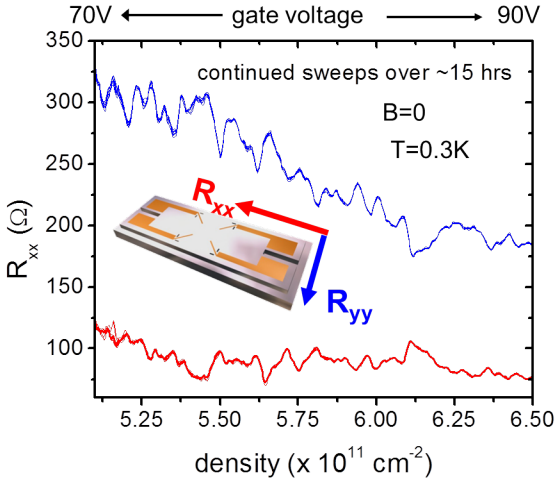

Figure 8.6: Anomalous resistance "fluctuations" as a function of gate voltage for npvt75. While they look like noise they are quite stable over time. Note the anti-correlation between the two channels (peaks matching to dips and vice versa)..

Chapter 9

Closing

9.1 Summary & Lessons

We have developed a novel device architecture for investigating transport on a H-Si(111)-vacuum interface free from the complications created by intrinsic disorder at Si-SiO_2 interfaces. The resulting devices display very high mobilities (up to 110,000 $cm^2/V\,s$ at 70 mK, more than twice as large as the best silicon MOSFETs). This improvement in mobility gives us an enormous increase in resolution for probing the energy structure of our 2DES, since low mobility leads to shorter scattering times and thus a broadening of the energy levels. We have been able to make the first detailed observations of the Integer Quantum Hall Effect (IQHE). From our data we see a consistent picture of low-B valley degeneracy being lifted at high magnetic fields, with gaps eventually appearing at spacings of $\Delta\nu = 1$. In addition, our highest mobility device shows additional gaps at what we believe to be the $\frac{4}{3}$ and $\frac{8}{5}$ fractional Quantum Hall states.

6–Valley Structure

From the data we have collected, we have begun to assemble a model of the multi-valley 2DEG. We find all six valleys populated at B=0 in every device although the valleys are not always degenerate. Our highest mobility device displays distinct signs of sixfold valley degeneracy even though the mobility is 100 times higher (and the level broadening 100 times sharper) than the sixfold-degenerate samples studied by Tsui and Kaminski in [3]. Reference [14] argues that even these "$g_v = 2$" devices in fact contain six occupied valleys, with three degenerate pairs split by an amount large compared with the level broadening yet small enough that all levels remain occupied. By this account, the greater level broadening in the lower-mobility "$g_v = 6$" devices washes out the (possibly reduced) valley splitting so that only the sixfold oscillation period appears.

Our measurements of the intrinsic level width via the Dingle temperature T_D give an

upper bound on the valley splitting of $T_D \approx 0.1$ K. Thus any valley splitting would have to be less than this to be "missed" by the SdH signal. In contrast, a valley splitting that can be resolved in standard Si(111) MOSFETs but not in the old sixfold degenerate MOSFETs would be of order ~ 10 K[14].

In some devices (most notably `npvt75` discussed in this thesis) the sixfold degeneracy is clearly lifted even at $B = 0$, though never so strongly as to completely depopulate any of the valleys. This weak degeneracy lifting has several effects of the 2DES:

unequal occupancy With some valleys raised in energy relative to the others, electrons are no longer distributed symmetrically among the valleys. The low energy valleys contain a larger share of the total density, with the proportion α determined by size of the valley gap Δ relative to the Fermi level.

anisotropy As a result of the unequal valley occupancy, the anisotropy of the effective mass is no longer countered by the symmetry of the valley distribution. This in turn causes the diagonal components of the resistivity to be no longer equal, as it is easier to drive current along the direction of lower effective mass.

SdH frequency If the two systems have significantly different Dingle temperatures, the SdH signal may be dominated by the system with sharper levels. The visible oscillation will be determined by the valley degeneracy of the sharper system and the proportional density in that system.

Valley Transport

The presence of multiple anisotropic conduction channels leads to additional B dependence of the 2DES magnetoresistance and Hall effect. At $B = 0$ this results in a strong suppression of both ρ_{xx} and ρ_{xy} by an amount determined by the in–plane effective masses ($\sim$31% for Si(111)); at higher fields ($(\omega_c\tau)^2 \gg 1$) this correction vanishes.

Interactions between valleys (even those which conserve total 2DES momentum) wash out this effect, causing the transport behavior to approach that of an isotropic single-valley system. Using this fact, we measure changes to the reduced Hall coefficient $r_H \equiv \rho_{x,y}/(B/n_s e)$ in the $B \to 0$ limit as a function of temperature as a new and highly sensitive

probe of valley-valley interactions. We model such interactions as a valley-valley momentum exchange similar to Coulomb drag and find good agreement with our data. Further, the damping rate τ_{vv}^{-1} associated with this drag scales roughly as $(T/T_F)^2$, consistent with expected theoretical behavior for a single-valley interacting Fermi liquid. However, the value of r_H at base temperature (70 mK) is lower than the lower bound predicted by our effective mass model, raising the possibility of more complex scattering and/or interactions.

9.2 Future Directions

9.2.1 Next steps

Mobility improvement

Although our device mobilities far exceed those of Si(111) MOSFETs we continue to optimize the sample design in hopes of further improvements. At minimum, we know that μ ~110,000 cm^2/V s is possible and thus seek to determine why most devices show μ of "only" 20–25,000 cm^2/V s.

MOSFET mobility limits are typically characterized in terms of two major scattering sources: charged impurities and surface roughness. In the case of charge impurities, an increase in the carrier density should result in better screening of these scattering centers, causing μ to *increase* with increasing n_s. On the other hand, an increasing gate voltage brings the 2DES ever closer to the Si surface, strengthening the effects of physical surface disorder. This causes mobility to *decrease* as n_s increases. In combination, these two effects generally result in a peaked μ vs. n_s function with charged impurity scattering dominating the low-n_s positive-slope side and surface roughness dominating the high-n_s negative-slope side[12, 4].

In our H-Si(111) FETs we consistently observe mobility increasing with density and have never observed a mobility peak. This indicates that our mobility mobility is most likely limited by charged impurity scattering on the Si surface. Since the rms roughness of our Si surfaces (as measured by AFM) is of order ~1Å or less, it is not surprising that roughness-limited transport would be difficult to observe. At the same time, we lack the disorder of an amorphous oxide to trap charges near the surface and the substrate doping

is extremely low*, so any charge centers must be directly on the surface itself.

It is likely that the chemical passivation process leaves some ionic residue on the Si surface. We have often found that following H-termination, our Si samples are very conductive at room temperature (∼40 kΩ vs. ∼400 kΩ for samples with a surface oxide) even at zero gate bias. This effect dissipates over the course of a couple days and appears to be quite sensitive to ambient temperature/humidity, vacuum exposure, and the precise details and timing of the chemical treatments. Similar effects have been studied on thin SOI layers [59, 60]. At low temperature ($T \lesssim$30—40 K) this surface conduction freezes out, but it is reasonable to presume that the charges remain as scattering centers.

One method we have considered to improve this is to prepare the Si(111) surface using oxygen-free water rather than NH_4F[61]. We might expect the water to leave less ionic residue. However, preliminary results indicate that although the water method is effective at creating good surfaces and working devices, such devices display the same room temperature conduction and no clear mobility improvement compared with the NH_4F-prepared samples.

Trends across samples

Now that our fabrication yield has greatly improved, it is possible to examine common characteristics across many devices and analyze possible trends. Preliminary observations indicate that devices with strong evidence for sixfold degeneracy in their SdH and QHE structure also display isotropic ρ, while those with signs of broken degeneracy display strong anisotropy in ρ at $B = 0$, consistent with our rough model.

Follow up on leads in present data

It is of great interest to further investigate the signs of fractional quantum hall states observed in `npvt131`. This requires high mobility devices and lower temperatures in large fields. Among other features, one might be able to examine the effects of valley occupancy on composite fermion states, as performed in AlAs[1].

*In the most recent devices, including `npvt131`, the substrate doping $\lesssim 10^{13}$ cm^{-3}, so the boron acceptors are unlikely to be a significant source of such impurities.

9.2.2 Longer term

B implants/holes

In principle, the H-FET device should work just as well if we reverse the charge of all our dopants (e.g. using boron implants for Ohmic contacts on n-type Si(111)) and reverse the gate bias. In this case we would induce holes on the Si(111) surface and create a 2D hole system (2DHS). Since the valence band of Si is isotropic and lacks the sixfold degeneracy of the conduction band the level structure should be much less complicated, leading to easier interpretation if less potential for new and interesting physics. If nothing else, this would help pave the way for broader application of the vacuum FET idea.

Si(100)

Likewise, we should be able to study electrons on Si(100) or other orientations. While chemical passivation of the Si(100) surface is less favorable in terms of surface roughness, even at sub-optimal mobilities we should be able to obtain a functional device or sufficient quality to perform useful magnetotransport measurements and compare the valley structure to that of Si(111). If we wish to pursue H-Si(100) devices further, we can obtain more ordered surfaces by passivating in UHV using a hydrogen cracker. Previous work has demonstrated the fabrication of atomic-scale wires and dots using P donors on H-Si(100) in UHV[62]. If our vacuum encapsulation technique could be applied to such systems it could help bridge the gap between ultra-sensitive quantum-scale devices and the dirty world of macroscopic laboratory electronics.

Appendix A

Derivations in Detail

Most of these calculations are written in terms of 2×2 matrix algebra in order to simplify the derivations. Many were originally computed via brute force with *Mathematica*, which made for awkward sharing. Furthermore, attempts to generalize some derivations would repeatedly cause *Mathematica* to crash, so it became necessary to hand-simplify many terms before feeding them into the computer. In doing this, very compact, analytic hand-derivations of the unequal occupancy result and the valley drag result emerged and are thus presented here.

A.1 Notation and Useful Identities

Note that some of these identities are specific to 2×2 matrices.

Core Matrices

$$\mathbb{I} \equiv \begin{pmatrix} 1 & 0 \\ 0 & 1 \end{pmatrix}, \quad \mathbb{X} \equiv \begin{pmatrix} 0 & 1 \\ 1 & 0 \end{pmatrix}, \quad \mathbb{Z} \equiv \begin{pmatrix} 1 & 0 \\ 0 & -1 \end{pmatrix}$$

$$\mathcal{Z}_\theta \equiv \begin{pmatrix} \mathrm{Cos}[\theta] & -\mathrm{Sin}[\theta] \\ \mathrm{Sin}[\theta] & \mathrm{Cos}[\theta] \end{pmatrix}, \theta_j \equiv \frac{2\pi(j-1)}{q}$$

$$\mathcal{Z}_\theta = \mathrm{Cos}[\theta]\mathbb{I} + \mathrm{Sin}[\theta]\mathbb{X}\mathbb{Z}$$

$$\mathbb{Z}\mathcal{Z}_\theta = \mathcal{Z}_{-\theta}\mathbb{Z}, \qquad \mathbb{X}\mathcal{Z}_\theta = \mathcal{Z}_{-\theta}\mathbb{X}, \qquad \mathbb{Z}\mathbb{X} = -\mathbb{X}\mathbb{Z}$$

$$\mathcal{Z}_\theta + \mathcal{Z}_\phi = 2\mathrm{Cos}\left[\frac{\phi-\theta}{2}\right]\mathcal{Z}_{(\phi+\theta)/2}$$

$$\mathcal{Z}_\theta - \mathcal{Z}_\phi = 2\mathrm{Sin}\left[\frac{\phi-\theta}{2}\right]\mathbb{X}\mathcal{Z}_{(\phi+\theta)/2}\mathbb{Z}$$

Mass

$$M \equiv \begin{pmatrix} m_x & 0 \\ 0 & m_y \end{pmatrix} = \bar{m}\mathbb{I} + m_-\mathbb{Z}$$

$$\bar{m} \equiv (m_x + m_y)/\,2, m_- \equiv (m_x - m_y)/\,2, m^* \equiv \sqrt{m_x m_y}$$

$$\Phi \equiv (\bar{m}/m^*)^2$$

$$M_j \equiv \mathcal{Z}_{\theta_j} M \mathcal{Z}_{-\theta_j} = \bar{m}\mathbb{I} + m_-\mathbb{Z}\mathcal{Z}_{-2\theta_j} = M + 2m_-\mathrm{Sin}\left[\theta_j\right]\mathcal{Z}_{\theta_j}\mathbb{X}$$

$$M_{\mathrm{jk}} \equiv \left({M_j}^{-1} + {M_k}^{-1}\right)^{-1} = \lambda\left(M_j + M_k\right), \qquad \lambda \equiv \frac{m^{*2}}{3\bar{m}^2 + m^{*2}}$$

$$M_j - M_k = 2\mathrm{Sin}\left[\frac{\theta_k - \theta_j}{2}\right]\mathcal{Z}_{-(\theta_k+\theta_j)/2}$$

$$\sum_{j=1}^{q} M_j = q\bar{m}\mathbb{I}, \qquad \sum_{j=1}^{q} {M_j}^{-1} = q\frac{\bar{m}}{m^{*2}}\mathbb{I}$$

Commutators

$$[M_j, \mathbb{X}] = 2m_-\mathrm{Cos}\left[2\theta_j\right]\mathbb{Z}\mathbb{X}$$

$$M_j\mathbb{X} = m^{*2}\mathbb{X}{M_{-j}}^{-1} \quad M_j\mathbb{Z} = \mathbb{Z}M_{-j}$$

$$[M_j, \mathbb{Z}] = -2m_-\mathrm{Sin}\left[2\theta_j\right]\mathbb{Z}\mathbb{X}, \quad [M_j, \mathcal{Z}_\phi] = \mathrm{Sin}[\phi]$$

$$[M_j, \mathbb{X}\mathbb{Z}] = -2m_-\mathrm{Sin}[\phi]\mathcal{Z}_{2\theta_j}\mathbb{X}, \quad [M_j, \mathbb{Z}.\mathbb{X}] = 2m_-\mathbb{X}.\mathcal{Z}_{-2\theta_j}$$

Determinants & Inverses

$$\mathrm{Det}[A + B] = \mathrm{Det}[A] + \mathrm{Det}[B] + \mathrm{Tr}[A]\mathrm{Tr}[B] - \mathrm{Tr}[\mathrm{AB}]$$

$$\mathrm{Det}[A + B + C] = \mathrm{Det}[A] + \mathrm{Det}[B] + \mathrm{Det}[C] + (\mathrm{Tr}[A]\mathrm{Tr}[B] + \mathrm{Tr}[B]\mathrm{Tr}[C]$$

$$+\mathrm{Tr}[C]\mathrm{Tr}[A]) - (\mathrm{Tr}[\mathrm{AB}] + \mathrm{Tr}[\mathrm{BC}] + \mathrm{Tr}[\mathrm{CA}])$$

$$2\mathrm{Det}[A] = \mathrm{Tr}[A]^2 - \mathrm{Tr}\left[A^2\right]$$

$$\mathrm{Det}[AB] = \mathrm{Det}[A]\mathrm{Det}[B]$$

$$(A+B)^{-1} = \frac{1}{\mathrm{Det}[A+B]}\left(\mathrm{Det}[A]A^{-1} + \mathrm{Det}[B]B^{-1}\right)$$

$$(A+B+C)^{-1} = \frac{1}{\mathrm{Det}[A+B+C]}\left(\mathrm{Det}[A]A^{-1} + \mathrm{Det}[B]B^{-1} + \mathrm{Det}[C]C^{-1}\right)$$

If $\mathrm{Det}[A] = \mathrm{Det}[B]$:

$$\Rightarrow \left(A^{-1}+B^{-1}\right)^{-1} = \mathrm{Det}[A](A+B)/\mathrm{Det}[A+B]$$

$$\left[A^{-1}, B\right] = A^{-1}[A,B]A^{-1}$$

$$(a\mathbb{I} + b\mathbb{Z}\mathbb{X})^{-1} = \frac{1}{a^2+b^2}(a\mathbb{I} - b\mathbb{Z}\mathbb{X})$$

$$\mathrm{Det}\left[M_j\right] = m^{*2} \qquad \mathrm{Tr}\left[M_j\right] = 2\bar{m}$$

$$M^{-1} = \frac{1}{m^{*2}}\mathbb{X}M\mathbb{X} \qquad M_j^{-1} = \frac{1}{m^{*2}}\left(M_j - 2m_{-}\mathcal{Z}_{2\theta_j}\mathbb{Z}\right)$$

$${M_j}^{-1} = \frac{1}{m^{*2}}\left(2\bar{m}\mathbb{I} - M_j\right)$$

$$\mathrm{Det}\left[{M_j}^{-1}\right] = 1/m^{*2} \qquad \mathrm{Tr}\left[{M_j}^{-1}\right] = 2/m_{\mathrm{op}} = 2\bar{m}/m^{*2}$$

$$\mathrm{Det}\left[M_{\mathrm{jk}}\right] = \lambda^2\mathrm{Det}\left[M_j + M_k\right] = m^{*4}/\left(3\bar{m}^2 + m^{*2}\right)$$

$$\lambda = \mathrm{Det}\left[M_j\right]/\mathrm{Det}\left[M_j + M_k\right]$$

A.2 Unequal Valley Occupancy

$$\vec{J_j} \times \vec{B} = B\mathbb{Z}\mathbb{X}\vec{J_j}, \quad \left(\sum_{k=1}^{q} M_k\right) = q\bar{m}\mathbb{I}, \quad \left(\sum_{k=1}^{q} {M_k}^{-1}\right) = q\frac{\bar{m}}{m^2}\mathbb{I}$$

q ≡ the number of valleys or valley pairs (for Si(111) q=3)

This frame indicates side calculations or identities.

Shadow box indicates a key definition or result.

Derivation

We now start with the kinetic equation without drag:

$$\begin{aligned}
M_j\vec{J}_j =& n_j e^2\tau\vec{E} + e\tau\vec{J}_j\times\vec{B} \\
\vec{J}_j =& n_j e^2\tau {M_j}^{-1}\vec{E} + e\tau {M_j}^{-1}\vec{J}_j\times\vec{B} && \text{(multiply by } M_j^{-1}\text{)} \\
\sum_{j=1}^{q} J_j =& e^2\tau\sum_{j=1}^{q} n_j {M_j}^{-1}\vec{E} + e\tau\sum_{j=1}^{q} {M_j}^{-1}\vec{J}_j\times\vec{B} && \text{(sum over valleys)} \\
\vec{J}_{\text{Tot}} =& e^2\tau\sum_{j=1}^{q} n_j {M_j}^{-1}\vec{E} + Be\tau\sum_{j=1}^{q} {M_j}^{-1}\mathbb{ZX}\vec{J}_j && \left(\textstyle\sum_{j=1}^{q} J_j = \vec{J}_{\text{Tot}}\right) \\
=& e^2\tau\sum_{j=1}^{q} n_j {M_j}^{-1}\vec{E} + \frac{Be\tau}{m^2}\mathbb{ZX}\sum_{j=1}^{q} M_j\ \vec{J}_j
\end{aligned}$$

To handle the last term note that

$$M_j J_j = n_j e^2\tau\vec{E} + Be\tau\mathbb{ZX}J_j \tag{A.1}$$

$$\sum_{j=1}^{q} M_j J_j = m\sigma_0\vec{E} + m\omega\tau\mathbb{ZX}J_{\text{Tot}}. \tag{A.2}$$

This gives us

$$\begin{aligned}
\vec{J}_{\text{Tot}} =& e^2\tau\sum_{j=1}^{q} n_j {M_j}^{-1}\vec{E} + \frac{Be\tau}{m^2}\mathbb{ZX}\left(ne^2\tau\vec{E} + Be\tau\mathbb{ZX}J_{\text{Tot}}\right) \\
=& e^2\tau\left(\sum_{j=1}^{q} n_j {M_j}^{-1} + n\frac{\omega\tau}{m}\mathbb{ZX}\right)\vec{E} - \omega\tau^2\mathbb{I}\vec{J}_{\text{Tot}}
\end{aligned}$$

$$e^2\tau\left(\sum_{j=1}^{q} n_j {M_j}^{-1} + n\frac{\omega\tau}{m}\mathbb{ZX}\right)\vec{E} = \left(1+\omega\tau^2\right)\mathbb{I}\vec{J}_{\text{Tot}} \tag{A.3}$$

Let $n_j = \alpha_j n$ ($\Sigma\alpha_j = 1$)

$$\left(\sum_{j=1}^{q}\alpha_j m {M_j}^{-1}+\omega\tau\mathbb{ZX}\right)\vec{E}=\frac{m}{ne^2\tau}\left(1+\omega\tau^2\right)\mathbb{I}\vec{J}_{\text{Tot}}$$

$$\vec{E}=\frac{m^*}{ne^2\tau}\left(1+\omega\tau^2\right)\left(m^*\sum_{j=1}^{q}\alpha_j {M_j}^{-1}+\omega\tau\mathbb{ZX}\right)^{-1}\vec{J}_{\text{Tot}}$$

To find the inverse we first compute:

$$\text{Det}\left[m^*\textstyle\sum_{j=1}^{q}\alpha_j {M_j}^{-1}\right]=\frac{M_{\alpha1}M_{\alpha2}}{m^{*2}}\quad \text{Det}\left[\alpha_j {M_j}^{-1}\right]=\left(\frac{\alpha_j}{m^*}\right)^2$$

where we have defined

$$\boxed{M_{\alpha1}\equiv\left(\textstyle\sum_{j=1}^{q}\alpha_j M_j\right)_{xx}\qquad M_{\alpha2}\equiv\left(\textstyle\sum_{j=1}^{q}\alpha_j M_j\right)_{yy}}.$$

Thus

$$\left(m^*\textstyle\sum_{j=1}^{q}\alpha_j {M_j}^{-1}\right)^{-1}=\frac{m^{*2}}{M_{\alpha1}M_{\alpha2}}\left(\textstyle\sum_{j=1}^{q}\frac{\alpha_j}{m^{*2}}M_j\right)=\frac{1}{M_{\alpha1}M_{\alpha2}}\left(\textstyle\sum_{j=1}^{q}\alpha_j M_j\right)$$

$$\vec{E}=\frac{m^*}{ne^2\tau}\frac{\left(1+\omega\tau^2\right)}{M_{\alpha1}M_{\alpha2}/m^{*2}+\omega\tau^2}\left(\frac{1}{m^{*2}}\sum_{j=1}^{q}\alpha_j M_j-\omega\tau\mathbb{ZX}\right)\vec{J}_{\text{Tot}}\tag{A.4}$$

So

$$\boxed{\rho=\frac{m^*}{ne^2\tau}\frac{\left(1+\omega\tau^2\right)}{M_{\alpha1}M_{\alpha2}/m^{*2}+\omega\tau^2}\left(\frac{1}{m^{*2}}\sum_{j=1}^{q}\alpha_j M_j-\omega\tau\mathbb{ZX}\right)}\tag{A.5}$$

A.2.1 Special Cases

- If all valleys are equally occupied ($\alpha_j = 1/q$) we recover the original solution:

$$\sum_{j=1}^{q}\alpha_j M_j=q\sum_{j=1}^{q}M_j=\bar{m}\mathbb{I}.\tag{A.6}$$

- If two valley pairs have equal occupancy (let $\alpha_k \equiv \alpha$, $\alpha_{j\neq k} = (1-\alpha)/(q-1)$):

$$\sum_{j=1}^{q}\alpha_j M_j=\frac{q}{q-1}\left((1-\alpha)\bar{m}\mathbb{I}+\left(\alpha-\frac{1}{q}\right)M_k\right).\tag{A.7}$$

- If $\{\alpha_j\} = \{a, b, 1-a-b\}$ then:

$$\sum_{j=1}^{q} \alpha_j M_j = \begin{pmatrix} \bar{m} + \frac{1}{2}(3a-1)m_- & -\frac{1}{2}\sqrt{3}(a+2b-1)m_- \\ -\frac{1}{2}\sqrt{3}(a+2b-1)m_- & \frac{1}{2}\left(2\bar{m} + (1-3a)m_-\right) \end{pmatrix} \tag{A.8}$$

A.3 Intervalley Drag

$$\vec{J}_j \times \vec{B} = B\mathbb{ZX}\vec{J}_j, \quad \left(\sum_{k=1}^{q} M_k\right) = q\bar{m}\mathbb{I}, \quad \left(\sum_{k=1}^{q} {M_k}^{-1}\right) = q\frac{\bar{m}}{m^2}\mathbb{I}$$

q ≡ the number of valleys or valley pairs (for us q=3)

This frame indicates side calculations or identities.

Shadow box indicates a key definition or result.

Derivation

We now start with the kinetic equation Eq. (7.4) given earlier:

$$\begin{aligned}
M_j\vec{J}_j =& n_j e^2\tau\vec{E} + e\tau\vec{J}_j \times \vec{B} + \gamma\lambda\sum_{k=1}^{q}(M_j + M_k)\left(\vec{J}_k - \vec{J}_j\right) \\
\vec{J}_j =& n_j e^2\tau {M_j}^{-1}\vec{E} + e\tau {M_j}^{-1}\vec{J}_j \times \vec{B} + \gamma\lambda {M_j}^{-1}\sum_{k=1}^{q}(M_j + M_k)\left(\vec{J}_k - \vec{J}_j\right) \\
\sum_{j=1}^{q} J_j =& e^2\tau\sum_{j=1}^{q} n_j {M_j}^{-1}\vec{E} + e\tau\sum_{j=1}^{q} {M_j}^{-1}\vec{J}_j \times \vec{B} \\
&+ \gamma\lambda\left(\left(\sum_{j=1}^{q} {M_j}^{-1}\right)\sum_{k=1}^{q} M_k\vec{J}_k - \sum_{j=1}^{q} {M_j}^{-1}\left(\sum_{k=1}^{q} M_k\right)\vec{J}_j\right) \\
\vec{J}_{\text{Tot}} =& e^2\tau\sum_{j=1}^{q} n_j {M_j}^{-1}\vec{E} + \frac{Be\tau}{m^2}\mathbb{ZX}\sum_{j=1}^{q} M_j\vec{J}_j + 2q\gamma\lambda\frac{\bar{m}}{m^2}\sum_{j=1}^{q} M_j\ \vec{J}_j - 2q\gamma\lambda\frac{\bar{m}^2}{m^2}\vec{J}_{\text{Tot}}
\end{aligned}$$

To simplify this expression we make a few substitutions.

Let $n_j = 1/q$, $\quad \Phi \equiv \frac{\bar{m}^2}{m^2}$, $\quad \sqrt{\Phi} = \frac{\bar{m}}{m}$, $\quad \mathrm{Q} \equiv 2\mathrm{q}\ \gamma\ \lambda$, $\quad \sigma_0 \equiv \frac{ne^2\tau}{m}$, $\quad \omega = \frac{eB}{m}$

This gives us

$$\begin{aligned}\vec{J}_{\text{Tot}} &= \sigma_0\sqrt{\Phi}\vec{E} + \omega\tau\mathbb{ZX}\frac{1}{m}\sum_{j=1}^{q} M_j\ \vec{J}_j + Q\sqrt{\Phi}\frac{1}{m}\sum_{j=1}^{q} M_j\ \vec{J}_j - Q\Phi\vec{J}_{\text{Tot}} \\ (1+Q\Phi)\vec{J}_{\text{Tot}} &= \sigma_0\sqrt{\Phi}\vec{E} + \left(\omega\tau\mathbb{ZX} + Q\sqrt{\Phi}\mathbb{I}\right)\frac{1}{m}\sum_{j=1}^{q} M_j\vec{J}_j\end{aligned}$$

To handle the last term note that

$$M_jJ_j = n_je^2\tau\vec{E} + Be\tau\mathbb{ZX}J_j + \gamma\lambda\sum_{k=1}^{q}(M_j+M_k)\left(\vec{J}_k - \vec{J}_j\right) \qquad \text{(Eq. (7.4))}$$

$$\sum_{j=1}^{q} M_jJ_j = m\sigma_0\vec{E} + m\omega\tau\mathbb{ZX}J_{\text{Tot}}. \qquad \text{(A.9)}$$

so

$$\begin{aligned}(1+Q\Phi)\vec{J}_{\text{Tot}} &= \sigma_0\sqrt{\Phi}\vec{E} + \left(\omega\tau\mathbb{ZX} + Q\sqrt{\Phi}\mathbb{I}\right)\left(\sigma_0\vec{E} + \omega\tau\mathbb{ZX}\vec{J}_{\text{Tot}}\right) \\ &= \sigma_0\left(\sqrt{\Phi}(1+Q)\mathbb{I} + \omega\tau\mathbb{ZX}\right)\vec{E} - \left(\omega^2\tau^2\mathbb{I} - Q\sqrt{\Phi}\omega\tau\mathbb{ZX}\right)\vec{J}_{\text{Tot}} \\ \left(\left(1+Q\Phi+\omega^2\tau^2\right)\mathbb{I} - Q\sqrt{\Phi}\omega\tau\mathbb{ZX}\right)\vec{J}_{\text{Tot}} &= \sigma_0\left(\sqrt{\Phi}(1+Q)\mathbb{I} + \omega\tau\mathbb{ZX}\right)\vec{E}.\end{aligned}$$

We now rearrange this into the form $\vec{E} = \rho\vec{J}_{\text{Tot}}$.

$$\begin{aligned}\vec{E} = &\quad \tfrac{1}{\sigma_0}\left(\sqrt{\Phi}(1+Q)\mathbb{I} + \omega\tau\mathbb{ZX}\right)^{-1}\left(\left(1+Q\Phi+\omega^2\tau^2\right)\mathbb{I} - Q\sqrt{\Phi}\omega\tau\mathbb{ZX}\right)\vec{J}_{\text{Tot}} \\ = &\quad \tfrac{1/\sigma_0}{\Phi(1+Q)^2+\omega^2\tau^2}\left(\sqrt{\Phi}(1+Q)\mathbb{I} - \omega\tau\mathbb{ZX}\right)\left(\left(1+Q\Phi+\omega^2\tau^2\right)\mathbb{I} - Q\sqrt{\Phi}\omega\tau\mathbb{ZX}\right)\vec{J}_{\text{Tot}}\end{aligned}$$

$$\text{Let } \rho_0 \equiv \frac{1}{\sigma_0}\frac{1}{(1+Q)^2+\omega^2\tau^2}$$

$$\begin{aligned}\rho =& \rho_0\left(\sqrt{\Phi}(1+Q)\mathbb{I} - \omega\tau\mathbb{ZX}\right)\left(\left(1+Q\Phi+\omega^2\tau^2\right)\mathbb{I} - Q\sqrt{\Phi}\omega\tau\mathbb{ZX}\right) \\ =& \rho_0\left(\sqrt{\Phi}(1+Q)\left(1+Q\Phi+\omega^2\tau^2\right)\mathbb{I} - \Phi Q(1+Q)\omega\tau\mathbb{ZX}\right. \\ &\left. - \left(1+Q\Phi+\omega^2\tau^2\right)\omega\tau\mathbb{ZX} - Q\sqrt{\Phi}\omega^2\tau^2\mathbb{I}\right) \\ =& \rho_0\sqrt{\Phi}\left((1+Q)(1+Q\Phi)+\omega^2\tau^2\right)\mathbb{I} - \rho_0\omega\tau\left(Q^2\Phi+2Q\Phi+1+\omega^2\tau^2\right)\mathbb{ZX}\end{aligned}$$

$$\boxed{\rho = \frac{\bar{m}}{ne^2\tau_0}\frac{(1+Q)(1+Q\Phi)+\omega^2\tau^2}{\Phi(1+Q)^2+\omega^2\tau^2}\mathbb{I} - \frac{B}{ne}\frac{Q^2\Phi+2Q\Phi+1+\omega^2\tau^2}{\Phi(1+Q)^2+\omega^2\tau^2}\mathbb{ZX}} \tag{A.10}$$

To match the notation used in Chapter 7 Eqs. (7.5) and (7.6) we simply substitute $Q \to \gamma\Lambda$.

$$\boxed{\rho = \frac{\bar{m}}{ne^2\tau}\frac{(1+\gamma\Lambda)(1+\gamma\Lambda\Phi)+\omega^2\tau^2}{\Phi(1+\gamma\Lambda)^2+\omega^2\tau^2}\mathbb{I} - \frac{B}{ne}\frac{\gamma\Lambda^2\Phi+2\gamma\Lambda\Phi+1+\omega^2\tau^2}{\Phi(1+\gamma\Lambda)^2+\omega^2\tau^2}\mathbb{ZX}} \tag{A.11}$$

Valley Splitting

Mass tensors

Valley splitting due to wafer miscut and in-plane B field both boil down to tracking effective masses for each valley. We start with the effective mass tensor in the [100] basis:

$$\mathbf{M} = \begin{pmatrix} m_x & 0 & 0 \\ 0 & m_y & 0 \\ 0 & 0 & m_z \end{pmatrix}. \tag{A.12}$$

Each valley pair will result in a different assignment of m_ℓ=0.916 and m_t=0.190 (twice) to m_x, m_y, m_z. In *Mathematica* we can define a set of replacement rules to carry out this assignment once we obtain an expression of interest.

$$\mathsf{ValleyRulesN} = \mathsf{Map}\left[\mathsf{Thread}\left[\{m_x, m_y, m_z\} \to \#\right]\&, \mathsf{Permutations}[\{.916, .19, .19\}]\right] \Rightarrow$$

$$\{\{m_x \to 0.916, m_y \to 0.19, m_z \to 0.19\}, \quad \{m_x \to 0.19, m_y \to 0.916, m_z \to 0.19\},$$

$$\{m_x \to 0.19, m_y \to 0.19, m_z \to 0.916\}\}$$

In this basis the inverse mass tensor is trivial to compute.

$$\mathbf{W} = \begin{pmatrix} 1/m_x & 0 & 0 \\ 0 & 1/m_y & 0 \\ 0 & 0 & 1/m_z \end{pmatrix} \tag{A.13}$$

To move to the [111] orientation we make two rotations (one about $\hat{z}$ and one about $\hat{x}$)

$$\begin{aligned}\mathbf{M}_{111} =& \mathcal{X}(-\Xi)\mathcal{Z}(-\pi/4)\mathbf{M}\mathcal{Z}(\pi/4)\mathcal{X}(\Xi) && \text{(Eq. (2.2))}\\ =& \begin{pmatrix} \frac{1}{2}(m_x+m_y) & \frac{m_x-m_y}{2\sqrt{3}} & \frac{m_x-m_y}{\sqrt{6}} \\ \frac{m_x-m_y}{2\sqrt{3}} & \frac{1}{6}(m_x+m_y+4m_z) & \frac{m_x+m_y-2m_z}{3\sqrt{2}} \\ \frac{m_x-m_y}{\sqrt{6}} & \frac{m_x+m_y-2m_z}{3\sqrt{2}} & \frac{1}{3}(m_x+m_y+m_z) \end{pmatrix} && \text{(A.14)}\end{aligned}$$

where $\Xi = \arccos 1/\sqrt{3}$. Likewise we can obtain the inverse tensor $\mathbf{W}_{111} = \mathbf{M}_{111}^{-1}$.

A.4 Miscut

Now we consider the case in which the wafer is miscut by an angle ψ away from [111]. We define the direction of the miscut by a second angle φ defined so that $\varphi = 0$ indicates a miscut toward $[11\bar{2}]$ (or clockwise about the $[1\bar{1}0]$ axis). The total rotation (acting on a vector) is then

$$\mathrm{R2}[\varphi,\psi] := \mathcal{Z}[\varphi]\cdot\mathcal{X}[\psi]\cdot\mathcal{Z}[-\varphi]. \tag{A.15}$$

To transform tensors we define the function

$$\mathsf{Miscut}[\mathit{tensor},\varphi,\psi] := \mathrm{R2}[\varphi,\psi]\cdot\mathit{tensor}\cdot\mathrm{R2}[\varphi,-\psi] \tag{A.16}$$

which we use to get the miscut tensors

$$\mathbf{Mt}[\varphi,\psi] = \mathsf{Miscut}[\mathbf{M}_{111},\varphi,\psi] \tag{A.17}$$

$$\mathbf{Wt}[\varphi,\psi] = \mathsf{Miscut}[\mathbf{W}_{111},\varphi,\psi]. \tag{A.18}$$

We can get a preview of the effect of a small miscut on the normal mass:

$$\begin{aligned}&\mathsf{Series}\,[1/\mathbf{Wt}_{zz}[0,\psi]/.\,\mathrm{ValleyRulesN},\{\psi,0,1\}]\Rightarrow\\&\big\{0.2582-0.1311\psi+O[\psi]^2,\\&\quad 0.2582-0.1311\psi+O[\psi]^2,\\&\quad 0.2582+0.2622\psi+O[\psi]^2\big\}\end{aligned}\tag{A.19}$$

Effect on energy

The ground state energy for a triangular potential (ignoring image, exchange, and self-consistent terms) is (AF& S[12] Eq. 3.23):

$$E_0^z \approx \left(\frac{\hbar^2}{2m_z}\right)^{1/3}\left(\frac{3\pi eF}{2\epsilon_0\kappa}\left(0+\frac{3}{4}\right)\right)^{2/3}\tag{A.20}$$

where

$$F=\frac{e(n_d+fn_s)}{\epsilon_0\kappa}\tag{A.21}$$

N_d is the depletion layer charge (for us, N_d <0.1×10^{11} cm^{-2} is probably an overestimate), κ is the dielectric constant of Si (≈11.5), and $0\le f\le 1$ is an adjustable parameter based on where (relative to the interface) we sample the effective field. In the limit $n_d \ll n_s$ we find that a value of f ≈0.8 gives a ground state energy that agrees with the one obtained via the variational approach outlined in [12, p. 466], including the image charge, depletion, and self-consistent contributions (but excluding the exchange term). For the ideal Si(111) mass m_z =0.258 and n_s=7×10^{11} cm^{-2}

$$E_0^z \approx 620\mathrm{K}\tag{A.22}$$

Although this value appears quite large compared with other energy scales in our system (E_F ∼10 K, k_BT ≪1 K), this value by itself is meaningless since we can always define the zero point of our energy scale so that the ground state energy is zero. What is important here is the relative energy between various states. To see the effect of the miscut on the ground state energy we simply evaluate Eq. (A.20) using $m_z = 1/\mathbf{Wt}_{zz}[\varphi,\psi]$ for

each valley configuration.

$$\mathsf{Ez0N}[\phi,\psi] = E_0^z /. \left(m_z \to 1/\mathbf{Wt}_{33}[\phi,\psi]^{1/3}\right) /. \mathrm{ValleyRulesN} \tag{A.23}$$

Figure A.1 plots the effect of a 1 degree miscut, which quite large. Generally 0.5 degrees is on the high end for our wafers (though npvt56 had a miscut ∼0.6 degrees); typical values are closer to 0.2 (npvt75) to less than 0.1 (npvt131).

Because the miscut ψ is so small, it makes sense to use a series expansion to simplify our expressions for the energy gaps. We can see from Fig. A.1 that the lowest energy gap is maximum at $\varphi = 0$, so we will take the value at that point.

$$\mathsf{Series}\,[\mathsf{Ez0N}[0,\psi][[2]] - \mathrm{Ez0N}[0,\psi][[3]], \{\psi, 0, 1\}]$$

$$314.415\psi + O[\psi]^2 \quad \Rightarrow \quad 5.5\,\mathrm{K/degree}$$

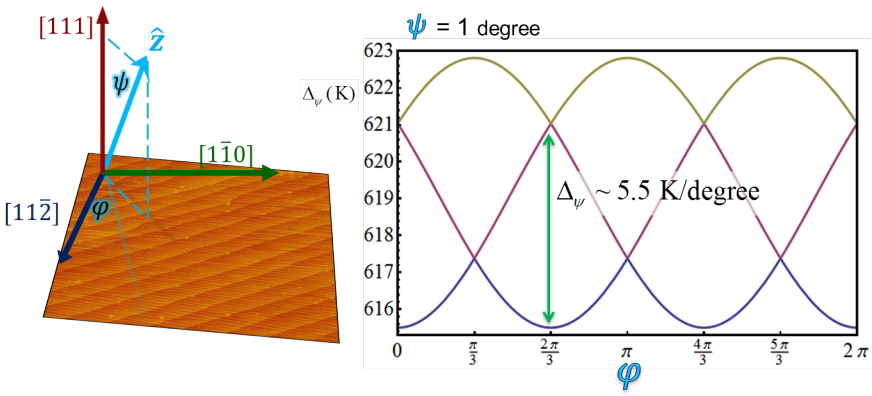

Figure A.1: Valley energies due to a miscut ψ =1 degree, as a function of the miscut direction φ. The gap between the lowest energy level (green) and first excited level (purple) varies with φ and vanishes at $\varphi = \frac{(1+2n)\pi}{3}$, creating a 4-fold degenerate ground state at these points. n_s=7×10^{11} cm^{-2}.

A.5 In-Plane B Field

For a magnetic field B of arbitrary orientation Stern and Howard[18] show that in addition to the cyclotron energy there is an additional B-dependent energy term (Eq. A8):

$$\Delta E_B = \frac{e^2}{2}(\langle z^2\rangle - \langle z\rangle^2)\left(\frac{(B_y - \frac{\mathbf{W}_{23}}{\mathbf{W}_{33}}B_z)^2}{m_1} + \frac{B_x^2}{m_2}\right). \qquad \text{(Eq. 2.14)}$$

We will make use of the inverse mass tensor $\mathbf{W}$ from the previous section; the masses m_1 and m_2 work out to the usual in–plane masses m_x and m_y. To find the prefactor $(\frac{e^2}{2}\langle z^2\rangle - \langle z\rangle^2)$ we use the variational approach in [12]

$$\left(\langle z^2\rangle - \langle z\rangle^2\right) = \frac{3}{b^2} \tag{A.24}$$

$$b^3 = \frac{12 m_z e^2 N^*}{\epsilon_0 \kappa \hbar^2} \tag{A.25}$$

$$N^* = n_d + \frac{11}{32} n_s \tag{A.26}$$

The derivation of Eq. (2.14) in [18] relies on the freedom to choose an x-y basis aligned with the (in-plane) valley ellipses to enable various terms to cancel. Therefore we must set our coordinates separately for each valley and translate the B field into each coordinate system. This gives us a set of three transformation rules:

$$\mathsf{Av} = \{B_x \to B\mathrm{Sin}[\theta]\mathrm{Cos}[\phi],$$
$$B_y \to B\mathrm{Sin}[\theta]\mathrm{Sin}[\phi], B_p \to B\mathrm{Cos}[\theta]\}\,;$$
$$\mathsf{Bv} = \left\{B_x \to -\frac{1}{2}B\mathrm{Cos}[\phi]\mathrm{Sin}[\theta] + \frac{1}{2}\sqrt{3}B\mathrm{Sin}[\theta]\mathrm{Sin}[\phi],\right.$$
$$\left.B_y \to -\frac{1}{2}\sqrt{3}B\mathrm{Cos}[\phi]\mathrm{Sin}[\theta] - \frac{1}{2}B\mathrm{Sin}[\theta]\mathrm{Sin}[\phi], B_p \to B\mathrm{Cos}[\theta]\right\};$$
$$\mathsf{Cv} = \left\{B_x \to -\frac{1}{2}B\mathrm{Cos}[\phi]\mathrm{Sin}[\theta] - \frac{1}{2}\sqrt{3}B\mathrm{Sin}[\theta]\mathrm{Sin}[\phi],\right.$$
$$\left.B_y \to \frac{1}{2}\sqrt{3}B\mathrm{Cos}[\phi]\mathrm{Sin}[\theta] - \frac{1}{2}B\mathrm{Sin}[\theta]\mathrm{Sin}[\phi], B_p \to B\mathrm{Cos}[\theta]\right\};$$

We also create a function that takes and expression and returns a three–item list containing the expression mapped into each valley.

$$\mathsf{Vlist}[x\_] := x/.\,Av, x/.\,Bv, x/.\quad Cv; \tag{A.27}$$

For example, for n_s=7×10^{11} cm^{-2} in a 10 T field tilted by 5 degrees towards [1$\bar{1}$0]

$$\begin{aligned}\mathsf{Vlist}[\Delta E_B]/.\{n_s \to 7, B \to 12, \phi \to 0, \theta \to \pi/36\}\\ \Rightarrow \{1.4481,\quad 1.89963,\quad 1.04249\}K\end{aligned} \tag{A.28}$$

Appendix B

Fabrication of Hydrogen-terminated Si(111) FETs

Adapted from material largely compiled by Kevin Eng and Tomasz Kott, July 2007

Fabrication of the device begins with two individual Si substrates (∼1 cm^2), each having a distinct function. One is the H–terminated Si(111) substrate with source and drain contacts. It is at this surface that the 2DES will be created. The other is a silicon–on–insulator (SOI) substrate which acts as the remote gate, where an electric field can be controlled within an etched cavity (Fig. B.1). These two substrates are contact-bonded in vacuum, and they adhere to one another due to local van der Waals forces between the two mating surfaces. Successful bonding requires these surfaces to be *flat* and *clean* of particle contamination before contact.

This manuscript describes in detail the processing steps used to fabricate H–Si(111) FETs and some of the experience and knowledge compiled throughout the years during development.

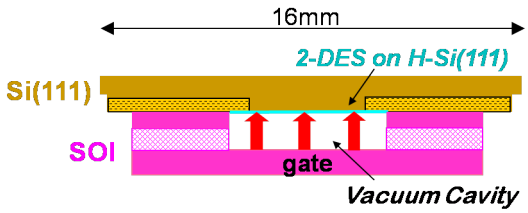

Figure B.1: H–Si(111) bonded to the SOI

B.1 Si-111 Sample Processing

Material for the Si(111) is p–type float-zone (FZ) silicon. Prior to early 2008 (device numbers ≤115) wafer resistivity was typically either 2" 1–20 Ω–cm or 3" 100–200 Ω–cm. Beginning in January 2008, we switched to 3" wafers with high resistivity ($\rho > 10,000$ Ω–cm).

B.1.1 Oxidation

Prior to lithography, we first grow a sacrificial thermal oxide on the surface. Oxidation can be performed in-house or by a third party, depending on the wafer size. The in-house tube furnace can accommodate wafers with diameters ≤3" or that have been pre-trimmed to this size using the dicing saw (see §C.4).

Oxidation of wafers with diameters >3" is outsourced and has been done at both MEMs Exchange and NIST at Gaithersburg (*See C.5 for contact info*). Typically the target thickness for this oxide is ∼30 nm and has varied ±5 nm from the different sources. The wafers should go through an RCA cleaning and HF dip right before the oxidation.

Procedures for growing an oxide in the LPS tube oven

1. Ultrasonicate in IPA for 10 minutes.
2. RCA clean wafer for 15 minutes.
3. 20:1 HF Dip for 5 sec.
4. move wafer from the cleanroom to the tube furnace in a closed carrier
5. In the furnace logbook write the date, your initials, material, and the temperature, duration, and gas used for your run.
   (also check previous entries and note whether metals have been used in the furnace recently)
6. Place in tube oven and oxidize wafer at 950°C for 30 minutes in O_2. Ramp up oven to 650°C and hold for 5 minutes then ramp up (40°C/min) to 950°C for 30 minutes.

   For Si (111) substrates, ∼320 Å of SiO_2 will be grown.

B.1.2 Lithography

There are two sets of masks for most Si(111) samples: the first mask is for defining a mesa by etching around the edges of the die in order to prevent particulate from residing on the top surface. The second mask creates windows for ion-implantion of source-drain contacts.

First Lithography step: Mesa

This step will create a $\sim$2 μm high mesa inset from the edges of the die.

1. Rinse wafer with IPA.
2. Blow dry and set on 120°C hotplate for 1–2 minutes.
3. Apply standard positive resist lithography (906–10) and use MESA mask.
4. RIE Mesa:
   (a) `llscum`: 30 seconds.
   (b) `sio2pt`: 1 min 15 sec. (remove top oxide grown, *See Appendix for etch rates*)
   (c) `engsix55`: 12 min
   (d) `o2chambr`: 15 min (after sample is removed from the RIE chamber)
5. Remove the resist using acetone, methanol and IPA.

Here, it is useful to have one acetone bath that strips off the majority of the resist, and then a preheated acetone bath that can be placed in the sonic bath to strip off any extra resist.

Second Lithography step: Contacts

These steps will create contacts to the 2DEG.

NOTE: beginning in mid 2008 we switched to using aluminum as an implant mask rather than photoresist because of problems removing the resist after implantation. This involves modifications to steps 1–3 below.

1. Apply standard positive resist lithography and use Si(111) CONTACT mask.
2. Clean contact windows via RIE: `llscum.prc` for 45 seconds (optional)
3. Hardbake resist for 3 minutes at 120 C.
4. Send out wafers for phosphorous implantation (Core Systems):

- Dosage: 4.5×10^{14} cm^{-2}
- Energy: 50 keV with a 7°± tilt

Post-Implant & Anneal

After implantation, the wafers need the resist removed which will be harder to do due to implant. Try to remove the resist soon after the wafers return from implantation even if they will not be further processed for a while. Experience suggests that resist left in place for extended periods is significantly harder to remove.

- Use solvents first (two acetone baths)
- Only if absolutely necessary, use an RCA clean (which should take care of the rest), but for no more than ∼15 minutes.

Resist at the edges of the contact windows is typically the most stubborn.

- Typically the P implants are annealed in the LPS tube oven for 30–45 minutes at 950°C in N_2.
- The longer anneals tend to help reduce the height difference between the doped and undoped regions.
- For wafers greater than 3" in diameter, the Si(111) wafers need to be diced down to size and anneal each partial wafer one at a time. Once again make sure the partial wafers are clean of contamination and particulate before a high temp anneal.

Dicing & Testing

Now the wafer must be *diced* (cut into individual sample pieces) using the wafer dicing saw in room 1217. See C.4 for dicing instructions, including pre-dicing wafer protection and cleaning of individual samples after dicing.

B.2 Silicon on Insulator (SOI) Processing Steps

SOI Wafers come from *Soitec(Unibond).* Dimensions of the Box are 340nm Si and 400nm SiO_2, P–type doping, Handle resistivity >2000 Ohm–cm, Diameter:

- 4" wafers, Overall thickness: 525 μm.
- 6" wafers, Overall thichknes 675 μm

B.2.1 Oxide Growth

1. Send out SOI wafers for thermal oxidation (target thickness ∼30 nm of SiO_2). This step has been done at MEMs exchange, using an SC1, SC2 and HF preclean prior to a 30 minute oxidation at 950°C.
2. The SOI wafer is cleaned with IPA before being sent to be implanted with a double boron implant for the gate and shield layers.
3. Wafers are then sent out to Core systems (see C.5 for contact info) for double boron implant. The implant parameters are:
   - Gate: 300 keV at 4.0×10^{14} cm^{-2}
   - Shield: 25 keV at 2.0×10^{14} cm^{-2}
4. Substrate is heated to 350°C during the dual implant to increase the conductivity of the top layer and prevent pinholes in the SiO_2 caused by arcing.

Quarter Wafer Dicing (optional)

Since large wafers are difficult to work with we frequently pre–cut SOI into smaller pieces prior to lithography. 4" wafers are cut into quarters, while 6" wafers are cut into nine parts (5 rectangles and 4 arcs).

1. Clean Wafer with Acetone, Methanol, IPA. Blow Dry and set on 120°C hotplate for 2 minutes.
2. Apply Microposit™ resist @ 3000 rpm for 1 minute.

3. Softbake wafer at 90°C for 3–5 minutes.

4. Use dicing saw to cut the wafer into 1/4 pieces.

B.2.2 Precleaning

1. After the wafer returns from being implanted, it needs to be *thoroughly* cleaned before activating the implants. This includes a round in acetone, methanol and IPA. To help with the cleaning, try heating the acetone solution and methanol before placing the solution in the sonic bath.

2. Next, proceed with a Piranha clean (10–15 minutes), making sure to thoroughly rinse the wafer after any clean. Inspect under the microscope to make sure that all contamination and particulate has been removed before the high temperature anneal.

B.2.3 Activating Implants

The implanted ions must be thermally activated to ensure metallic behavior of the implanted silicon. There are two methods used for this activation:

1. Activate the implants by using the RTA on the "`rm_activate`" program. This will activate the double boron implant by heating the SOI to 950°C for 1 minute. It is recommended that this program be run twice, as on rare occasions a single run does not appear to be sufficient to ensure conduction.

2. Alternatively, activate implants in the tube oven at 900°C for 30 minutes in N_2 (assuming an oxide already exists on the top surface of the SOI). Remember only partial wafers can fit into the tube oven whereas whole 4" & 6" wafers can be activated in the RTA.

B.2.4 Photolithography (pre-ver8)

NOTE: this describes the process used prior to 2008. The 'version 8' design for the SOI sample introduced significant changes to the lithography process. See B.2.5 for the updated process.

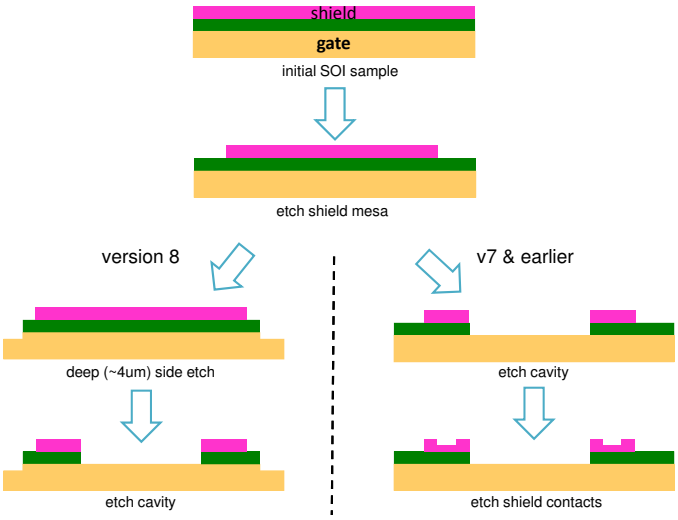

Figure B.2: Basic photolithography steps for the SOI sample.

The SOI substrate then goes through a series of three lithography steps using RIE. A mesa is defined around the edges of the substrate by etching away the top SiO_2 and Si layer of the SOI. Contacts to the shield layer are then exposed by etching some of p–Si. Lastly, we etch a 2 mm $\times$2 mm cavity to the gate layer (depth $\sim$760 nm) at the center of the SOI substrate.

Before doing contact lithography the mask should be inspected for cleanliness. Typically they need to be cleaned about every 10 uses. An effective method for cleaning off resist of the mask is to apply some acetone on the brown side of the chrome mask (side where wafer contacts the mask) and then rub a q–tip which is soaked in acetone as well and gently scrub the mask clean. While the mask is still wet with acetone, rinse with methanol, IPA and then blow dry the mask. Before spinning resist on the SOI make sure the spinner is clean and the vacuum chuck works properly. Typically wafers will not hold properly on the chuck due to resist on the backside of the wafer or an improper installation of the chuck (dirty o–ring), all of which disrupts the vacuum. Also ensure the spinner is set for 60 seconds and 3000 rpm.

First Layer: Mesa

This lithography step etches around the edges of the SOI to isolate the top surface of the substrate (the mesa) and provide registration markers for subsequent lithography steps. Use the standard Positive photoresist (906–10) lithography recipe (see C.1) along with the MESA mask. If you are patterning partial SOI wafers, make sure to leave some room (one alignment mark over) around the edges to allow tweezers to pick up the wafer in which not to scratch any critical die. Use the following recipes on the RIE (*See C.3 for specific details on these RIE recipes.*):

1. `llscum`: 30 seconds (removes residual resist in the developed areas)
2. `sio2pt`: 1min 15sec (removes top thermal oxide but times depend on thickness)
3. `engsix17`: 5min (removes silicon top layer)
4. `o2chambr`:7min (after sample is removed)

Remove the resist using acetone, methanol and IPA. Here, it is useful to have one acetone bath that strips off the majority of the resist, and then a preheated acetone bath that can be placed in the sonic bath to strip off any extra resist.

Second Layer: SHIELD CONTACT

Apply standard positive resist lithography and use the SHIELD mask. This will allow to make electrical contact to the shallow boron implant in the top layer of the Si within the SOI. The etch depth depends on the energy of the boron implant. RIE shield contact by using the following:

1. `llscum`: 30 sec
2. `sio2pt`: 1min 15sec
3. `engsix17`: 1min
4. `o2chambr`: 5min (after sample is removed)

Remove resist using solvents and similar procedures after the first lithography step. Make sure not to ultra–sonicate the SOI for long periods (we have found this to affect the BOX performance).

Third Layer: CAVITY

After this step is done and cleaned, repeat for the gate layer, this time doing:

1. `llscum`: 30 sec
2. `sio2pt`: 1min 15 sec
3. `engsix17`: 5min
4. `sio2pt`: 12min 45 sec
5. `o2chambr`: 20min (after sample is removed)

Remove resist using solvents using similar procedures from previous lithography steps.

Figure B.3 shows the walls created by this cavity etch.

Note: if necessary, a sterile, new, padded wiper can be used to rub the remaining photoresist off. At the moment, there is no evidence that this causes any scratching. Alternatively you can try a long DI rinse after the solvents. Place the sample under running DI (clean) for 1–2 minutes.

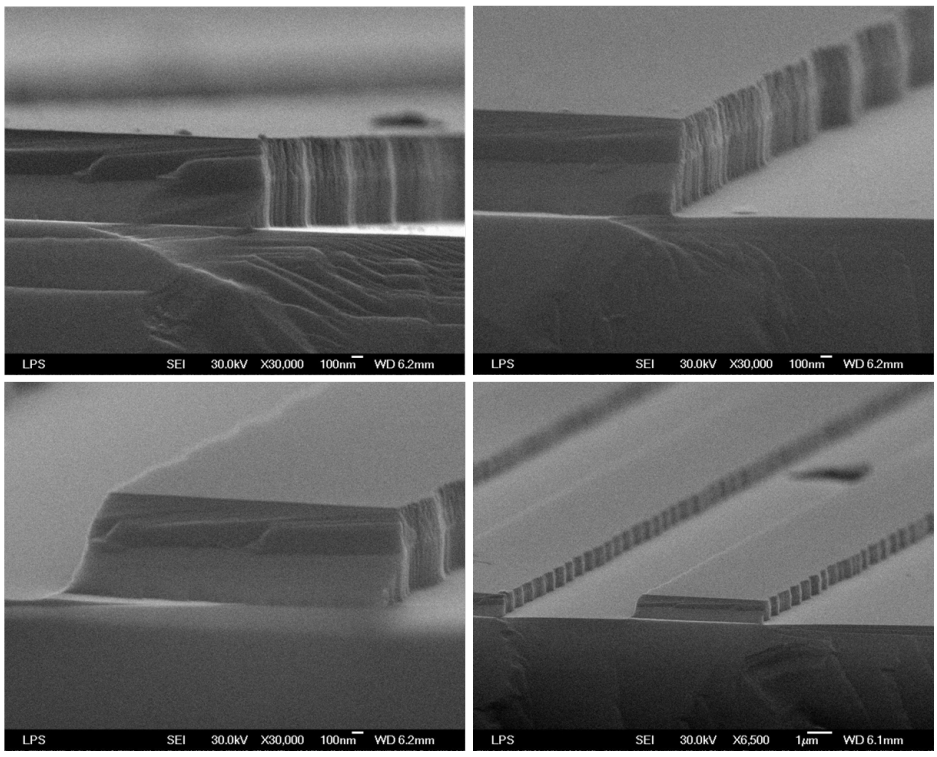

Figure B.3: SEM images of an SOI test sample. A grating pattern was etched using the standard cavity etch process to check for the possibility of undercutting of the cavity walls. Sample fabricated by Tomasz Kott; Images taken by Vitaley Zaretskey.

B.2.5 New "v8" SOI design

In late 2007/early 2008 we modified the SOI design to alleviate gate leakage problems. While the component steps were similar to those described above, a few key changes have been made:

1. The first etching step etches to the BOX as described in Section B.2.4. This is now called the SHIELD MESA.

2. Next we define a GATE MESA by etching through the BOX layer and deep ($\sim 4\mu$m into the handle layer, well past the depth of the gate ions. This helps isolate the gate from the sample edge.

3. Lastly we etch the CAVITY layer as before, though the shape has been changed from a simple 2 mm×2 mm square to the shape shown in Fig. B.4. The probed region at the cavity center is 0.4 mm × 0.4 mm. The four trumpet-shaped extensions are designed to tolerate alignment variances from the Ohmic contacts on the Si(111) substrate without changing the Van der Pauw geometry of the probed channel.

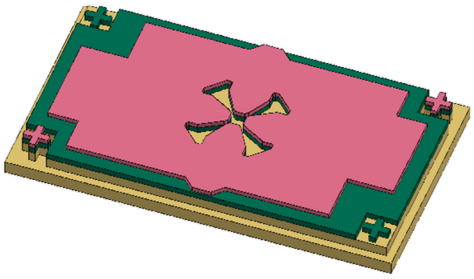

Figure B.4: SOI v8. The Shield mesa is recessed from the edge of the oxide layer to reduce the possibility of gate leakage round the outer edge of the device. The new cavity pattern ensures that we maintain a Van der Pauw geometry even if the Si(111) contacts are slightly misaligned.

B.2.6 Dicing & Testing

Now the wafer must be *diced* (cut into individual sample pieces) using the wafer dicing saw in room 1217. See C.4 for dicing instructions, including pre-dicing wafer protection and cleaning of individual samples after dicing.

Once the pieces have been cut and cleaned, test gate oxide of each sample on the probe station.

B.3 Contact Bonding the SOI and Si(111) samples

This proceedure applies to passivation and bonding performed in the cleanroom. Since early 2008 use of the N_2 glovebox has become standard proceedure, and the protocol has changed slightly.

At this point both SOI and Si(111) die are diced to size and both top surfaces need to be cleaned of any particulates and contamination from previous processing. The difficulty in this step is dependent on how clean the samples were kept while doing the previous lithography and annealing steps. Listed below is a typical cleaning procedure for cleaning and passivating the Si(111) surface with hydrogen but not all samples need to follow such cleaning procedures literally. Once both surfaces are clean and the Si(111) surface hydrogen–terminated, they are both introduced in a vacuum nearly the same time. Thus the cleaning steps are done in concert with one another and the user should be conscious of how long each step will take. Before cleaning it is best to start sparging a small Teflon beaker of NH_4F with N_2 ($\sim$1 hr).

B.3.1 Preparing the SOI for bonding

Cleaning SOI samples for bonding can vary greatly depending on how clean the samples are to begin with. Typically you take the best candidates from your inventory and do some standard cleans. Typically the procedure for cleaning is to

1. Ultrasonicate in IPA for a few minutes. Once again you should try to limit the time on this step.

2. Blow dry.

3. If the sample is still dirty try doing a DI rinse where the sample is under running DI for 1-2 minutes.

4. The next option is an RCA clean for 10–20 minutes.

5. Rinse in running DI
6. Piranha clean for 15 minutes
7. Rinse in running DI
8. RTA anneal: use `rm_anneal` (650°C for 2 min)
9. Place SOI sample in the sample holder and close the chamber.

B.3.2 Preparing the H-Si(111) sample for bonding

1. Ultra-sonicate in IPA for 10min
2. Rinse in running DI
3. RCA clean 10–20 min.
4. HF dip 20:1 for 2 min
   (removes sacrificial 30 nm SiO_2 layer grown in the beginning)
5. Rinse in DI for 2 sec
6. Blow dry
7. Place in sparged NH_4F for 5 min
8. Rinse in DI for 1 sec
9. Blow dry
10. Set on 120C hotplate for 30 sec
11. Load into the vacuum bond chamber (right after the SOI)

B.3.3 Vacuum Bond chamber

1. Load lock of the chamber has been purged with N_2 gas.
2. Once the samples are loaded, turn off the N_2 gas line and turn on the turbo pump

3. At 0.5 mTorr open the gate valve
4. Load the sample holder to the bonding chamber side
5. Let the bond chamber pump for 30–45 minutes.
6. Turn on the light bulb and initiate bond by moving the sapphire peg, pushing the samples against the sapphire boss.
7. Infrared camera will be able to detect bond.

Appendix C

Standard Fabrication Processes

adapted from material largely compiled by Kevin Eng and Tomasz Kott, July 2007

C.1 Photolithography

Positive resist process (906-10)

1. Rinse sample with IPA and blow dry
2. Water removal bake at 120°C for 2 minutes
3. Spin on HMDS at 3 krpm for 60 seconds (optional)
4. Spin on 906-10 at 3 krpm for 60 seconds
5. Prebake at 90°C for 1 minute
6. Expose in contact aligner 6 seconds.
7. Post exposure bake at 120°C for 1 minute
8. Develop for 1 minute in OPD 4262
9. Rinse in running DI for 1 minute

C.1.1 Positive resist process (908-35)

1. Rinse sample with IPA and blow dry
2. Water removal bake at 120°C for 3 minutes
3. Spin on HMDS at 2 krpm for 60 seconds
4. Spin on 908-35 at 3 krpm for 60 seconds
5. Prebake at 90°C for 1 minute
6. Expose in contact aligner 12 seconds (Exposed areas are visible in mask aligner after exposure, allowing easy multiple exposures).
7. Post exposure bake at 90°C for 1 minute
8. Develop for 1 minute in OPD 4262
9. Rinse in DI
10. Post development bake at 90°C for 3 minutes

C.1.2 Negative resist process (NR7 1500P)

This resist was used for the original process but has been replaced due to the difficulties in removing the resist.

1. Rinse sample with IPA and blow dry.
2. Water removal bake at 120°C for 2 minutes
3. Spin on HMDS at 3 krpm for 60 seconds
4. Spin on NR7 1500 P at 4.0 krpm for 60 seconds
5. Prebake at 90°C for 1 minute
6. Expose in contact aligner for 14 seconds
7. Post exposure bake at 120°C for 1 minute
8. Develop for 12 seconds in RD6
9. Rinse in DI
10. Post development bake at 120°C for 3 minutes

C.2 Cleaning Proceedures

C.2.1 Piranha cleaning

Piranha clean is highly oxidative and removes organic and metal contamination. If the sample has a large amount of organic impurities, the piranha etch will form an insoluable organic layer that can't be removed.

Piranha solution contains H_2SO_4 : H_2O_2 (4:1). Use the same quartz beaker for piranha cleans to minimize contamination.

1. Heat sulfuric acid at 120 to 130±C with a cover for at least 15 minutes.
2. Have a beaker ready for DI rinsing. Rinse out DI quartz beaker 2 times and place your tefon tweezers in the DI water.
3. Pour the hydrogen peroxide and stir the solution with your tweezers.
4. Place your sample in for 15 min.
5. Rinse the samples in DI water very well. Have the DI refreshed 3-4 times. The rinse should take about 5 min.
6. If the sample is going into a baker clean then no drying is necessary.
   Otherwise blow dry the sample.
7. To remove the piranha solution, let it cool for 10 min and pour down the acid/base waste sink and run the DI for several minutes.

C.2.2 RCA clean

NOTE: RCA clean (also called SC1) is very effective at removing many forms of stubborn contamination. However, we have found that it etches the portion of SiO_2 that has been exposed to ion implantation. Once this layer is gone, the solution slowly etches the doped Si underneath, causing irregular topography. Therefore, this clean should be used only when absolutely necessary and the cumulative total time spent in RCA should be carefully recorded. Keep the total exposure under 20 minutes.

The RCA solution that we use generally contains H_2O:NH_4OH:H_2O_2 (4:4:1). Use the same quartz beaker for RCA cleans to minimize cross-contamination.

1. Combine water and Ammonium Hydroxide and place on hot plate. Heat the solution to 80°C using the temperature probes.

2. Have a beaker ready for DI rinsing. Rinse out DI quartz beaker 2 times and place your Teflon tweezers in the DI water.

3. Pour the hydrogen peroxide and stir the solution with your tweezers. This cools down the solution. Wait a few minutes for the solution to start bubbling. Place the samples in, rinsing the tweezers after each contact with RCA.

4. Leave the sample in for about 15 minutes, depending on cleanliness.

5. Take the samples out of the RCA and into a refreshed DI water beaker. Then, rinse the samples in DI water very well. The rinse should take about 5 min.

6. To dispose of the RCA, let it cool for 10 min and pour down the acid/base waste sink while running DI.

C.2.3 Using the Temperature Probes on Hot plates

1. To use the temperature probes, make sure there is a solid connection to the back of the hot plates. On the hot-plate/stirrer combo one, a LED should be lit up indicating a probe is connected. On the other plates, the light will be lit up once a temperature is set.

2. Set the solution on the hotplate, and carefully lower the probes into solution.

3. Make sure that there is enough solution in the beaker so that in case of evaporation, the probe will still be in the solution. Also, make sure that the probes are not touching any of the glass.

4. After you are done using the probes, pour a large beaker of DI, and dip the probes in it to clean the probes from the solution. This is even more important if the probes are not constantly used for the same cleans.

C.3 RIE Etch Recipes and Rates

These are the standard recipes used in the Plasma Therm 790 Reactive Ion Etching machine at LPS.

recipe: `llscum`

task: surface clean before each run

run time: ∼45 seconds

gas: O_2 @ 16 sccm and 175 mTorr

RF: 50 W

recipe: `Sio2pt`

task: etching silicon dioxide

etch rate: ∼320 Å/ min

gas: CHF_3 @ 18 sccm and O_2 @ 2 sccm at 40 mTorr

RF: 175 W

recipe: `engsix17`

task: etching silicon on SOI

etch rate: ∼700 Å/ min

gas: SF6 @ 10 sccm and 20 mTorr

RF: 17 W

recipe: `engsix55`

task: etching silicon on Si(111)

etch rate: ∼1600 Å/ min

gas: SF6 @ 20 sccm and 10 mTorr

RF: 55 W

C.4 Dicing Saw

Prep for Wafer Dicing

Prior to dicing, wafers must be coated with resist to protect the surface from the grit and runoff produced by the saw.

1. Apply Microposit™ resist @ 1500rpm for 60 seconds.
2. Softbake wafer for 3 min @ 90C.
3. If desired, repeat previous steps to add a second coat for thicker coverage.
4. Mount back of the wafer on clear tape.

Dicing wafers

NOTE: these instructions are a guidline only. Use of the dicing saw generally requires training and authorization by the 'owner'. Contact Toby (or current cleanroom manager) for the current contact person and proceedures.

1. Grab our saw blades from storage (right now kept by Robert) both the flange and hub type of 3000 or 1800 grit.
2. Flange is used when the hub is already present on the saw, and is just the blade itself
3. Hub is used when that was the last type used, and houses both the saw blade and the holder
4. Use the torque wrench (until it clicks) to put on the small and larger holder (smooth side goes toward saw blade)

5. Use the setup and a test wafer to check the hairline, which is the location and width of the saw blade, so that the picture on the screen reflects the actual cut that will be made.

6. Use the dicing saw blade log to record:

   - the date
   - your initials
   - blade used
   - material cut
   - approximate # of cuts
   - blade wear and remaining exposure after cutting

Post-Dicing: Individual Samples:

Wafer sawing is the dirtiest step in the entire fabrication process. Therefore post-dicing cleaning is extremely important to successful bonding and high device yield.

1. Remove samples from clear tape and soak in acetone.
   (To prevent chipping, do not allow adjacent sample edges to rub together)

2. A double soak in acetone helps ensure that silicon particles or resist residue do not redeposit on to the die.

3. Complete cleaning with methanol and IPA.

4. Blow dry and place each die in the wafer tray.

C.5 Outsourcing companies

Core Systems: Ion Implantation

Attn: Chuck Hudak
1050 Kifer Rd.
Sunnyvale, CA 94086
Email:chudak AT coresystems.com
Telephone # (408) 328 1340
Fax: (408) 328 –1346

MEMs exchange: Oxide growth

For oxidation of Si(111) wafers:
Paul Sunal (Grower)
psunal AT mems-exchange.org
Christy Short (Business)
(703) 262-5375

NIST Gaithersburg: Oxide growth

For oxidation of Si(111) wafers:
Attn: Gerard Henein
gerard.henein AT nist.gov
301-975-8761
Russ Hajdaj (Technician)
russell.hajdaj AT nist.gov

Bibliography

[1] M. Shayegan, E. P. D. Poortere, O. Gunawan, Y. P. Shkolnikov, E. Tutuc, and K. Vakili, "Two-dimensional electrons occupying multiple valleys in AlAs," *physica status solidi (b)* **243** (2006) no. 14, 3629–3642. 1, 9, 18, 19, 73

[2] A. A. Shashkin, A. A. Kapustin, E. V. Deviatov, V. T. Dolgopolov, and Z. D. Kvon, "Strongly enhanced effective mass in dilute two-dimensional electron systems: System-independent origin," *Phys. Rev. B* **76** (Dec, 2007) 241302. 1, 42

[3] D. C. Tsui and G. Kaminsky, "Observation of sixfold valley degeneracy in electron inversion layers on si(111)," *Phys. Rev. Lett.* **42** (Feb, 1979) 595–597. 1, 2, 18, 70

[4] E. H. Hwang and S. Das Sarma, "Transport properties of two-dimensional electron systems on silicon (111) surfaces," *Phys. Rev. B* **75** (2007) no. 7, 073301. 1, 39, 40, 72

[5] A. Kapustin, A. Shashkin, V. Dolgopolov, M. Goiran, H. Rakoto, and Z. Kvon, "Spin susceptibility and polarization field in a dilute two-dimensional electron system in (111) silicon," *Physical Review B* **79** (2009) no. 20, . 2, 64

[6] G. S. Higashi, Y. J. Chabal, G. W. Trucks, and K. Raghavachari, "Ideal hydrogen termination of the si (111) surface," *Applied Physics Letters* **56** (Feb., 1990) 656–658. 3

[7] M. A. Hines, "IN SEARCH OF PERFECTION: understanding the highly Defect-Selective chemistry of anisotropic etching," *Annual Review of Physical Chemistry* **54** (2003) no. 1, 29–56. 3

[8] K. Reinhardt and W. Haber, *Handbook of Silicon Wafer Cleaning Technology, 2nd Edition, Second Edition.* William Andrew, 2 ed., 2008. 3, 15, 24, 27

[9] G. M. Gusev, Z. D. Kvon, N. N. Ovsyuk, and P. A. Cheremnych, "Hall resistance of a 2D electron gas at (111) silicon surface in strong magnetic field," *Sov.Phys.Sol.St.Phys* **28** (1986) no. 3, 510–511. 5

[10] L. Zheng and S. Das Sarma, "Coulomb scattering lifetime of a two-dimensional electron gas," *Phys. Rev. B* **53** (Apr, 1996) 9964–9967. 7, 62

[11] N. W. Ashcroft and N. D. Mermin, *Solid State Physics.* Brooks/Cole, Pacific Grove, CA, 1976. 9, 10

[12] T. Ando, A. B. Fowler, and F. Stern, "Electronic properties of two-dimensional systems," *Rev. Mod. Phys.* **54** (Apr, 1982) 437–672. 13, 15, 19, 20, 42, 44, 72, 84, 86

[13] M. Janen, O. Viehweger, U. Fastenrath, and J. Hajdu, *Introduction to the Theory of the Integer Quantum Hall Effect: Edited by J. Hajdu.* Wiley-VCH, 1 ed., Aug., 1994. 15

[14] B. Vinter and A. Overhauser, "Resolution of shubnikov-de haas paradoxes in si inversion layers," *Physical Review Letters* **44** (1980) no. 1, 47–50. 15, 70, 71

[15] M. Friesen, M. A. Eriksson, and S. N. Coppersmith, "Magnetic field dependence of valley splitting in realistic Si/SiGe quantum wells," *Applied Physics Letters* **89** (Nov., 2006) 202106–3. 16, 19

[16] J. L. McChesney, A. Kirakosian, R. Bennewitz, J. N. Crain, and F. J. Himpsel, "Gd disilicide nanowires attached to si(111) steps," *Nanotechnology* **13** (2002) no. 4, 545–547. 16

[17] N. Kharche, S. Kim, T. B. Boykin, and G. Klimeck, "Valley degeneracies in (111) silicon quantum wells," *Applied Physics Letters* **94** (Jan., 2009) 042101. 18

[18] F. Stern and W. E. Howard, "Properties of semiconductor surface inversion layers in the electric quantum limit," *Physical Review* **163** (Nov., 1967) 816. 19, 86

[19] S. S. Iyer, *Silicon Wafer Bonding Technology for VLSI and MEMS Applications*. The Institution of Engineering and Technology, illustrated edition ed., May, 2002. 22

[20] Q. Y. Tong and U. Gsele, *Semiconductor Wafer Bonding: Science and Technology*. John Wiley, New York, 1999. 22

[21] F. Grey and K. Hermansson, "Preservation of atomically clean silicon surfaces in air by contact bonding," *Applied Physics Letters* **71** (Dec., 1997) 3400–3402. 22

[22] K. Eng, R. McFarland, and B. Kane, "Integer quantum hall effect on hydrogen-passivated silicon (1 1 1) surfaces," *Physica E* **34** (Aug., 2006) 701–702. 28

[23] K. Eng, R. N. McFarland, and B. E. Kane, "High mobility two-dimensional electron system on hydrogen-passivated silicon(111) surfaces," *Appl. Phys. Lett.* **87** (2005) no. 5, 052106. 28

[24] K. Eng, R. N. McFarland, and B. E. Kane, "Integer Quantum Hall Effect on a Six-Valley Hydrogen-Passivated Silicon (111) Surface," *Phys. Rev. Lett.* **99** (July, 2007) 016801. 28, 53

[25] R. N. McFarland, T. M. Kott, L. Sun, K. Eng, and B. E. Kane, "Temperature-dependent transport in a sixfold degenerate two-dimensional electron system on a H-Si(111) surface," *Physical Review B (Condensed Matter and Materials Physics)* **80** (Oct., 2009) 161310–4. 29

[26] L. van der Pauw, "A method of measuring specific resistivity and hall effect of discs of arbitrary shape," *Philips Research Reports* **13** (1958) 1–9. 33

[27] S. V. Kravchenko and M. P. Sarachik, "Metalinsulator transition in two-dimensional electron systems," *Reports on Progress in Physics* **67** (2004) no. 1, 1–44. 38, 64

[28] S. S. Safonov, S. H. Roshko, A. K. Savchenko, A. G. Pogosov, and Z. D. Kvon, ""Metallic" and "Insulating" behavior of the Two-Dimensional electron gas on a vicinal surface of si MOSFET's," *Physical Review Letters* **86** (2001) no. 2, 272. 38

[29] B. Spivak, S. V. Kravchenko, S. A. Kivelson, and X. P. A. Gao, "Transport in strongly correlated two dimensional electron fluids," `0905.0414`. 38, 64

[30] D. A. Knyazev, O. E. Omel'yanovskii, V. M. Pudalov, and I. S. Burmistrov, "Metal-Insulator transition in two dimensions: Experimental test of the Two-Parameter scaling," *Physical Review Letters* **100** (Feb., 2008) 046405–4. 38

[31] S. D. Sarma and E. H. Hwang, "The so-called two dimensional metalinsulator transition," *Solid State Communications* **135** (2005) no. 9-10, 579–590. 38, 40

[32] A. Punnoose and A. M. Finkel'stein, "Dilute electron gas near the metal-insulator transition: Role of valleys in silicon inversion layers," *Phys. Rev. Lett.* **88** (Dec, 2001) 016802. 38

[33] S. V. Kravchenko, A. A. Shashkin, D. A. Bloore, and T. M. Klapwijk, "Shubnikov-de haas oscillations near the metal-insulator transition in a two-dimensional electron system in silicon," *Solid State Comm.* **116** (2000) no. 9, 495 – 499. 42

[34] F. F. Fang and P. J. Stiles, "Effects of a tilted magnetic field on a two-dimensional electron gas," *Phys. Rev.* **174** (Oct, 1968) 823–828. 44

[35] M. Padmanabhan, T. Gokmen, N. C. Bishop, and M. Shayegan, "Effective mass suppression in dilute, Spin-Polarized Two-Dimensional electron systems," *Phys. Rev. Lett.* **101** (July, 2008) 026402–4. 44, 45

[36] Y. P. Shkolnikov, S. Misra, N. C. Bishop, E. P. D. Poortere, and M. Shayegan, "Observation of quantum hall "Valley skyrmions"," *Physical Review Letters* **95** (2005) no. 6, 066809. 49

[37] U. Gummich and L. J. Sham, "Valley phase transition of a si inversion layer in high magnetic fields," *Physical Review B* **26** (Nov., 1982) 5611. 49

[38] A. Y. Kuntsevich, N. N. Klimov, S. A. Tarasenko, N. S. Averkiev, V. M. Pudalov, H. Kojima, and M. E. Gershenson, "Intervalley scattering and weak localization in si-based two-dimensional structures," *Phys. Rev. B* **75** (May, 2007) 195330–9. 54, 56, 58

[39] R. R. Gerhardts, D. Weiss, and K. v. Klitzing, "Novel magnetoresistance oscillations in a periodically modulated two-dimensional electron gas," *Physical Review Letters* **62** (Mar., 1989) 1173. 54

[40] W. Zhang, M. A. Zudov, L. N. Pfeiffer, and K. W. West, "Resonant phonon scattering in quantum hall systems driven by dc electric fields," *Physical Review Letters* **100** (2008) no. 3, 36805–36805. 54

[41] E. H. Hwang and S. D. Sarma, "Hall coefficient and magnetoresistance of two-dimensional spin-polarized electron systems," *Physical Review B* **73** (Mar., 2006) 121309. 58

[42] C. A. Kukkonen and P. F. Maldague, "Electron-electron scattering: Hall coefficient and magnetoresistance," *Phys. Rev. B* **19** (Feb, 1979) 2394–2397. 58

[43] S. A. Vitkalov, "Hall coefficient and electron-electron interaction of two-dimensional electrons in si mosfets," *Phys. Rev. B* **64** (Oct, 2001) 195336. 58

[44] A. Alkauskas, K. Flensberg, B. Y.-K. Hu, and A.-P. Jauho, "Sign reversal of drag in bilayer systems with in-plane periodic potential modulation," **66** (Nov, 2002) 201304. 61

[45] M. P. Lilly, J. P. Eisenstein, L. N. Pfeiffer, and K. W. West, "Coulomb drag in the extreme quantum limit," *Phys. Rev. Lett.* **80** (Feb, 1998) 1714–1717. 61

[46] A. S. Price, A. K. Savchenko, B. N. Narozhny, G. Allison, and D. A. Ritchie, "Giant fluctuations of coulomb drag in a bilayer system," *Science* **316** (Apr, 2007) 99–102. 61

[47] N. P. Ong, "Geometric interpretation of the weak-field hall conductivity in two-dimensional metals with arbitrary fermi surface," *Physical Review B* **43** (1991) no. 1, 193. 61

[48] G. F. Giuliani and J. J. Quinn, "Lifetime of a quasiparticle in a two-dimensional electron gas," *Physical Review B* **26** (Oct., 1982) 4421. 62

[49] C. E. Yasin, T. L. Sobey, A. P. Micolich, W. R. Clarke, A. R. Hamilton, M. Y. Simmons, L. N. Pfeiffer, K. W. West, E. H. Linfield, M. Pepper, and D. A. Ritchie, "Interaction correction to the longitudinal conductivity and hall resistivity in high-quality two-dimensional gaas electron and hole systems," *Phys. Rev. B* **72** (Dec, 2005) 241310. 62

[50] S. Das Sarma and E. H. Hwang, "Temperature dependent weak field hall resistance in two-dimensional carrier systems," *Phys. Rev. Lett.* **95** (Jun, 2005) 016401. 62

[51] A. Kuntsevich, D. Knyazev, V. Kozub, V. Pudalov, G. Brunthaler, and G. Bauer, "Nonmonotonic temperature dependence of the hall resistance of a 2D electron system in silicon," *JETP Letters* **81** (Apr., 2005) 409–412, `cond-mat/0504475`. 62

[52] K. Lai, W. Pan, D. Tsui, S. Lyon, M. Mhlberger, and F. Schffler, "Two-Flux composite fermion series of the fractional quantum hall states in strained si," *Physical Review Letters* **93** (2004) no. 15, . 64

[53] E. P. D. Poortere, E. Tutuc, Y. P. Shkolnikov, K. Vakili, and M. Shayegan, "Magnetic-field-induced spin polarization of AlAs two-dimensional electrons," *Physical Review B* **66** (Oct., 2002) 161308. 64

[54] A. A. Shashkin, "Metal-insulator transitions and the effects of electron-electron interactions in two-dimensional electron systems," *Physics-Uspekhi* **48** (2005) no. 2, 129–149. 64

[55] S. D. Sarma and E. H. Hwang, "Low-density spin-polarized transport in two-dimensional semiconductor structures: Temperature-dependent magnetoresistance of si MOSFETs in an in-plane applied magnetic field," *Physical Review B* **72** (Nov., 2005) 205303. 64

[56] E. P. D. Poortere, E. Tutuc, and M. Shayegan, "Critical resistance in the AlAs quantum hall ferromagnet," *Physical Review Letters* **91** (Nov., 2003) 216802. 67

[57] K. Lai, W. Pan, D. C. Tsui, S. Lyon, M. Mhlberger, and F. Schffler, "Intervalley gap anomaly of Two-Dimensional electrons in silicon," *Physical Review Letters* **96** (Feb., 2006) 076805. 67

[58] W. J. Skocpol, P. M. Mankiewich, R. E. Howard, L. D. Jackel, D. M. Tennant, and A. D. Stone, "Universal conductance fluctuations in silicon inversion-layer nanostructures," *Physical Review Letters* **56** (June, 1986) 2865. 69

[59] S. A. Scott, W. Peng, A. M. Kiefer, H. Jiang, I. Knezevic, D. E. Savage, M. A. Eriksson, and M. G. Lagally, "Influence of surface chemical modification on charge transport properties in ultrathin silicon membranes," *ACS Nano* **3** (July, 2009) 1683–1692. 73

[60] G. Dubey, G. P. Lopinski, and F. Rosei, "Influence of physisorbed water on the conductivity of hydrogen terminated silicon-on-insulator surfaces," *Applied Physics Letters* **91** (2007) no. 23, 232111. 73

[61] M. Nishizawa, L. Bolotov, T. Tada, and T. Kanayama, "Scanning tunneling microscopy detection of individual dopant atoms on wet-prepared si(111):h surfaces," *J. Vac. Sci. Technol. B* **24** (2006) no. 1, 365–369. 73

[62] S. R. Schofield, N. J. Curson, M. Y. Simmons, F. J. Rue, T. Hallam, L. Oberbeck, and R. G. Clark, "Atomically precise placement of single dopants in si," *Physical Review Letters* **91** (2003) no. 13, 136104–136104. 74

Index